

**SYNTHESIS AND STUDY OF STRUCTURAL AND MAGNETIC  
PROPERTIES OF FERRITE NANOCRYSTALS FOR  
MAGNETOCALORIC APPLICATIONS**

By

**Silvana Rocio Urcia Romero**

Thesis submitted for the partial requirements for the degree of

MASTER OF SCIENCE

in

Physics

UNIVERSITY OF PUERTO RICO  
MAYAGÜEZ CAMPUS  
2011

Approved by:

_____ Oscar Perales-Pérez, Ph.D. President, Graduate Committee	_____ Date
_____ Félix Fernández, Ph.D. Member, Graduate Committee	_____ Date
_____ Héctor Jiménez, Ph.D. Member, Graduate Committee	_____ Date
_____ Luis F. Gordillo-Guerrero Representative Graduate Studies, Ph.D.	_____ Date
_____ Dorial Castellanos, Ph.D. Director of Department of Physics	_____ Date

## ABSTRACT

Pure and doped  $\text{Co}_x\text{Zn}_{1-x}\text{Fe}_2\text{O}_4$  ( $0.5 \leq x \leq 1.0$ ) nanocrystals have been synthesized by conventional and modified size-controlled coprecipitation methods. In the latter, the control of the oversaturation in reacting solutions, attained by controlling the flow rate at which the reactants were contacted, promoted heterogeneous nucleation and hence crystal growth. The size-controlled synthesis route allowed the tuning of the maximum magnetization and the coercivity, which increased by a factor of nine. The demagnetization temperature ( $T_d$ ) was also found to be strongly dependent on both, the Co atomic fraction and crystal size and varied between 106 °C and 540 °C. Mössbauer spectroscopy confirmed the strong influence of the synthesis conditions on the superparamagnetic fraction in the samples.

In order to investigate the effect of rare-earth ions on the properties of the ferrite, RE-doped  $\text{Co}_{0.7}\text{Zn}_{0.3}\text{Fe}_2\text{O}_4$ , nanoparticles (RE=Gd and Dy ions), were also synthesized by following the above mentioned synthesis approaches. The average crystallite size varied from  $(9.43 \pm 0.13)\text{nm}$ , in the conventional synthesis method, to  $(18.45 \pm 0.11)\text{nm}$  when the ferrite was synthesized at 1 mL/min. The maximum magnetization of the ferrite synthesized by the conventional approach decreased from 60 emu/g (non-doped ferrite) to 55 emu/g when it was doped with 1 at % of Dy; this maximum magnetization went up to 62 emu/g when the synthesis was carried out under flow-controlled conditions. The demagnetization temperature went down from 350 °C (non-doped ferrite) to 320 °C for the same content of Dy ions and was further decreased down to 308 °C when the ferrite powders were synthesized under flow-rate controlled conditions. Regarding the effect of Gd dopant, estimated  $T_d$ -values decreased from 350 to 230 °C for Gd-doping levels between 0.00 and 0.05, respectively. The weakening of the Fe-RE super-exchange interaction

when  $\text{Fe}^{3+}$  is substituted by  $\text{Gd}^{3+}$  (due to screening of the  $4f$  electrons by the outer electrons), and the paramagnetic character of the  $\text{Gd}^{3+}$  ions could explain this trend in  $T_d$ .

The results of the experimental design evidenced the strong dependence of the average crystallite size and the coercivity on both, the  $\text{Gd}^{3+}$  and NaOH concentrations. The variation of the solubility of the hydroxide ferrite precursor would have promoted the spin canting effect and formation of dead magnetic layer on the nanoparticle surface.

On a materials application basis, the following remarks summarize our main findings. The highest magnetization was 73 emu/g ( $x = 0.7$ ) and was attained when the ferrite powders were synthesized by the hydrothermal method. However, neither the coercivity nor the demagnetization temperatures were suitable for applications in the magnetocaloric pump. Although we could decrease  $T_d$  by increasing the Zn concentrations ( $T_d$  can be as low as 100 °C), it would take place at expenses of the drop in magnetization and the pyromagnetic coefficient. This applicability scenario becomes more promising after doping the ferrite with Gd or Dy species. For 5% doping the maximum magnetization was an acceptable 53 emu/g, while the coercivity reached a low value of 20 Oe, which are in the required range for applications. The lowest value for the demagnetization temperature was 230 °C reached with Gd-doping. This same sample had a pyromagnetic coefficient of 0.59 emu/g-K, which is a significant increase over all other systems evaluated in this work and also the literature.

Therefore, from a material application viewpoint in magnetocaloric pumping, the doping of the CoZn ferrite with Gd species will promote both, the drop in the demagnetization temperature (it decreased from 350 °C down to 230 °C) and a remarkable increase of the pyromagnetic

coefficient. The moderate magnetization and minimum coercivity of these nanoparticles enable them to be considered a very promising candidate for magnetocaloric pumping systems.

## RESUMEN

Nanocristales de  $\text{Co}_x\text{Zn}_{1-x}\text{Fe}_2\text{O}_4$  ( $0.5 \leq x \leq 1.0$ ) puros y dopados fueron sintetizados mediante el método de coprecipitación y el método de tamaño controlado. En el último, el control de la sobresaturación en la solución reactante fue logrado mediante el control de la razón de flujo al cual los reactantes fueron contactados, promoviendo la nucleación heterogénea y el crecimiento del cristal. La síntesis de tamaño controlado también permite el control de la magnetización máxima y la coercividad, la cual incrementa en un factor de nueve. La temperatura de magnetización es fuertemente dependiente de la fracción atómica de Co y del tamaño del cristal, variando desde  $106^\circ\text{C}$  a  $540^\circ\text{C}$ . La espectroscopía Mössbauer confirma la fuerte influencia de las condiciones de síntesis sobre la fracción superparamagnética en las muestras. Con la finalidad de investigar el efecto de los iones de tierras raras sobre las propiedades de las nanopartículas de ferrita de  $\text{Co}_{0.7}\text{Zn}_{0.3}\text{Fe}_2\text{O}_4$  fueron dopadas con iones de tierras raras (Gd y Dy). Estas muestras también sintetizadas mediante los métodos mencionados anteriormente. En general, el tamaño promedio del cristalito varía desde  $(9.43 \pm 0.13)\text{nm}$ , en el método de síntesis convencional, a  $(18.45 \pm 0.11)\text{nm}$  cuando las ferritas fueron sintetizadas a  $1\text{mL}/\text{min}$ . La máxima magnetización de la ferrita decrece desde  $60\text{emu}/\text{g}$  (sin dopaje) a  $55\text{emu}/\text{g}$  cuando fue dopada a  $1\text{at.}\%$  de Dy. La magnetización máxima de la ferrita de Co-Zn dopada con Dy ( $y = 0.01$ ) se incrementó a  $62\text{emu}/\text{g}$  cuando la síntesis fue llevada a cabo bajo condiciones de flujo controlado. La temperatura de desmagnetización disminuye desde  $350^\circ\text{C}$  (sin dopaje) a  $320^\circ\text{C}$  para el mismo contenido de iones de Dy y disminuyó aún más hasta  $308^\circ\text{C}$  a niveles diferentes. En el sistema dopado con Gd, los valores estimados para  $T_d$  disminuyeron desde  $350^\circ\text{C}$  a  $230^\circ\text{C}$  para niveles de dopaje de Gd entre  $0.00$  y  $0.05$ , respectivamente. El debilitamiento de la interacción de superintercambio Fe-Re cuando los iones de  $\text{Fe}^{3+}$  son sustituidos por iones de  $\text{Gd}^{3+}$  (debido al apantallamiento de

los electrones 4f por los electrones ubicados en los niveles más externos) explica esta disminución en  $T_d$ .

Los resultados del diseño experimental evidenciaron la fuerte dependencia del tamaño promedio del cristalito y la coercividad, tanto con la concentración de  $Gd^{3+}$  como con la concentración de NaOH. La variación de la solubilidad del hidróxido precursor de la ferrita puede haber favorecido el canting de los espines en la superficie del cristal y la formación de capas magnéticamente muertas.

Desde un punto visto de aplicación de nuestros materiales, las siguientes observaciones resumen nuestros principales resultados. La magnetización más alta fué de 73emu/g ( $x=0.7$ ) y se obtuvo cuando los polvos fueron sintetizados mediante el método hidrotermal. Sin embargo ni la coercividad ni la temperatura de desmagnetización, fueron las deseadas para potenciales aplicaciones en la bomba magneto calórica. A pesar que se pudo disminuir  $T_d$  mediante el incremento de las concentraciones de Zn ( $T_d$  alcanzó los 100 °C), esto ocurrió a expensas de una reducción de la magnetización y del coeficiente piromagnético. El escenario para la aplicación de nuestros materiales se hizo más prometedor luego de dopar a la ferrita con especies de Gd o Dy. Para dopajes del 5 at.% la máxima magnetización fué un aceptable 53 emu/g, mientras la coercividad alcanzó un valor tan bajo como 20 Oe, los cuales están en el rango requerido para la aplicación. El valor más bajo para la temperatura de desmagnetización fue de 230 °C, lo cual fué logrado dopando con Gd. Esta misma muestra tiene un coeficiente piromagnético de 0.59 emu/g-K, lo cual representa un incremento importante comparado con todos los otros sistemas reportados en la literatura así como los evaluados en este trabajo.

Por lo tanto, desde el punto de vista de la aplicación del material en la bomba magnetocalórica, el dopaje de las ferritas de CoZn con especies de Gd promoverá la disminución en la temperatura

de desmagnetización (esta decrece desde 350 °C hasta 230 °C) y un notable incremento del coeficiente piromagnético. Además, el valor moderado de magnetización y mínima coercividad permiten considerar a las ferritas de CoZn dopadas con Gd como un candidato muy prometedor para los sistemas de la bomba magnetocalórica.

**Copyright © 2011**  
**By**  
**Silvana Rocio Urcia Romero**

## DEDICATORY

*To God, for his infinite love and protection*

*To my parents Gerardina and Emilio, and my  
brothers Poll and Bryam for their unconditional  
support, inspiration, and love.*

## ACKNOWLEDGEMENTS

Very special thanks to the University of Puerto Rico at Mayagüez for giving me the opportunity to develop as a researcher.

During the completion of my graduate studies at the University of Puerto Rico many persons and institutions collaborated directly and indirectly with my research. Without their support it would have been impossible for me to finish my work. Hence, I wish to dedicate this section to recognizing their support. This work would not have been possible without the support of:

- Dr. Oscar Perales Pérez for his support, guidance, transmitted knowledge, motivation and scientific discussions, and the opportunity to work in his laboratory.
- Dr. Oswald Uwakweh for his scientific advice, interest in my research, and Mössbauer spectroscopy analysis.
- Dr. Henri Radovan for his unconditional support, guidance, discussions and contributions to my research.
- M.S. Segundo Jauregui Rosas for his support in searching for information and suggestions at the beginning of my research and his valuable friendship.
- Dr. Mauricio Cabrera Rios for his support and guidance in the statistical work, analysis and suggestion in my research.
- Dr. Héctor Jiménez and Dr. Félix Fernández for accepting the committee participation, their teachings, and transmitted knowledge for the completion of my work.
- Dr. Yong-Jihn Kim for his wisdom on the theory of magnetism.
- Dr. Jeannette Santos for allowing me to work in outreach activities within CREST.
- Dr. Samuel Hernández and M.S. Leonardo Pacheco for their time dedicated to carry out Raman measurements.
- M.S. Celia Osorio Cantillo for her support and guidance in the beginning of my research and her friendship.
- Ms. Yarilyn Cedeño Matei for her help in TEM measurements and her friendship.
- Ing. Turner Vidal Urquiza for his support with the Autocad design program and his friendship.
- M.S. Yareni P. Lara Rodríguez for help with the statistical method and Minitab program, Zaimara Hernández for contribution in the material synthesis for the statistical model.
- My colleagues and friends for their help in this work and for making my stay enjoyable in Puerto Rico.

The material for this research is based on work supported by the U.S. Department of Defense under Award No. 50797-RT-ISP.

# TABLE OF CONTENTS

<i>LIST OF TABLES</i> .....	<i>XV</i>
<i>LIST OF FIGURES</i> .....	<i>XVIII</i>
<b>CHAPTER I: INTRODUCTION</b> .....	<b>1</b>
<b>1.1 Motivation</b> .....	<b>1</b>
<b>1.2 Aim of study</b> .....	<b>5</b>
<b>Main Objective</b> .....	<b>5</b>
<b>Specific Objectives</b> .....	<b>5</b>
<b>CHAPTER II: THEORETICAL BACKGROUND</b> .....	<b>6</b>
<b>2.1 Magnetism and Magnetic Materials</b> .....	<b>6</b>
<b>Diamagnetism and Paramagnetism</b> .....	<b>10</b>
<b>Ferromagnetism</b> .....	<b>11</b>
<b>Antiferromagnetism and Ferrimagnetism</b> .....	<b>12</b>
<b>Magnetic Anisotropy</b> .....	<b>15</b>
<b>Magnetic Domains</b> .....	<b>18</b>
<b>Single domains</b> .....	<b>19</b>
<b>Magnetization Curve and Hysteresis Loop</b> .....	<b>20</b>
<b>Magnetic Properties and Crystal Size</b> .....	<b>22</b>
<b>Superparamagnetism</b> .....	<b>22</b>
<b>Magnetism of Rare Earth Metal Ions</b> .....	<b>24</b>
<b>Ferrites</b> .....	<b>25</b>
<b>2.2 Nanoparticles synthesis by co-precipitation</b> .....	<b>31</b>
<b>Thermodynamics of co-precipitacion</b> .....	<b>33</b>
<b>2.3 Ferrofluids and the Magnetocaloric Pump</b> .....	<b>41</b>
<b>2.4 Fundamentals of Experimental Design</b> .....	<b>42</b>
<b>CHAPTER III: PREVIOUS RELATED WORKS</b> .....	<b>45</b>
<b>CHAPTER IV: EXPERIMENTAL DETAILS</b> .....	<b>52</b>

<b>4.1</b>	<b>Synthesis of CoZn Ferrite Nanoparticles .....</b>	<b>52</b>
4.1.1.	Materials .....	52
4.1.2.	Conventional Co-Precipitation Method .....	52
4.1.3.	Size-Controlled Co-Precipitation Method .....	53
<b>4.2</b>	<b>Synthesis of <math>\text{Co}_{0.7}\text{Zn}_{0.3}\text{Fe}_2\text{O}_4</math> Nanoparticles by Hydrothermal Method .....</b>	<b>54</b>
4.2.1.	Materials and Procedure .....	55
<b>4.3</b>	<b>Synthesis of RE doped <math>\text{Co}_{0.7}\text{Zn}_{0.3}\text{Fe}_2\text{O}_4</math> Nanoparticles (RE=Dy or Gd) .....</b>	<b>56</b>
4.3.1.	Materials .....	56
4.3.2.	Conventional Co-Precipitation Method .....	56
4.3.3.	Size-Controlled Precipitation Method .....	56
<b>4.4</b>	<b>Synthesis of Gd doped <math>\text{Co}_{0.7}\text{Zn}_{0.3}\text{Fe}_2\text{O}_4</math> Nanoparticles Using a Statistical Model ..</b>	<b>57</b>
4.4.1.	Materials and Procedure .....	57
<b>4.5</b>	<b>Characterization of Ferrite Nanocrystals .....</b>	<b>57</b>
4.5.1.	X-Ray Diffractometry (XRD) .....	58
4.5.2.	Raman Spectroscopy (RS).....	60
4.5.3.	High Resolution Transmission Electron Microscopy (HRTEM) .....	61
4.5.4.	Vibrating Sample Magnetometry (VSM) .....	63
4.5.5.	Mössbauer Spectroscopy (MS) .....	64
<b>CHAPTER V: RESULTS AND DISCUSSION .....</b>		<b>68</b>
<b>5.1</b>	<b>Tuning of Magnetic Properties in <math>\text{Co}_x\text{Zn}_{1-x}\text{Fe}_2\text{O}_4</math> Ferrite Nanocrystals Synthesized by a Size Controlled and Conventional Co-Precipitation Method .....</b>	<b>68</b>
5.1.1.	Conventional (i.e., no control on flow-rate) ferrite synthesis.....	68
5.1.1.1.	Structural Analyses.....	68
5.1.1.2.	Magnetic Measurements .....	72
5.1.1.3.	Mössbauer Spectroscopy Analyses.....	76
5.1.2.	Size-controlled synthesis.....	79
5.1.2.1.	Structural Analyses.....	79
5.1.2.2.	Magnetic Measurements .....	83
5.1.2.3.	Mössbauer Spectroscopy Analyses.....	86

5.1.2.4. Concluding Remarks .....	90
<b>5.2 Effect of Temperature on the <math>\text{Co}_x\text{Zn}_{1-x}\text{Fe}_2\text{O}_4</math> (<math>x=0.7</math>) Nanoparticles Synthesized by Hydrothermal Method.....</b>	<b>91</b>
5.2.1. Structural Analyses.....	91
5.2.2. Magnetic Measurements .....	94
5.2.3. Concluding Remarks .....	97
<b>5.3 Effect of Dy Doping on the Structural and Magnetic Properties of <math>\text{Co}_x\text{Zn}_{1-x}\text{Fe}_2\text{O}_4</math> (<math>x=0.7</math>) Ferrite Nanocrystals.....</b>	<b>98</b>
5.3.1. Conventional (i.e, no control on flow-rate) ferrite synthesis.....	98
5.3.1.1. Structural Analyses.....	98
5.3.1.2. Magnetic Measurements .....	101
5.3.2. Size-controlled synthesis.....	105
5.3.2.1. Structural Analyses.....	105
5.3.2.2. Magnetic Measurements .....	108
5.3.3. Concluding Remarks .....	110
<b>5.4 Effect of Gd Doping on the Structural and Magnetic Properties of Co-Zn (<math>x=0.7</math>) Ferrite Nanocrystals.....</b>	<b>110</b>
5.4.1. Conventional (i.e, no control on flow-rate) ferrite synthesis.....	110
5.4.1.1. Structural Analyses.....	110
5.4.1.2. Magnetic Measurements .....	112
5.4.2. Size-controlled synthesis.....	114
5.4.2.1. Structural Analyses.....	114
5.4.2.2. Magnetic Measurement .....	117
5.4.3. Concluding Remarks .....	120
<b>5.5 Attempts to Optimize the Magnetic Properties in <math>\text{Gd}^{3+}</math> Doped <math>\text{Co}_x\text{Zn}_{1-x}\text{Fe}_2\text{O}_4</math> (<math>x=0.7</math>) Ferrite Nanocrystals Synthesized by the Conventional Co-precipitation Method</b>	<b>120</b>
5.5.1. Effect of the selected synthesis parameters on the average crystallite size of $\text{Co}_{0.7}\text{Zn}_{0.3}\text{Fe}_{2-z}\text{Gd}_z\text{O}_4$ .....	122
Statistical Characterization .....	124
Analysis $2^2$ factorial design .....	124

Analysis for the central composite design .....	126
5.5.2. Effect of the Selected Synthesis Parameters on the Magnetic Properties of $\text{Co}_{0.7}\text{Zn}_{0.3}\text{Fe}_{2-z}\text{Gd}_z\text{O}_4$ .....	127
Statistical Characterization .....	129
Analysis of $2^2$ factorial design.....	129
Analysis for the central composite design .....	130
5.5.3. Concluding Remarks .....	132
<i>CHAPTER VI: FINAL REMARKS</i> .....	133
<i>CHAPTER VII: REFERENCES</i> .....	138

## LIST OF TABLES

<b>Table 1.</b> Ionic radii for selected metal ions usually present in ferrites <sup>31</sup> .....	27
<b>Table 2.</b> Spin configuration of some 3d-metal ions and magnetic moment contribution.....	28
<b>Table 3.</b> Average crystallite size, <i>D</i> , and lattice parameter, <i>a</i> , for $\text{Co}_x\text{Zn}_{1-x}\text{Fe}_2\text{O}_4$ synthesized at different Co atomic fractions, 'x', by the conventional co-precipitation method.....	70
<b>Table 4.</b> Summary of the Raman shifts for tetrahedral and octahedral sites in Co-Zn ferrite. ....	71
<b>Table 5.</b> Magnetization ( <i>M</i> ) and coercivity ( <i>H</i> ) for the CoZn ferrite at different <i>x</i> - values, synthesized by the conventional co-precipitation method. ....	73
<b>Table 6.</b> Demagnetization temperature ( <i>T<sub>d</sub></i> ) for the CoZn ( <i>x</i> =0.5, 0.7, 0.8, 0.9 and 1.0) ferrite synthesized by the conventional co-precipitation method. ....	75
<b>Table 7.</b> Mössbauer parameters for the CoZn ( <i>x</i> =0.5, 0.8, and 0.9) ferrite nanocrystals synthesized by the conventional co-precipitation method. ....	77
<b>Table 8.</b> Average crystallite size, <i>D</i> , lattice parameter, <i>a</i> , for $\text{Co}_x\text{Zn}_{1-x}\text{Fe}_2\text{O}_4$ synthesized at different Co atomic fractions, ('x'=0.5, 0.8, 0.9, 1.0) by size-controlled synthesis method. ....	81
<b>Table 9.</b> Maximum magnetization ( <i>M</i> ) and coercivity ( <i>H</i> ) for the CoZn ( <i>x</i> =0.5,0.8,0.9 and 1.0) ferrite synthesized by co-precipitation method with different flow rates. ....	85
<b>Table 10.</b> Mössbauer parameters for the CoZn ( <i>x</i> =0.9) ferrite nanocrystals synthesized by conventional co-precipitation ( <i>N-F</i> ) and size-controlled method at 20mL/min and 1mL/min. ....	88
<b>Table 11.</b> Average crystal size, <i>D</i> , and lattice parameter, <i>a</i> , for the $\text{Co}_{0.7}\text{Zn}_{0.3}\text{Fe}_2\text{O}_4$ ferrite at different temperatures of the synthesis. The powders were synthesized by co-precipitation ( <i>T</i> =100oC) and hydrothermal method (100 oC-250 oC). ....	92

**Table 12.** Summary of magnetic properties for the  $\text{Co}_{0.7}\text{Zn}_{0.3}\text{Fe}_2\text{O}_4$  ferrite at different temperatures of the synthesis. The powders were synthesized by co-precipitation ( $T=100^\circ\text{C}$ ) and hydrothermal methods. .... 95

**Table 13.** Demagnetization temperature for the  $\text{Co}_{0.7}\text{Zn}_{0.3}\text{Fe}_2\text{O}_4$  ferrite at different temperatures of the synthesis. The powders were synthesized by co-precipitation and hydrothermal methods. .... 96

**Table 14.** Average crystallite size,  $D$ , lattice parameter,  $a$ , for Gd doped Co-Zn ferrite synthesized at different Dy atomic fractions, 'y' by conventional co-precipitation method. 99

**Table 15.** Magnetization ( $M$ ) and coercivity ( $H$ ) of Dy-doped CoZn ferrite synthesized at different Dy atomic fractions, 'y', synthesized by the co-precipitation method without flow rate control. .... 102

**Table 16.** Demagnetization temperature ( $T_d$ ) for Dy-doped CoZn ferrite at different Dy atomic fractions, 'y'. Samples were synthesized by the conventional co-precipitation method..... 104

**Table 17.** Average crystallite size,  $D$ , size and lattice parameter,  $a$ , for the Dy (0.01) doped  $\text{CoZn}(x=0.7)$  ferrite synthesized by the conventional co-precipitation method. .... 106

**Table 18.** Average crystallite size,  $D$ , size and lattice parameter,  $a$ , for the  $\text{Co}_{0.7}\text{Zn}_{0.3}\text{Fe}_{2-z}\text{Gd}_z\text{O}_4$  ferrite synthesized at various Gd atomic fractions, 'z'. The samples were synthesized by the conventional co-precipitation method. .... 111

**Table 19.** Magnetization ( $M$ ) and coercivity ( $H$ ) of  $\text{Co}_{0.7}\text{Zn}_{0.3}\text{Fe}_{2-z}\text{Gd}_z\text{O}_4$  ( $z=0.01, 0.03, 0.05$ ), synthesized by the conventional co-precipitation method. .... 112

**Table 20.** Average crystallite size,  $D$ , size and lattice parameter,  $a$ , for the  $\text{Co}_{0.7}\text{Zn}_{0.3}\text{Fe}_{2-z}\text{Gd}_z\text{O}_4$  ( $z=0.01, 0.03, 0.05$ ) ferrite synthesized by the size-controlled method. .... 116

**Table 21.** Maximum magnetization and coercivity for the Gd-doped  $\text{Co}_{0.7}\text{Zn}_{0.3}\text{Fe}_{2-z}\text{Gd}_z\text{O}_4$  ( $z=0.01, 0.03, 0.05$ ) ferrite synthesized by the size-controlled method. .... 118

**Table 22.** Average crystallite size,  $D$ , for the coded and experimental levels in  $2^2$  factorial and CCD experimental design applied to the synthesis of  $\text{Co}_{0.7}\text{Zn}_{0.3}\text{Fe}_{2-z}\text{Gd}_z\text{O}_4$ . ..... 123

**Table 23.** Results for  $2^2$  factorial design; the response variable was the average crystallite size  $D$  (nm). ..... 125

**Table 24** Results for CCD design; the response variable was the average crystallite size  $D$  (nm). ..... 126

**Table 25** Maximum magnetization,  $M$ , and coercivity,  $H_{ci}$ , for the coded and experimental levels in  $2^2$  factorial and CCD experimental design applied to the synthesis of  $\text{Co}_{0.7}\text{Zn}_{0.3}\text{Fe}_{2-z}\text{Gd}_z\text{O}_4$ . ..... 128

**Table 26.** Results of the response surface analysis of the  $2^2$  factorial design for the coercivity (Oe). ..... 129

**Table 27.** Results for CCD design; the response variable was coercivity (Oe). ..... 130

## LIST OF FIGURES

- Figure 1.** Semiclassic schematic for origin of the magnetic dipole. The electron circulates around the nucleus, generating a magnetic dipole while the spin is generated due to the electron rotating around its axis..... 7
- Figure 2.** Spin- orbit interaction. On the left, depicts an electron orbiting about the nucleus. In the right, from the electron rest frame, the nucleus appears to be orbiting around the electron and hence producing a magnetic field in the sense indicated<sup>23</sup>..... 8
- Figure 3.** Schematic representation for diamagnetism. In presence of magnetic field, the electrons induce a current and this current has a magnetic field opposite to applied magnetic field, screening the applied magnetic field. .... 10
- Figure 4.** Schematic representation for paramagnetism. In absence of external magnetic field, the spins are randomly; this is because of thermal energy. Furthermore in applied magnetic field the spins tend to align with it. .... 11
- Figure 5.** Schematic representation for ferromagnetism. In absence of external magnetic field, they can exhibit spontaneous magnetization. In presence of external magnetic field the spins tend to align in the direction of applied magnetic field. .... 12
- Figure 6.** Schematic representations for antiferromagnetism. In absence of external magnetic field, they do not exhibit magnetization and the magnetic moment is aligned opposite to one another and the net magnetic moment is zero. In presence of external magnetic field, the magnetization is zero. .... 13
- Figure 7.** Schematic representations for ferrimagnetic ordering. .... 14
- Figure 8.** Shows schematically domain walls in a ferromagnetic material. .... 19
- Figure 9.** Dependence of coercivity with particle diameter<sup>27</sup>. .... 20

<b>Figure 10.</b> Schematic representation of magnetization process explained by magnetic domain <sup>29</sup> .....	21
<b>Figure 11.</b> Schematic representation of the Hysteresis loop, ( $M_s$ ) represent the saturation of magnetization, remanent magnetization ( $M_r$ ), and coercivity ( $H_c$ ) .....	22
<b>Figure 12.</b> Schematic representation of the ferrite structure <sup>27</sup> .....	26
<b>Figure 13.</b> Schematic of $d$ and $p$ orbitals important to the super-exchange interaction <sup>23</sup> .....	28
<b>Figure 14.</b> Cation site preferences for different transition metal ions in A or B sites (Navrotsky and Kleppa 1968) <sup>23</sup> .....	31
<b>Figure 15.</b> Reduction of the Gibbs free energy by forming a solid phase and maintaining an equilibrium concentration <sup>38</sup> .....	34
<b>Figure 16.</b> Change of volume free energy ( $\Delta G_v$ ), surface free energy( $\Delta G_s$ ), and total free energy( $\Delta G$ ), as function of nucleus radius ( $r$ ) <sup>39</sup> .....	35
<b>Figure 17.</b> Process of nucleation and subsequent growth process <sup>42</sup> .....	37
<b>Figure 18.</b> (a) Schematic representation of a ferrofluid and (b) magnetic nanoparticle coated by the surfactant. $R_p$ is the radius of the nanoparticle, $M_d$ is the magnetization and $\delta$ represents the thickness of the surfactant that was adsorbed by the nanoparticle <sup>45</sup> .....	41
<b>Figure 19.</b> Schematic representation of a magnetocaloric pump. The cooler magnetic fluid is entering from the left (zone a), is heated (zone b) and exits on the right (zone c). The magnetic fluid in zone c experiences smaller attractive magnetic forces than in zone a. ....	42
<b>Figure 20.</b> (a) Combinations in the $2^2$ factorial design and (b) CCD design. ....	44
<b>Figure 21.</b> Schematic representation of the nanoparticles synthesis by the conventional co-precipitation method. In the size controlled method, the metal salts (identified as 2nd) are added at different flow-rates using a peristaltic pump. ....	54

<b>Figure 22.</b> (a) Schematic representation of autoclave used, and (b) 475 HP/HT pressure reactor from parr Instruments company.....	55
<b>Figure 23.</b> Scheme for derivation of the Bragg equation <sup>24</sup> .....	58
<b>Figure 24.</b> Siemens D500 X-Ray Diffractometer. ....	60
<b>Figure 25.</b> Schematic representation of the energy levels showing the state involves in Raman signal. ....	61
<b>Figure 26.</b> JEOL 2011 Transmission Electron Microscope. ....	62
<b>Figure 27.</b> Lakeshore 7400Series Vibrating Sample Magnetometer.....	63
<b>Figure 28.</b> Schematic representation of a Vibrating Sample Magnetometer <sup>29</sup> .....	64
<b>Figure 29.</b> Experimental device for Mössbauer spectroscopy.....	65
<b>Figure 30.</b> Splitting of nuclear levels in <sup>57</sup> Fe by a magnetic field. One can observe the isomeric shift and transitions giving rise to the characteristic sextet of Fe.....	67
<b>Figure 31.</b> WEBRES spectrometer operating in the transmission mode, with <sup>57</sup> Co source in a Rh matrix (Ritverc, GmbH).....	67
<b>Figure 32.</b> (a) XRD patterns for CoZn ferrite powders synthesized by the conventional (i.e., without control of flow-rate)co-precipitation method and at different Co atomic fractions, 'x'; (b) average crystallite size as function of 'x', and (c) variation of ferrite lattice parameter as function 'x' value.....	69
<b>Figure 33.</b> Raman spectra for the CoZn (x = 0.5, 0.7, 0.9) ferrite synthesized by the co-precipitation method. The arrow in the middle panel (x = 0.7) indicates the shoulder appearing as discussed in the text. ....	72
<b>Figure 34.</b> (a) M-H curves for CoZn ferrite powders synthesized by the conventional co-precipitation method and different cobalt atomic fraction 'x'; (b) maximum magnetization and coercivity as function of 'x'. ....	74

<b>Figure 35.</b> <i>M-T profiles for CoZn ferrites, <math>x= 0.5,0.8,</math> and <math>0.9</math> synthesized by the conventional coprecipitation method. The arrows indicate the demagnetization temperatures. The external magnetic field was 5 kOe.....</i>	75
<b>Figure 36.</b> <i>Room-temperature Mössbauer spectra for CoZn ferrites, 'x'= 0.5, 0.8, and 0.9, synthesized by the conventional co-precipitation method. ....</i>	76
<b>Figure 37.</b> <i>Mössbauer parameters <math>H_f</math> (Oe) and (RA%) as function of cobalt concentration 'x' for octahedral, (a), and tetrahedral, (b), sites. ....</i>	78
<b>Figure 38.</b> <i>(a) XRD patterns for CoZn ferrite ('x'= 0.5), (b) (<math>x=0.8</math>) powders synthesized with and without (N-F) control of flow-rate. ....</i>	80
<b>Figure 39.</b> <i>(a) XRD patterns for CoZn ferrite ('x'= 0.9) powders synthesized with and without, (N-F), control of flow-rate. (b) TEM image for CoZn nanocrystals synthesized at 'x'=0.9 and 1 mL/min, and (c) average crystallite size as function of flow rate for different Co fraction values.....</i>	82
<b>Figure 40.</b> <i>(a) Complete hysteresis loop for CoZn ferrite ('x'= 0.9) powders synthesized with and without, (N-F), control of flow-rate; (b) maximum magnetization as function of flow rate for different cobalt atomic fractions, 'x', and (c) coercivity as function of flow rate for different cobalt atomic fractions, 'x'. ....</i>	84
<b>Figure 41.</b> <i>M-T curves for CoZn ferrite powders, <math>x=0.5</math>, synthesized with no control of flow-rate (N-F) and 1 mL/min. The arrows indicate the demagnetization temperatures. The external magnetic field was 5 kOe.....</i>	86
<b>Figure 42.</b> <i>Room-temperature Mössbauer spectra for CoZn synthesized at different flow rate conditions for <math>x = 0.5</math>, (a) and <math>x = 0.9</math>, (b). ....</i>	87
<b>Figure 43.</b> <i>Mössbauer parameters <math>H_f</math> (Oe) and (RA%) for CoZn ferrite (<math>x=0.9</math>) as function of flow-rate for the octahedral site, (a), tetrahedral site, (b), and surface, (c). ....</i>	89
<b>Figure 44.</b> <i>(a) XRD spectra for CoZn (<math>x=0.7</math>) ferrite synthesized by hydrothermal method and co-precipitation (<math>T_c</math>); (b) average crystallite size as function of synthesis temperature</i>	

[lower point at 100 °C corresponds to the sample produced by co-precipitation], and (c) lattice parameter as function of the synthesis temperature [lower point at 100 °C corresponds to the sample produced by co-precipitation]..... 93

**Figure 45.** TEM images for Co-Zn ferrite ( $x=0.7$ ) synthesized by: (a) co-precipitation, and hydrothermal method at 100 °C, (b) and 250 °C, (c). Lattice fringes are clearly visible in all cases..... 94

**Figure 46.** (a) M-H curves for CoZn ( $x=0.7$ ) ferrite synthesized by the hydrothermal method at 100oC, 150oC and 250oC; (b) complete hysteresis loops for CoZn ( $x=0.7$ ) ferrite synthesized by the hydrothermal method at 100oC and 250oC; (c) maximum magnetization and coercivity as function of temperature. .... 95

**Figure 47.** M-T profiles for CoZn ferrites ( $x=0.7$ ), synthesized by hydrothermal method at  $T=100$  °C, 150 °C, and 250 °C. The arrows indicate the demagnetization temperatures. The external magnetic field was 5 kOe..... 97

**Figure 48.** (a) XRD spectra for Dy-doped CoZn ( $x=0.7$ ) ferrite synthesized by co-precipitation; (b) average crystallite size as a function of Dy-concentration 'y'. .... 99

**Figure 49.** Raman spectra of non-doped ( $y = 0.0$ ) [lower panel] and Dy-doped Co-Zn ferrite ( $y = 0.01$ ) [upper panel]..... 101

**Figure 50.** (a) M-H curves of Dy doped CoZn ( $x=0.7$ ) ferrite synthesized by co-precipitation method; (b) maximum magnetization and coercivity as function of the Dy atomic fraction, 'y'. The lines are guide to the eyes. .... 103

**Figure 51.** M-T profiles for Co-Zn ( $x=0.7$ ) ferrite at different Dy-concentrations. The dotted lines extrapolate the linear part of the curves and indicate the demagnetization temperature  $T_d$ ..... 105

**Figure 52.** (a) XRD spectra for CoZn ( $x=0.7$ ) ferrite doped with Dy( $y=0.01$ ) synthesized by co-precipitation; (b) average crystallite size as function of flow rate..... 106

**Figure 53.** TEM image of Dy-doped ( $y=0.01$ ) Co-Zn ferrite ( $x=0.7$ ) synthesized by co-precipitation at 20 mL/min flow rate. The dotted frames emphasize two crystallites with approximate sizes of 10nm. The lattice fringes are clearly visible..... 107

**Figure 54.** (a) M-H curves for Dy (0.01) doped CoZn ferrite ( $'x'= 0.7$ ) powders synthesized with and without control of flow-rate at 1 mL/min and 80 mL/min and (b) complete hysteresis loop for the same CoZn ferrite synthesized at 1 mL/min and 80 mL/min. .... 108

**Figure 55.** M-T profiles for Co-Zn ( $x=0.7, y=0.01$ ) ferrite synthesized at different flow rates. .... 109

**Figure 56.** (a) XRD spectra for CoZn ( $x=0.7$ ) ferrite doped with Gd; (b) ferrite average crystallite size as function of Gd-concentration ' $z$ ' ..... 111

**Figure 57.** M-H curves of Gd doped CoZn ( $x=0.7$ ) ferrite synthesized by co-precipitation method..... 113

**Figure 58.** M-T profiles for Co-Zn ( $x=0.7$ ) ferrite with Dy-concentration ( $z=0.0 - 0.2$ ) synthesized by the conventional co-precipitation method. .... 114

**Figure 59.** (a) XRD spectra for CoZn ( $x=0.7$ ) ferrite doped with Dy ( $y=0.01$ ) synthesized by co-precipitation at different flow rates; (b) CoZn ( $x=0.7$ ) ferrite doped with Dy ( $y=0.03$ ). .... 115

**Figure 60.** TEM images of Gd-doped ( $z=0.01$ ) Co-Zn ferrite ( $x=0.7$ ) synthesized (a) without flow rate and (b) by size-controlled co-precipitation method at 80mL/min. The lattice fringes are clearly visible. .... 117

**Figure 61.** M-H curves of Gd doped CoZn ( $x=0.7$ ) ferrite synthesized by conventional (N-F,) and size-controlled method at 80 mL/min and 20mL/min. The Gd atomic fractions were, (a)  $z=0.01$ , and (b)  $z=0.03$ . .... 118

**Figure 62.** M-T profiles for Co-Zn ( $x=0.7$ ) ferrite with Gd-concentration ( $z=0.01$ ) synthesized by conventional and size-controlled co-precipitation method at 20mL/min and 80mL/min. .... 119

**Figure 63.** XRD Patterns corresponding to the coded and experimental levels for the  $2^2$  factorial and CCD experimental design applied to the synthesis of  $\text{Co}_{0.7}\text{Zn}_{0.3}\text{Fe}_{2-z}\text{Gd}_z\text{O}_4$ . 124

**Figure 64.** (a) 3D-surface plot for the average crystallite size,  $D$ , as function of the controllable variables and (b) contour plot for the 3D-surface plot corresponding to  $2^2$  factorial design. .... 125

**Figure 65.** (a) 3D-surface plot for the average crystallite size,  $D$ , as function of the controllable variables and (b) contour plot for the 3D-surface plot corresponding to CCD design. .... 127

**Figure 66.** (a) 3D-surface plot for the coercivity,  $H_{ci}$ , as function of the controllable variables and (b) contour plot for the 3D-surface plot corresponding to  $2^2$  factorial design. .... 130

**Figure 67.** (a) 3D-surface plot for the coercivity,  $H_{ci}$ , as function of the controllable variables; (b) contour plot for the 3D-surface plot corresponding to CCD design. .... 131

# CHAPTER I: INTRODUCTION

## 1.1 Motivation

Worldwide, there is an increasing interest in research involving materials at the nanoscale due to their broad range of applications. One speaks of nanomaterials when their size is between 1-100 nm. Compared to bulk materials, these nanomaterials display new properties. In general, these new properties cannot be predicted based on effects at the large scale. Materials created with tools and techniques at the nanoscale are fundamentally different due to finite size effects, surface or interface dominance and quantum effects in general<sup>1,2</sup>. As soon as nanomaterials are created, one can specifically target new applications and avenues by enhancing or blocking certain new properties. This leads to the so-called designer materials that will most certainly dominate 21<sup>st</sup> century technology. Nanomaterials can be made "2-dimensional", such as ultrathin films or multilayers, "1-dimensional" such as nanorods, nanowires, or nanofibers, or "0-dimensional" such as nanoparticles or clusters.

The synthesis of "0-dimensional" magnetic ferrite nanoparticles is currently an intensive research area due to the verified size-dependence of their functional properties and wide range of applications. There exists a variety of synthesis techniques for nanoparticles which will have influence on properties such as size and magnetic properties. Synthesis techniques include ball milling, microbial synthesis, sol-gel method, microwave method, high-temperature organometallic decomposition, chemical condensation reaction of aqueous ions, polymerizable complex (PC) method based on the Pechini-type reaction route, forced hydrolysis in polyol, alkoxid hydrolysis, citrate route, co-precipitation method, and hydrothermal method. Depending on the targeted application, certain synthesis routes are advantageous over others.

In the case of magnetic materials, new phenomena emerge due to systems containing magnetic nanoparticles. Some of these phenomena are giant magnetoresistance, systems with a high density for information storage, or novel permanent magnets.

Size-controlled synthesis of the nanoparticles can be achieved by variations of the synthesis process such as controlling the solubility of the solution, separating the nucleation and growth stages, using tensio-active agents, controlled addition of precursor materials, temperature, or PH value of the solution<sup>3,4</sup>. To control magnetic properties it is very important to consider the composition of the nanoparticles. For instance, the use of 3d transition metals or 4f rare earths metals guarantee that the nanoparticles will exhibit magnetic properties. Among magnetic particles one finds so-called ferrites, which are iron oxide materials with inverse spinel crystal structure. The ferrites have been very well characterized due to their important magnetic and electric properties<sup>5-9</sup>. When suspending ferrite nanoparticles in aqueous or oleic phase, a ferrofluid is obtained. A ferrofluid is a stable colloidal suspension of magnetic nanoparticles. In order to achieve stability, there should be no dipolar interaction between the nanoparticles, which is achieved by covering the surface with a surfactant or tensioactive agent such as oleic acid. The nanoparticle size plays an important role in determining magnetic properties and mechanical properties of the ferrofluid. Suitable nanoparticles for ferrofluids are in general small, chemically stable and preferably having a single magnetic domain.

Currently there exist many applications using ferrofluids. In biological applications new ventricular assist devices<sup>10</sup>, cell separation devices<sup>11</sup>, cancer treatment by hyperthermia<sup>12</sup> or drug delivery exist. Commercial applications include galvanometers and inclinometers<sup>13</sup>. Magnetocaloric applications include magnetocaloric pump and refrigeration systems<sup>14,15</sup>.

The magnetocaloric pump makes it possible to circulate a magnetic fluid without moving parts<sup>16</sup>. To achieve this it is necessary to have a heat source and an external magnetic field. The heat source can be another hot electronic device that requires cooling and therefore can be cooled using the magnetocaloric pump. This cooling effect is possible utilizing the magnetocaloric effect, where magnetic materials lose their magnetization when heated toward a critical temperature, the so-called demagnetization temperature. In our case, the magnetic material is the ferrofluid. Initially, the cool ferrofluid is attracted toward an external constant magnetic field. When approaching the heat source, the magnetization of the ferrofluid decreases and therefore the warm ferrofluid feels less attraction to the magnetic field and is replaced by cool ferrofluid that feels a stronger attraction. The difference in magnetization generates a pressure gradient that ultimately is responsible for the ferrofluid motion<sup>14,17</sup>. Furthermore, a ferrofluid exposed to a magnetic field, undergoes large changes in its viscosity.

As mentioned above, by controlling the nanoparticles size, its magnetic properties can be varied, such as the magnetization, coercivity, demagnetization temperature, etc. Based on this, the principal objective in this work is to obtain magnetic nanoparticles with certain properties that can be used for the magnetocaloric pump. The optimal properties are: high saturation magnetization ( $M_{\max}$ ), demagnetization temperature ( $T_d$ ) close to the maximum operating temperature of machines, low coercivity ( $H_{ci}$ ), and high pyromagnetic coefficient ( $\partial M/\partial T$ ). A variety of different ferrites have been studied, such as  $Mn_xFe_{1-x}Fe_2O_4$ , with reported demagnetization temperatures of 75 °C and 325 °C with average crystal size between 6nm and 20nm<sup>18</sup>. Reported values for MnZn ferrites are demagnetization temperatures of 360 °C and 165 °C, saturation magnetization between 34emu/g and 42emu/g with average crystal size of 9nm and 11nm<sup>3</sup>, respectively. The CoZn ferrites on the other hand show higher demagnetization

temperatures as compared with MnZn, however also higher maximum magnetization. Reported magnetization temperatures are 415 °C and 267 °C, maximum magnetization of 54emu/g and 40emu/g with average crystal size of 12nm and 8nm, respectively<sup>19</sup>. Taking into account the abovementioned reported properties, for this work the CoZn ferrites are chosen. The idea is to produce a nanomaterial with a suitable response to the change in temperature, i.e.  $\partial M/\partial T$ . To achieve this, during the synthesis process a variety of parameters can be controlled, such as the addition of metal salts, doping with rare earths metals (Dy or Gd), synthesis temperature, and pressure.

On the other hand, once the factors and variables controlling the synthesis process have been established, one can apply the concepts of the design and optimization of experiments. In this case, the aim is to optimize the desired system properties, thereby reducing materials and costs in the process. In the present work, the so-called Central Composite Design (CCD) was used. The CCD is a statistical design which is balanced, modular, and economic and which allows to determine the interaction between the variables. Optimization is defined as an improvement over the original design within the established limits<sup>20</sup>. In real experiments the materials and time are limited and therefore an optimization strategy is chosen, which will minimize the used materials costs and experimental trials. For this purpose, the method of optimization is a metamodel based on an optimization algorithm<sup>21</sup>. This algorithm has been corroborated and found to be effective in stochastic and deterministic simulations.

## 1.2 Aim of study

### **Main Objective**

Determine the influence of composition and crystal size on the magnetic and structural properties of mixed ferrites for potential magneto-caloric applications.

### **Specific Objectives**

- a. Optimize the synthesis conditions for various magnetic ferrite nanoparticle systems (Co Zn and RE doped Co-Zn ferrites) by utilizing conventional and size-controlled co-precipitation methods in aqueous phase.
- b. Determine the effect of aqueous processing conditions on the structural and functional (magnetization, coercivity, demagnetization temperature and pyromagnetic coefficient) properties of the materials at the nanoscale.
- c. Determine the effect of hydrothermal processing conditions on the structural and functional (magnetization, coercivity, demagnetization temperature and pyromagnetic coefficient) properties of the materials at the nanoscale.
- d. Identify, propose and discuss mechanisms involved with the magnetic properties of selected systems at the nanoscale.

## CHAPTER II: THEORETICAL BACKGROUND

### 2.1 Magnetism and Magnetic Materials

Magnetic properties of materials originate from the orbital motion of the electrons and spin motion of the electrons (see Fig.1). The quantized nature of the electron motion leads to the fundamental unit of the magnetic dipole, the Bohr magneton ( $\mu_B$ ).

In simplified terms it can be considered that the electrons have orbital motion about their nuclei, which is equivalent to an electric current (the electron is moving in opposite direction of the current), by Ampere's law such a current loop has a magnetic dipole moment:

$$\boldsymbol{\mu}_l = i\mathbf{a} = -\frac{ev}{2\pi r}\mathbf{a} = -\frac{e\hbar}{2m}\mathbf{l} \quad (1)$$

where  $\mathbf{a}$  is the area vector of the loop,  $\hbar\mathbf{l}$  is the angular momentum vector of the orbiting electron ( $|\hbar\mathbf{l}| = mvr$ ) and  $|\mathbf{a}| = \pi r^2$ ,  $\hbar$  is the natural unit for the orbital angular momentum of atom. From here the natural unit for the magnetic moment  $\mu_B$  is obtained<sup>22</sup>

$$\mu_B = \frac{e\hbar}{2m} = 9.127 \times 10^{-24} \text{ JT}^{-1}$$

There is also a magnetic moment,  $\boldsymbol{\mu}$  associated with the (spin) intrinsic angular momentum ( $\hbar\mathbf{S}$ ) of the electron:

$$\boldsymbol{\mu}_S = -g\mu_B\mathbf{S} \quad (2)$$

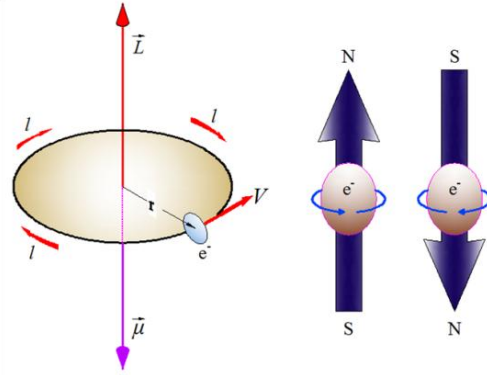


**Figure 1.** Semiclassical schematic for origin of the magnetic dipole. The electron circulates around the nucleus, generating a magnetic dipole while the spin is generated due to the electron rotating around its axis.

where  $g$  is the Landé factor;  $g = 1$  for the purely orbital magnetic contribution, and  $g = 2$  for the spin magnetic contribution. Comparison of eqs (1) and (2), the spin angular momentum is twice as effective in generating a moment as the orbital momentum.

The total magnetic dipole moment of the atom is:  $\mu_J = -\mu_B(\mathbf{L} + 2\mathbf{S})$ , here  $\hbar\mathbf{L} = \hbar\sum\mathbf{l}$  and  $\hbar\mathbf{S} = \hbar\sum\mathbf{s}$  being the sum over the electrons in the atom,  $\hbar\mathbf{L}$  and  $\hbar\mathbf{S}$  are the total orbital angular and spin angular momentum of the atom. **Permanent dipole moments only occur in atoms or ions with incomplete shells ( $L \neq 0$  and  $S \neq 0$ ).**

The angular momentum of spin and orbital cannot be independent of each other, due to spin-orbit interaction (or L-S coupling), which is important for a host of magnetic phenomena that are key to most applications of magnetic materials.

The L-S interaction describes the effects of an electron's orbital motion on its spin. In Fig. 2 one observes that in the reference frame of the electron, the nucleus circles around the electron producing a magnetic dipole field. This magnetic field in turn couples to the spin of the electron and generates the L-S interaction, where  $\mathbf{J} = \mathbf{L} + \mathbf{S}$  with eigenvalues  $L(L + 1)$ ,  $S(S + 1)$ , and  $J(J + 1)$ . The values of  $L$ ,  $S$ , and  $J$  can be found by applying Hund's rules:

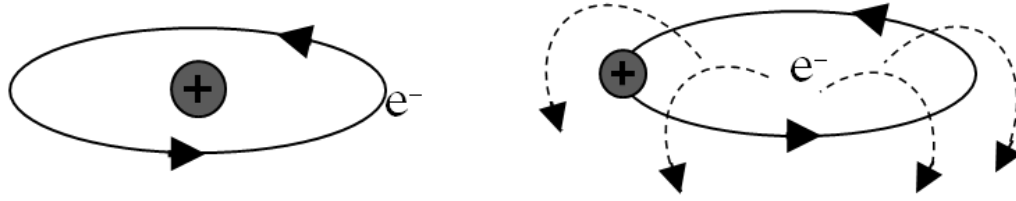


**Figure 2.** Spin- orbit interaction. On the left, depicts an electron orbiting about the nucleus. In the right, from the electron rest frame, the nucleus appears to be orbiting around the electron and hence producing a magnetic field in the sense indicated<sup>23</sup>.

- $S$  takes the maximum value allowed by the Pauli exclusion principle.
- $L$  takes the maximum value consistent with the value of  $S$ .
- $J = |L - S|$  for shells less than half-full and  $J = |L + S|$  for shells more than half-full.

For isolated atoms Hund's rules determine the formation of an atomic magnetic moment for incompletely filled orbitals. This is a reflection of the intra-atomic exchange interaction. There are other interactions that occur between the atoms in a solid, interatomic exchange interaction, that describes when and how these atomic moments couple parallel or antiparallel with each other<sup>24</sup>. To account for alignment between atomic magnetic moments in solids despite strong thermal disordering effects it is postulated that an internal or molecular field  $H_{mol} = \lambda M$ , where  $\lambda$  is proportional to the sum of the exchange energy with all the other spins in the solid. This theory was postulated by Pierre Weiss. This theory has limitations, because to explain the strength of the alignment,  $H_{mol}$  is assumed to have a high value  $\sim 10^3 T^{23}$ , which is large and not possible to be obtained.

In order to understand magnetism it is needed know the Coulomb repulsion between electrons and the constraints imposed by the Pauli's exclusion principle. The wavefunction

of two electrons must be antisymmetric under the exchange of all electron coordinates, space and spin.

The antisymmetry of the wavefunction therefore tends to keep electrons of parallel spin apart so that the expectation value of the Coulomb repulsion energy,  $\frac{e^2}{4\pi\epsilon_0} |r_1 - r_2|$  is smaller for parallel spins than for antiparallel spin, this exchange interaction can be represented by  $-2\mathcal{J}S_1S_2$ , where  $\mathcal{J}$  is the exchange integral and it follows that  $\mathcal{J} > 0$  implies parallel alignment of the spin (ferromagnetic order). A negative value,  $\mathcal{J} < 0$ , favours antiparallel spins and thus antiferromagnetic ordering. This type of exchange interaction is direct exchange, which cannot explain the magnetic order in rare earths. In the rare earth metals there is little overlap of the  $4f$  wavefunctions on neighboring atoms. Here, the magnetic order is explained by indirect exchange interaction. For metal oxides, the exchange interaction is called super-exchange interaction, which occurs in the presence of oxygen atoms between two transition metal ions. The super-exchange interaction is a consequence of the different symmetries of  $p$  and  $d$  states.

As there are many atoms in the solid and usually more than one electron on each atom contributes to the magnetism, the exchange energy of the entire solid is obtained by summing over electron pairs and reads for the Heisenberg Hamiltonian  $\mathcal{H} = -\sum_i \sum_{j \neq i} 2\mathcal{J}_{ij} S_i \cdot S_j$ , where  $2\mathcal{J}_{ij} S_i \cdot S_j$  is the contribution from atoms  $i$  and  $j$ .

In conclusion, orbital and spin angular momentum can contribute to the magnetic moment of the atoms (with unfilled energy levels) in a magnetically ordered solid and can explain paramagnetism in solid compounds for ions, but is not sufficient to explain the other types of magnetic order in the solids as discussed below.

## Diamagnetism and Paramagnetism

When an external magnetic field ( $H_{ext}$ ) is applied to any material it causes an induced electromotive force (emf), which accelerates electrons within the material. The resulting electric current is in such a direction as to reduce (oppose) the applied field and persists when the magnetic field  $H_{ext}$  is maintained at a constant value. The material acquires a magnetization ( $M$ ) in opposite direction (Fig. 3); this phenomenon is known as diamagnetism.

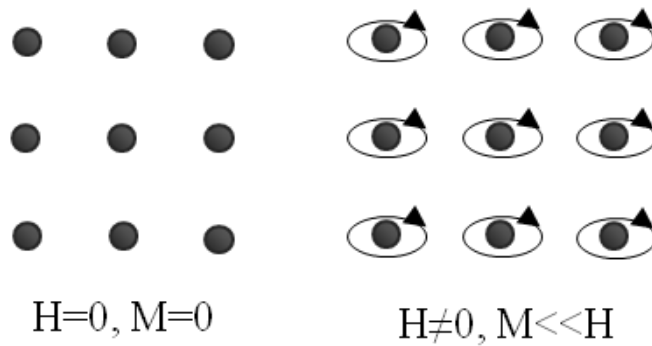


**Figure 3.** Schematic representation for diamagnetism. In presence of magnetic field, the electrons induce a current and this current has a magnetic field opposite to applied magnetic field, screening the applied magnetic field.

In materials in which some or all atoms possess a permanent magnetic dipole moment in the absence of an applied field are called paramagnetic. In  $H_{ext} = 0$  the atomic moments are randomly oriented and do not exhibit a net magnetization due to thermal effects. In small fields there is competition between ordering and thermal disorder, but on average there are more moments with components parallel to the field than antiparallel to it (Fig. 4).

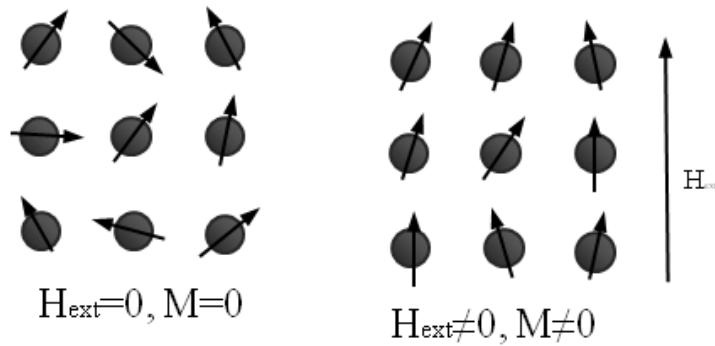


**Figure 4.** Schematic representation for paramagnetism. In absence of external magnetic field, the spin are randomly; this is because the thermal energy. Furthermore in applied magnetic field the spin tend to align to them.

### Ferromagnetism

In the presence of ferromagnetic order, the magnetic moments are ordered and contribute to the spontaneous magnetization. The resulting magnetization exhibits saturation and hysteresis. The magnetic moments are aligned in the direction of the applied external magnetic field (Fig. 5), when the field disappears, the material retains a certain magnetization called remnant magnetization ( $M_r$ ). The magnetization disappears above a certain critical temperature ( $T_c$ ), called the Curie temperature, where the material becomes paramagnetic. This behavior can be encountered in metals and alloys.

The metals form covalent or metallic bonds, which are formed between two atomic orbitals with similar electronegativities ( $E_A \approx E_C$ ) satisfying symmetry and overlap conditions [references]. In the covalent bond, the charge is delocalized from each of the atomic sites and builds up between the atoms. The electronic structure of the transition metals (with  $d$ -electrons) is considered as free-electron like or atomic like. In some cases it turns out to be more free-electron like while in other cases it's more atomic like<sup>23,25</sup>.

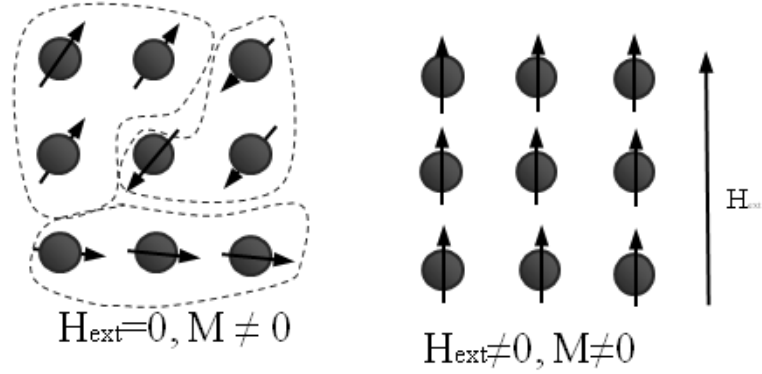


**Figure 5.** Schematic representation for ferromagnetism. In absence of external magnetic field, can be exhibit expontaneous magnetization. In presence external magnetic field the spins tenden to alined in the direction of applied magnetic field.

The Heisenberg exchange interaction (electron-electron interaction) is defined for localized electrons that interact only weakly. It is used to describe ferromagnetism ( $J_{ij} > 0$ ) or antiferromagnetism ( $J_{ij} < 0$ ) in metals, however, is not sufficient to explain all features in detail.

### Antiferromagnetism and Ferrimagnetism

Chemical interaction in materials with polar bonding is formed in materials with significantly different electronegativity ( $E_A \neq E_C$ ), such as in compounds  $A_xC_{1-x}$ , where  $A$  and  $B$  represent anion and cation, respectively. The orbitals must also satisfy symmetry and overlap conditions in order to form a bond. In the polar bonding the charge is transferred from the orbital of higher energy (lower electronegativity, the cation) to that of lower energy (the anion). This type of bonding occurs in oxides<sup>23</sup>. The interacting species can be treated as charged atoms with highly localized atom-like electronic states<sup>26,27</sup>.

The Heisenberg exchange interaction ( $\mathcal{H} = -2J\sum S_i \cdot S_j$ ) is used to describe the tendency of neighboring localized magnetic moments to align parallel ( $J_{ij} > 0$ ) or antiparallel ( $J_{ij} <$

0). This interaction depends on orbital overlap. For the transition metal oxides the magnetism is governed by a different exchange, called super-exchange interaction, which is also a consequence of the Pauli exclusion principle founded on the antisymmetric nature of the electronic wavefunction. The electron- electron interaction present in oxides is generally weak.

In antiferromagnetic order, the magnetic moments are ordered in an antiparallel arrangement due to the exchange energy being negative ( $J_{ij} < 0$ ), with zero net moment at temperatures below the ordering, this temperature is called Neel temperature. Due to the zero net moment, no magnetic saturation occurs when an external magnetic field ( $H_{ext}$ ) is applied. The lattice of the magnetic atoms is divided into two identical sublattices, A and B, such that in the ordered state the mean magnetic moment on the sites of the A sublattice is antiparallel to that on the B sublattice (Fig. 6).

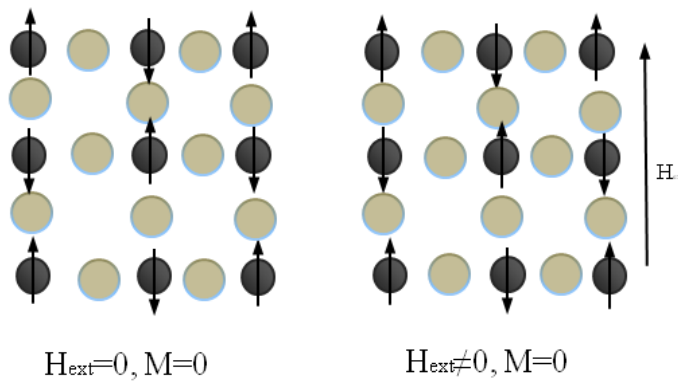


**Figure 6.** Schematic representations for antiferromagnetism. In absence of external magnetic field, no exhibit magnetization and the magnetic moment is alined opposite one and others and the net magnetic moment is zero. In presence of external magnetic field, the magnetization is zero.

Ferrimagnetic ordering is intermediate between ferromagnetic and antiferromagnetic ordering. A ferrimagnetic material, in simply terms, is one in which the magnetic moment of the atoms on different sublattices opposes as in antiferromagnets (A and B sublattices), but the opposing moments are unequal and a spontaneous magnetization remains. Analogous to the ferromagnetic phase the ferrimagnetic phase consists of magnetically saturated domains, which exhibit magnetic saturation and hysteresis. The magnetization disappears above a certain critical temperature ( $T_c$ ), also called the Curie temperature, above which the material becomes paramagnetic. In this investigation we use the terminology of demagnetization temperature ( $T_d$ ). Figure 7 shows the magnetic moment of ferrimagnetic materials without magnetic field applied.

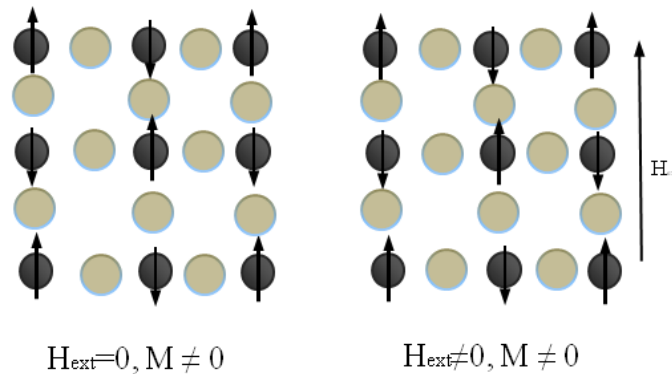


**Figure 7.** Schematic representations for ferrimagnetic ordering.

Ferrimagnetic materials are ionic solids, meaning they are electrically insulating. The most important ferrimagnetic substances are double oxides of iron and the so-called ferrites. (This will be discussed in section 2.1.9 in more detail). Neel has given a simple model to explain this type of spin order based on a Weiss molecular field theory.

## Magnetic Anisotropy

Magnetic anisotropy means that the magnetic properties depend on the direction in which they are measured. This property affects strongly the shape of the hysteresis loop. A thorough knowledge of anisotropy is thus necessary for understanding the magnetic materials. There are several types of anisotropy: (i) crystal anisotropy, (ii) shape anisotropy, (iii) stress anisotropy (which is due to magnetic annealing, plastic deformation, and irradiation), and (iv) exchange anisotropy. Of the abovementioned types, only crystal anisotropy is intrinsic to the materials, all the other are extrinsic or induced.

Crystalline anisotropy is not solely a cause of the anisotropy of the magnetic dipole interaction. But the magnetic moment can “distinguish” between different crystallographic directions by the coupling of the spin part of the magnetic moment to the electronic orbital shape and orientation (spin-orbit coupling) as well as the chemical bonding of the orbital on a given atom with the local environment (crystalline electric field). If the atomic orbital has zero angular momentum  $\langle L_z \rangle = 0$  (spherical charge distribution), it is independent of the symmetry of the crystal field. Here does not occur a coupling between the direction of the spin and the orbital angular momentum ( $L.S = 0$ ). Furthermore, if  $\langle L_z \rangle \neq 0$ , the orbital may assume any orientation in a spherically symmetric crystal field but in a crystal field with lower symmetry the orientation will be in certain preferential directions. In these cases ( $L.S \neq 0$ ), the spin will prefer a specific orientation relative to  $L$ .

When there is magnetic anisotropy, the application of a magnetic field will cause a torque on the magnetic dipole moment  $\mu_L$  but in addition  $S$  may be coupled to  $L$  and two responses can be distinguished. On one hand a crystal field energy  $D$  is generated (coupling of  $L$  with the lattice), in which case  $D > L.S$  and  $\mu_S$  will show a weakly anisotropic response to  $H_{ext}$ ,

while  $\mu_L$  is fixed in direction by the crystal field energy  $D$ . This occurs in 3d transition metals and alloys. On the other hand spin-orbit coupling is generated (coupling  $L$  to  $S$ ) in which case  $D < L.S$ ; this happens typically in rare earth systems where  $\mu_J = \mu_L + \mu_S$  will respond to  $H_{ext}$ , but the pull of the crystal field may be strong if it is of low symmetry. If there is high magnetocrystalline anisotropy and the moment is rotated relative to the crystal, the rotation of the anisotropic orbital charge distribution causes large anisotropic strain. For example in Gd with  $4f^7$  and  $\langle L_z \rangle = 0$ , the spin-orbit interaction vanishes. For the existence of magnetic anisotropy the following conditions are required: an asymmetric crystal field, non-zero orbital angular momentum for the highest occupied electronic state (so that the orbital senses the orbital crystal field symmetry), and a non-zero spin-orbit interaction for the spin to couple to the crystal field<sup>23</sup>.

The strength of the anisotropy of the crystalline electric field determines the strength of the magnetic anisotropy that an ion in that field can exhibit. Having a single magnetic ion exhibiting anisotropy in a non-magnetic environment (single-ion anisotropy), can be distinguished from anisotropic exchange between two magnetic ions.

For the transition metal ions, magnetic anisotropy is usually treated by examining the crystal field splitting of the valence states of the magnetic ion of interest and adding spin-orbit coupling as a perturbation. In Figure 2.8 are shown the d-orbital wave functions for the cubic crystal field of octahedral symmetry, the  $d_{z^2}$  and  $d_{x^2} - d_{y^2}$  orbitals, whose electronic wavefunctions point toward the six neighboring sites. They take on a different energy relative to the three  $d_{xy}, d_{yz}, d_{zx}$  orbitals, which are directed between neighboring sites. This energy shift is due to the Coulomb interaction between the electronic charge distributions on the various orbitals and that on the neighboring ions. As result, the 3d levels

at an octahedral or tetrahedral site split into a triply degenerate energy level and doubly degenerate energy level.

Spinel ferrites have the potential for creating strong anisotropy with an anisotropy constant of  $K_1 = 4.1 \times 10^{-6}$ . Incorporation of a small concentration of  $\text{Co}^{2+}$  in the  $\text{Fe}_3\text{O}_4$  lattice causes a change in the easy axis from  $\langle 111 \rangle$  to  $\langle 100 \rangle$ . The  $\text{Co}^{2+}$  occupies the octahedral site in the ferrite structure leading to a triply degeneration of the ground state with non-zero orbital angular momentum. Figure 9 shows the environment about the octahedral site in the spinel structure. The six neighbors (oxygen) account for the octahedral symmetry, the cubic symmetry alone would not allow for the strong anisotropy exhibited by Co-ferrites. The next six cations, have a trigonal arrangement about the  $\langle 111 \rangle$  axis. These second neighbors lower the crystal field symmetry enough to break the degeneracy of the  $t_{2g}$  triplet state. The three  $d_{xy}$ -like states recombine to form three new orbitals compatible with trigonal symmetry (the  $3p$  states and  $s$  states combine in tetrahedral environments to form  $sp^3$  hybrid orbitals). The result is a singlet state with charge distribution concentrated along the trigonal axis and a doublet with charge distribution in the plane perpendicular to the trigonal axis.

When the dimension is reduced, such as for nanoparticles, there is an increase in the surface-to-volume ratio leading to an increasing fraction of the total crystal volume that consists of surface atoms. The surface atoms experience a lower symmetry environment with respect to bulk atoms and this asymmetry is known as surface anisotropy<sup>28</sup>.

## **Magnetic Domains**

Most ferromagnetic and ferrimagnetic materials do not exhibit a spontaneous magnetization. Only when placed in an external field or near a permanent magnet do they respond and reveal their magnetism. The demagnetization of soft magnetic materials (having a low magnetization) is attributed to the formation of magnetic domains inside the material, which are regions that are magnetized in different directions so that the net magnetization is nearly zero. These regions are known as magnetic domains. This happens because of the magnetic dipole interaction between the spins is much weaker than the short range exchange interaction which aligns neighboring spins. However, over short distances, the magnetic dipole interaction forces neighboring regions to have opposite magnetization<sup>27</sup>. Magnetic domains are separated by domain walls, which are interfaces between them. The transition between the net magnetic moments in different domains occurs usually at an angular displacement of  $90^\circ$  or  $180^\circ$ <sup>29</sup>. For understanding the magnetic domain walls and their motion a variety of different magnetic energy densities must be accounted for: (i) Exchange energy, which tends to keep adjacent magnetic moment parallel to each other. This energy expresses the energy cost of a change in the direction of magnetization;. (ii) Magnetostatic energy, which arises mainly from having a discontinuity in the normal component of magnetization across an interface. It is a form of anisotropy due to the sample shape and is often uniaxial in symmetry; (iii) Magnetocrystalline anisotropy, which describes the preference for the magnetization to be oriented along certain crystallographic directions; (iv) Magnetoelastic energy, which describes that part of magnetocrystalline anisotropy that is proportional to strain. The thickness of a wall is a compromise between the opposing influences of exchange energy and magnetocrystalline anisotropy energy.

Domain structure has its origin in the possibility of lowering the energy of the system by going from a saturated configuration with high magnetic energy to a domain configuration with a lower energy<sup>24</sup>

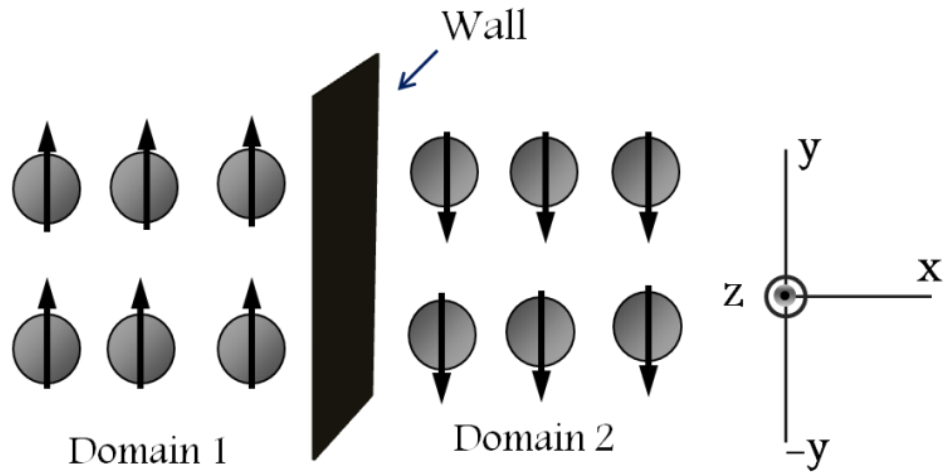


*Figure 8. Shows schematically domain walls in a ferromagnetic material.*

### Single domains

When the size of the nanoparticles is reduced below a critical value, they will not contain domain walls and so will consist only of a single domain, which can be understood based on two arguments. If the size of the particle falls below the thickness of a domain wall, no two domains can exist. On the other hand, the magnetic energy of the particle decreases with the volume, while the wall energy decreases with the area<sup>27</sup>. Accordingly, the development of magnetic walls will not be favored below a certain particle diameter. A typical single domain nanoparticle could have a diameter of the size less than about 100 atoms<sup>30</sup>.

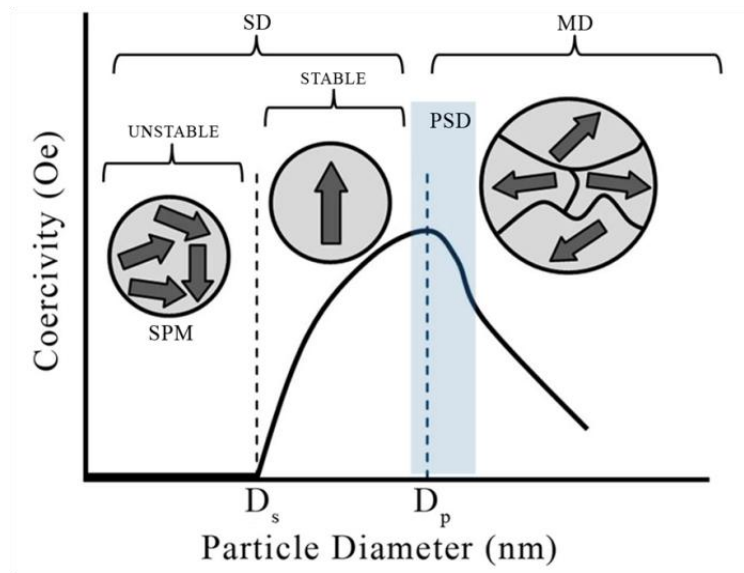


*Figure 9. Dependence of coercivity with particle diameter<sup>27</sup>.*

### **Magnetization Curve and Hysteresis Loop**

Magnetic materials internally are composed of small regions, so-called domains within each of which the local magnetization is saturated. In the absence of an applied magnetic field, the magnetization can be randomly oriented. In the presence of a low magnetic field, the magnetization process occurs with a growth of domains aligned with the field (to minimize the field energy) and a decrease of domains aligned opposite to the direction of the magnetic field. Furthermore, when a strong magnetic field is applied the domain magnetization rotates toward the direction of the magnetic field. In this case the atomic magnetic moments within an unfavorably aligned domain overcome the anisotropy energy and rotate from their original direction into one of the crystallographic easy axes, which is nearest to the field direction<sup>29</sup>. Figure .10 shows the magnetization process explained in terms of magnetic domains. Another factor important for the occurrence of magnetization is the exchange interaction between spins favoring parallel alignment.

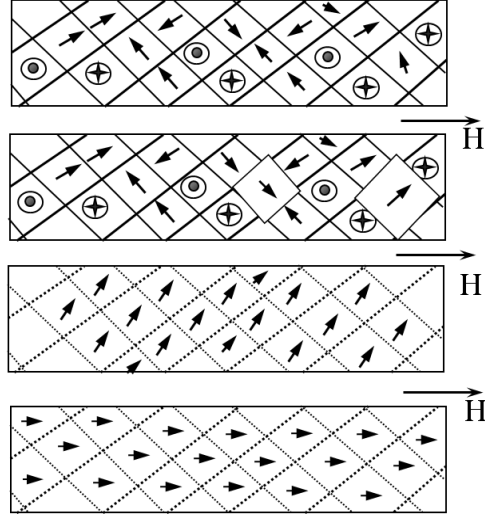


**Figure 10.** Schematic representation of magnetization process explained by magnetic domain<sup>29</sup>.

The magnetization process can be seen in the M-H curve; a typical magnetization curve can be divided into three regions: (i) at the lowest fields the material can be reversibly magnetized or demagnetized, (ii) for intermediate fields the material undergoes irreversible domain displacements, while (iii) at high fields the magnetization rotates.

In a sufficiently high field it is possible to reach the saturation magnetization, in which case all magnetic moments are aligned in the direction of the field. When the magnetic field is reduced, the magnetization curve does not follow the same path, giving rise to hysteresis loops of different shapes. The hysteresis loop gives information about magnetic quantities such as remanent magnetization ( $M_r$ ), coercive field ( $H_c$ ), saturation magnetization ( $M_s$ ), etc. Figure 11 shows a typical hysteresis loop. The remanence or remanent magnetization appears when the applied magnetic field is removed. It expresses the fact that permanent magnetic materials can exist. The order of magnitude of ( $M_r$ ) is that of the spontaneous magnetization ( $M_s$ ), but various geometrical or structural features may contribute to decreasing ( $M_r$ ) well below ( $M_s$ ). The coercivity ( $H_c$ ) is usually defined as the

reverse magnetic field that reduces the magnetization to zero. Taking into account the above mentioned, the magnetic materials can be classified in soft and hard magnetic materials. In soft materials the coercivity is below 200Oe, while for the hard materials the coercivity is greater than 200Oe<sup>31</sup>. The coercivity decreases with decreasing impurities and strain in the material, *i.e.*, in a very pure, unstrained single crystal the hysteresis loop typically is narrow.

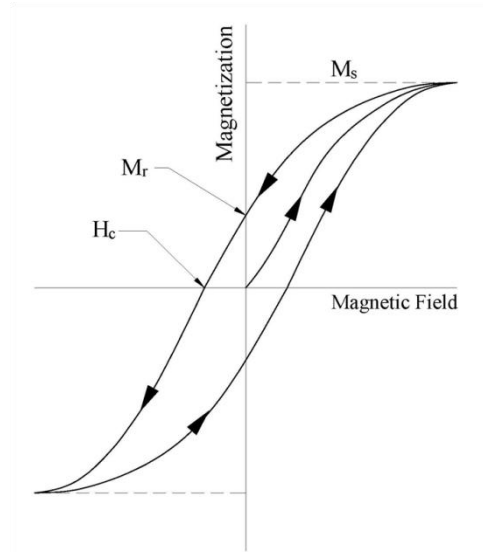


**Figure 11.** Schematic representation of the Hysteresis loop, ( $M_s$ ) represent the saturation of magnetization, remanent magnetization ( $M_r$ ), and coercivity ( $H_c$ .)

## Magnetic Properties and Crystal Size

### Superparamagnetism

This phenomenon is a form of magnetism that appears in ferrimagnetic and ferromagnetic nanoparticles. In very small nanoparticles the magnetization can randomly flip direction under the influence of thermal energy of the system. The typical time between two flips is called the Néel relaxation time.

In superparamagnetism the atomic magnetic moment moves coherently, *i.e.*, the total magnetic moment can be represented by the classic vector  $\mu = \mu_{at}N$ , where  $\mu_{at}$  is the atomic magnetic moment and  $N$  is the number of atoms of the particles. Below a certain size the nanoparticles cannot retain the remanent magnetization, because the moments are randomly oriented by the thermal energy of the lattice. Typically, ferrimagnetic and ferromagnetic materials are in the single-domain superparamagnetic limit when their radius is below about 10nm, in which case they have spherical shape<sup>32,33</sup>.

The temporal relaxation of the magnetization of the particles with a single-domain can be described by an Arrhenius-type law  $M(t) = M_0 \exp(-t/\tau)$ , where  $M_0$  is the initial magnetization and  $\tau$  the decay time. The decay time itself follows  $\tau = \tau_0 \exp\left(\frac{E_B}{K_B T}\right)$ ,

where  $\tau_0$  is associated with the attempt frequency of the magnetic moments between the two opposite directions of the easy axis of magnetization with values between  $10^{-9} - 10^{-10}$  s<sup>34</sup>. The barrier energy  $E_B$  is connected with the product between the volume of the particle and the anisotropy energy ( $E_B = K_\alpha V$ ), where  $K_B$  is the Boltzmann constant.

As nanoparticles exhibit uniaxial symmetry, the magnetic anisotropy is  $E_B = E_B \sin^2 \theta$ , where  $\theta$  is the angle between the magnetization and the easy axis. The minimum and maximum for  $E_B$  occur at  $0^\circ$  and  $180^\circ$  (easy axis). When a magnetic field is applied in the direction of the z-axis, the magnetic energy is  $E_\theta = E_B \sin^2 \theta - \mu H \cos \theta$ .

As mentioned above the magnetization has a certain decay time and an utilized measurement technique will also have its characteristic time scale. The equality of both time scales defines the so-called blocking temperature. In the blocking regime, the magnetization relaxation is slow compared with the measurement time scale. The blocking temperature is proportional

to the volume and anisotropy energy of the nanoparticles,  $T_B \approx \frac{K_a V_0}{25K_B}$ . Below the superparamagnetic limit a nanoparticle has no remanent state and no coercivity.

### **Magnetism of Rare Earth Metal Ions**

In the rare earths the magnetic properties are determined by the number of electrons in the unfilled  $4f$ -shells, which are highly localized, and the crystal field. The electrons in the  $5s$ - and  $5p$ -shells have an indirect effect. It is these electrons which are in contact with the electrons of the neighboring ions. Furthermore, the crystal electric field effect is smaller than the effect from spin-orbit coupling due to the smaller radius of the  $4f$ -electron shell compared to the ionic radius. The outer shells may distort because the environment of the ion and the charge distribution within the  $4f$ -shell is not spherical. This additionally shields the inner  $4f$  electrons from the external crystal field.

Rare earths (RE) ions have more electrons and fill up higher orbitals such as  $4f$  and  $5s$ . Therefore, these ions are larger in size than iron ions. When doping with RE ions the electronic environment changes and hence also the crystal field. One expects that this will influence the magnetic and structural properties of ferrites. The  $\text{RE}^{3+}\text{-O-Fe}^{3+}$  interaction is about one order of magnitude smaller than those found between  $\text{Fe}^{3+}\text{-O-Fe}^{3+}$ , while the  $\text{RE}^{3+}\text{-O-RE}^{3+}$  interaction is even up to two orders of magnitude smaller<sup>35</sup>. The smaller interaction between RE ions is attributed to the abovementioned stronger localization and more shielding of the  $4f$ -electrons. This modified superexchange interaction between RE ions will certainly influence the magnetic properties in ferrites.

## Ferrites

Ferrites have been considered for many years as important for technology and industry, based on their magnetic and electric properties. In order to understand the different properties in the ferrites, the principal characteristics that determine their macroscopic behavior need to be understood first.

Ferrite is an inorganic compound with chemical formula  $XO.Y_2O_3$ , where  $X$  represents a divalent metal cation ( $Co^{2+}, Fe^{2+}, Mn^{2+}, etc$ ) and  $Y$  a trivalent metal cation (generally  $Fe^{3+}$ ) forming ionic bonding<sup>31</sup>. The structure of ferrites consists of a closed-packed face-centered cubic arrangement of the oxygen ions with the cations being distributed in the interstitial sites in between, the lattice constant is about 0.8nm. Figure 12 shows the two interstitial sites A and B, where the metal ions can be accommodated. The tetrahedral A-sites are coordinated with four oxygen ions, whose connected lines form a tetrahedron, while the octahedral B-sites are coordinated by six nearest-neighboring oxygen ions, whose connected lines form an octahedron. A unit cell is formed from 64 A-sites and 32 B-sites. Of the 64 possible tetrahedral sites only 8 are occupied and of the 32 possible octahedral sites only 16 are occupied.

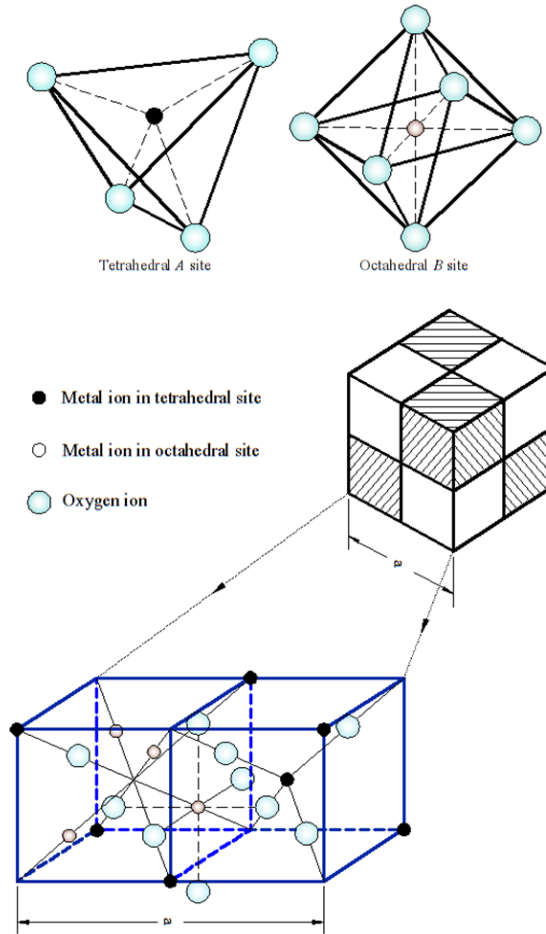


**Figure 12.** Schematic representation of the ferrite structure<sup>27</sup>.

Therefore, in each unit formula only one A-site and two B-sites are occupied. The metal ions have preferential sites, which are determined by the ionic radii, interstitial sizes, temperature, orbital preferences for specific coordination, and valences<sup>23</sup>. One expects the existence of two different ferrite forms, the normal and the inverse. Table 1 shows the radii of several metal ions involved in ferrite formation.

**Table 1.** Ionic radii for selected metal ions usually present in ferrites <sup>31</sup>.

<b>Metal Ion</b>	<b>Ionic Radius (nm)</b>
Mn <sup>2+</sup>	0.091
Mg <sup>2+</sup>	0.078
Fe <sup>2+</sup>	0.083
Fe <sup>3+</sup>	0.067
Co <sup>2+</sup>	0.082
Zn <sup>2+</sup>	0.082
Cr <sup>3+</sup>	0.064
Dy <sup>3+</sup>	0.091
Gd <sup>3+</sup>	0.097

The magnetism in ferrites is governed by super-exchange interaction, which is described in Figure 13. In general, two transition (T) metal ions are separated by ions with outermost electrons in the  $p$  orbital (in this case oxygen). The  $p$  orbital is filled in the ground state and can exchange an electron with each of the adjacent  $3d$  orbital's. Thus the bonding is mostly ionic  $T^{2+}$  and  $O^{2-}$ , but some hopping is allowed. The doubly occupied  $p_x$  orbital has two electrons of opposite spin, the  $3d$  and  $p$  orbital's must exchange electrons, that is some of the excited states of the system must be partially occupied. When the  $p_x$  electron is excited into an empty  $d$  state to form a  $(p - d)\sigma$  or  $\sigma^*$  bond, it leaves behind an electron of opposite spin, which may be exchanged with the  $d$  states of the other T metal ions coupled to this  $p_x$  orbital. The exchange interaction between the spin of two T metal ions on different sites depends on the distance between these ions and the oxygen ions.

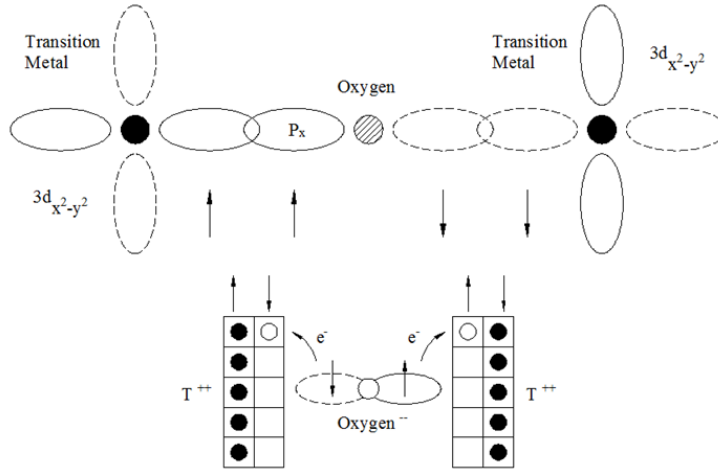


**Figure 13.** Schematic of *d* and *p* orbitals important to the super-exchange interaction<sup>23</sup>.

In the spinel structure, the A-O-B bond has an angle of  $125^\circ$ , the B-O-B bond of  $90^\circ$ , and the A-O-A bond of  $80^\circ$ . The strongest super-exchange interaction is the  $125^\circ$  antiferromagnetic A-B coupling. Considering this fact the major contributor is the A-B interaction<sup>31</sup>.

**Table 2.** Spin configuration of some 3*d*-metal ions and magnetic moment contribution

Metal ion	3 <i>d</i> -orbitals electrons	Spin-only magnetic moment ( $\mu_B$ )
Mn <sup>2+</sup>	↑ ↑ ↑ ↑ ↑	5
Fe <sup>2+</sup>	↑↓ ↑ ↑ ↑ ↑	4
Fe <sup>3+</sup>	↑ ↑ ↑ ↑ ↑	5
Co <sup>2+</sup>	↑↓ ↑↓ ↑ ↑ ↑	3
Zn <sup>2+</sup>	↑↓ ↑↓ ↑↓ ↑↓ ↑↓	0
Cr <sup>3+</sup>	↑ ↑ ↑ ↑	4

Néel explained the ferrimagnetism of ferrites by collinear two inequivalent sublattices A and B sites, the introduction of this asymmetry is responsible for the properties of these

materials. Basically, this may be considered as a generalization of ferromagnetism and antiferromagnetism. As in these cases, the molecular field theory is used here also for treatment of ferrimagnetism<sup>27</sup>.

Néel and Anderson have modified the Weiss theory to take account of the actual structure of crystals and the effective field can be written as  $H_i = H_o + \sum \gamma_{ik} M_k$ . The material is considered to be divided into substructures and  $H_i$  is the field acting on an atom on the  $i$ th substructure,  $\gamma_{ik}$  is the molecular field coefficient for the field exerted on an atom on the  $i$ th substructure by its neighbors on the  $k$ th substructure. For the two sublattices A and B with different species of cations it can be assumed<sup>36</sup>:

$$H_A = -\gamma_{AA}M_A - \gamma_{AB}M_B$$

$$H_B = -\gamma_{BA}M_A - \gamma_{BB}M_B.$$

The exchange integrals  $J_{AB}$ ,  $J_{BB}$  and  $J_{AA}$  are negative and favor antiparallel alignment (antiferromagnetic coupling)<sup>24</sup>. But the interaction A-O-B is the strongest, so that the A spins are parallel to each other and the B spins are parallel to each other, in order that the A spins may be antiparallel to the B spins.

Consider a Co-ferrite which has two  $Fe^{3+}$  ions and one  $Co^{2+}$  ion. From Figure 14 it can be seen that the  $Fe^{3+}$  has a stronger preference to occupy the tetrahedral site and  $Co^{2+}$  to occupy the octahedral site. One of  $Fe^{3+}$  ions occupies the A-site and relegates the other two ions ( $Co^{2+}$  and  $Fe^{3+}$ ) to the octahedral B-sites. Hence, the Co-ferrite has inverse site occupation. It is important to note that  $Zn^{2+}$  has the strongest tendency for A-site occupation among all ions. The distribution of the ions can be represented by  $Fe^{3+} \downarrow [Co^{2+} \uparrow Fe^{3+} \uparrow]O_4$  for the Co-ferrite where the brackets enclose the ions on **B**. Approximately, the spontaneous

magnetization per formula unit thus corresponds to the number of unpaired spins for the  $\text{Co}^{2+}$ . Zn-ferrite on the other hand is a normal spinel according to  $\text{Fe}^{3+} \downarrow \text{Zn}^{2+}(\text{O})[\text{Fe}^{3+} \uparrow]\text{O}_4$ . For the Co-Zn ferrite, the  $\text{Co}^{2+}$  ions are replaced by  $\text{Zn}^{2+}$  which still occupies the A sites with corresponding proportions of  $\text{Fe}^{3+}$  according to  $\text{Zn}^{2+}(\text{O})\text{Fe}_{1+\delta}^3 \downarrow [\text{Co}_{1-\delta}^{2+} \uparrow \text{Fe}_1^3 \uparrow]\text{O}_4$ , where  $\delta$  represents the extent to which the site occupation is normal and varies accordingly to the method of preparation and heat treatment. The stronger AB interaction overcomes the negative BB interaction to impose ferromagnetic order within the B sublattice.

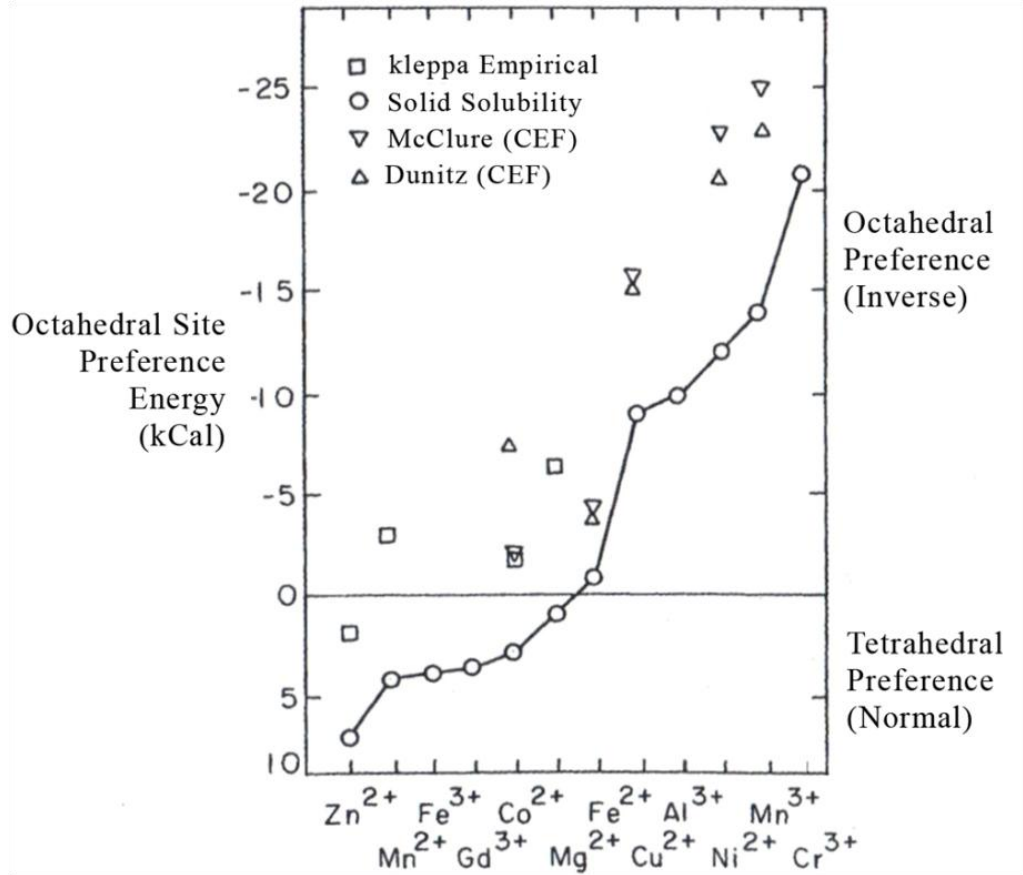


**Figure 14.** Cation site preferences for different transition metal ions in A or B sites (Navrotsky and Kleppa 1968)<sup>23</sup>

## 2.2 Nanoparticles synthesis by co-precipitation

In the co-precipitation method the crystal growth depends on various parameters, the most important being the molecular concentration of the constituents approaching the surface of the crystallite during the process of growth. The liberation of latent heat at the surface makes the local temperature higher than the average temperature of the solution. The surface temperature affects the local molecular concentration at the crystal surface, and hence the crystal growth<sup>37</sup>.

The co-precipitation reactions involve the simultaneous occurrence of nucleation, growth, coarsening, and/or agglomeration. The co-precipitation reactions have the following characteristics: (i) the resulting co-precipitation products are little soluble and are formed under supersaturation conditions, (ii) the formation of the nanoparticles fundamentally depends on the nucleation, (iii) the size, shape, and properties can be affected by secondary processes, such as aggregation and coarsening or Ostwald Ripening, and (iv) the saturation condition is a result of chemical reactions. The co-precipitation reaction can be induced by chemical reactions, which generally lead to reaction products of low solubility, thereby resulting in supersaturation conditions. If more than one element is present, the chemical reactions happen faster. In ternary or quaternary systems multiple species can precipitate simultaneously<sup>2</sup>. The nucleation and growth processes define the size and morphology of the particle. Immediately after begin of the co-precipitation reaction numerous crystallites form, which tend to aggregate forming larger particles to increase thermodynamic stability. In thermodynamics exists a strong tendency of solids to minimize the total surface energy. It has been demonstrated experimentally that the total surface energy and the specific surface area (surface area per unit of volume) increase with decreasing size<sup>3</sup>. This tendency is due to the fact that nanomaterials have a bigger number of atoms on the surface per unit volume, implying that they have a bigger surface area and hence bigger surface energy. The surface energy ( $\gamma$ ) turns out to be the energy required to generate a new unit of surface. In the synthesis of nanoparticles it is possible to control the surface energy by decreasing it, thereby preventing that the nanoparticles grow.

## Thermodynamics of co-precipitation

As mentioned above, the nucleation and growth processes determine the size and morphology of the nanoparticles, which directly influence among others the structural, electrical, and magnetic properties.

### a. Nucleation

In the co-precipitation process the key step is the degree of supersaturation of the solution. Supersaturation occurs if the solute concentration in the solvent exceeds its equilibrium solubility value or the temperature falls below the phase transformation point. A supersaturated solution has a high Gibbs free energy compared with the solution in equilibrium, the total system energy can be lowered through segregation of the solute in the solution. Figure 15 shows the reduction of the total Gibbs free energy of a supersaturated solution through formation of a solid phase while maintaining an equilibrium concentration in the solution. Many authors suggest that the change in the Gibbs free energy is the driving force in the nucleation and growth process<sup>4</sup>. The change in the Gibbs free energy per unit volume of solid phase depends on the solute concentration and is given by the relation<sup>38</sup>:

$$\Delta G_v = -\frac{KT}{\Omega} \ln\left(\frac{C}{C_0}\right) = -\frac{KT}{\Omega} \ln(1 + \sigma)$$

where  $C$  is the solute concentration,  $C_0$  the equilibrium concentration,  $K$  the Boltzmann constant,  $T$  the temperature,  $\Omega$  the atomic volume, and  $\sigma$  the supersaturation, which is given by  $\sigma = \frac{C-C_0}{C_0}$ . From this relation one can deduce that for  $\sigma = 0$  (no supersaturation),  $\Delta G_v = 0$  and no nucleation will take place. When  $C > C_0$ ,  $\Delta G_v$  is negative and nucleation occurs spontaneously. With the nucleation initiating in a supersaturated solution and

assuming a spherical nucleus of radius  $r$ , the Gibbs free energy per volumen can be written

as<sup>38</sup>: 
$$\Delta\mu_v = \frac{4}{3}\pi r^3 \Delta G_v$$

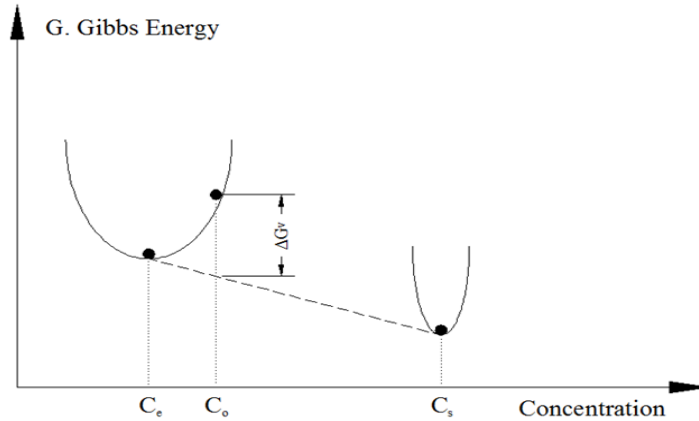


**Figure 15.** Reduction of the Gibbs free energy by forming a solid phase and maintaining an equilibrium concentration<sup>38</sup>.

However, this reduction is counteracted by the introduction of surface energy through the formation of a new phase. As a result the surface energy of the system increases. The surface energy is given by:  $\Delta\mu_s = 4\pi r^2\gamma$ , where  $\gamma$  is the surface energy per unit area. The total change in the chemical potential for the nuclei formation is given by the relation<sup>38</sup>:

$$\Delta G = \Delta\mu_v + \Delta\mu_s = \frac{4}{3}r^3\Delta G_v + 4\pi r^2\gamma$$

As can be seen,  $\Delta G$  depends on the nucleus radius, because of which there exists a critical equilibrium radius  $r^*$ . If the initial nucleus radius is smaller than the critical radius  $r < r^*$ , the nucleus dissolves to reduce the total free energy; on the other hand, if  $r > r^*$  the nucleus is stable and growth continues. Substituting  $r = r^*$  and taking  $\frac{d(\Delta G)}{dr} = 0$  one obtains the

following relations: 
$$r^* = -2\frac{\gamma}{\Delta G_v} \quad \Delta G^* = \frac{16\pi\gamma}{(3\Delta G_v)^2}$$

As can be seen in Figure 16.  $\Delta G^*$  is the energy barrier which the nucleation process has to overcome

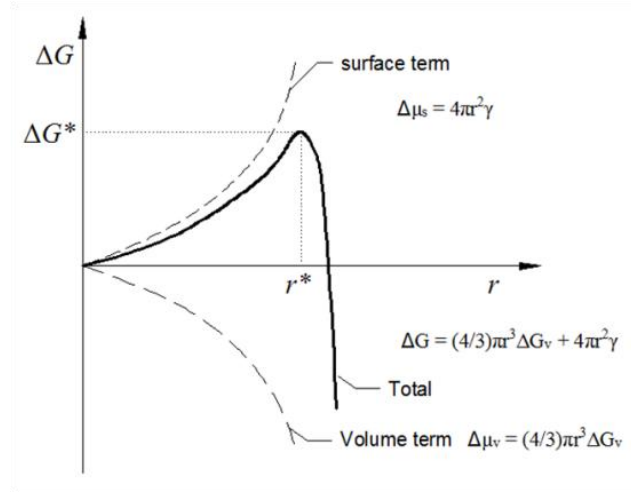


**Figure 16.** Change of volume free energy ( $\Delta G_v$ ), surface free energy ( $\Delta G_s$ ), and total free energy ( $\Delta G$ ), as function of nucleus radius ( $r$ )<sup>39</sup>.

For a supersaturated solution the critical radius represents the limit on how the nanoparticles should be synthesized. Increasing the supersaturation of the system will reduce the critical radius, the Gibbs free energy, and the surface energy. The rate of nucleation per unit volume and unit time  $R_N$  is proportional to the probability that there is a thermodynamic fluctuation of the critical free energy  $\Delta G^*$  given by:  $P = \exp\left(-\frac{\Delta G^*}{KT}\right)$  the number of monomers of the solute per unit volume  $n$ , and the successful jump frequency of solute monomers,  $\Gamma$ , from one site to another, is given by:  $\Gamma = \frac{KT}{3\pi\lambda^3\eta}$ ; where  $\lambda$  is the diameter of the solute monomers and  $\eta$  is the viscosity of the solution. Furthermore the rate of nucleation  $R_N$  is given by<sup>38</sup>:

$$R_N = nP\Gamma = \left\{ \frac{C_0KT}{3\pi\theta\lambda^3\eta} \right\} \exp\left(-\frac{\Delta G^*}{KT}\right)$$

This equation indicates that supersaturation, low viscosity, and low energy barrier favor the formation of a larger number of nuclei and therefore one obtains nuclei of smaller size. For the given concentration.

Before the nucleation process begins, there is a pre-nucleation phase or induction phase starting immediately after the metal salts get in contact with the precipitating agent. In this phase the metal salts start to dissolve initiating a chemical reaction which produces primordial solute species and increases the concentration. When the supersaturation of the solution reaches a critical value ( $C_{min}$ ) over the solubility concentration the nucleation sets in. This critical value of the solubility concentration corresponds to a barrier energy  $\Delta G^*$ , after the initial nucleation  $r > r^*$ , the induction time, the solution goes from a metastable to a stable phase<sup>40</sup>. After this stage the supersaturation of the species in the solution decreases and the change in the Gibbs free energy is reduced. When the concentration falls below the critical concentration, new nuclei stop forming and the species in solution precipitate on the surface of the nuclei already formed, while the growth continues until reaching the solubility concentration. Above the minimum concentration ( $C_{min}$ ) the processes of nucleation and growth occur simultaneously, but at different speeds. Figure 17 shows the process of nucleation and growth of the nuclei.

In the synthesis of nanoparticles with uniform size distribution, the nuclei were formed at the same time having the same or similar size due to similar initial conditions<sup>41</sup>. The process of nucleation occurs abruptly and at very high supersaturation the saturation decreases rapidly until it falls below the minimum concentration, where no new nuclei are formed and the already existing nuclei keep growing until reaching the concentration of solubility.

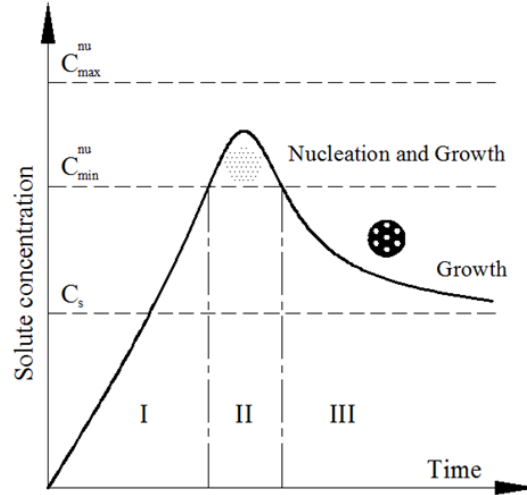


**Figure 17.** Process of nucleation and subsequent growth process<sup>42</sup>.

Up until now the process of homogeneous nucleation was described. There exist, however, another process which occurs when the new phase is formed on top of another material and is known as heterogeneous nucleation. In this case other particles can be added to the system, which act as substrate whose surface favors the formation of the new phase and hence act as catalysts of nucleation. The theoretical description of this mechanism was described starting with obtaining the change in the Gibbs free energy of the nucleation system, corresponding to the formation of the new phase on top of the substrate. This theory is due to G. Cao, obtaining the following mathematical relations for the critical radius ( $r^*$ ) and the barrier energy<sup>38</sup>:

$$r^* = -2 \frac{a_1 \gamma_{vf} + a_2 \gamma_{fs} - a_2 \gamma_{sv}}{3a_3 \Delta G_v}$$

$$\Delta G^* = \left\{ \frac{16\pi \gamma_{vf}}{(3\Delta G_v)^2} \right\} \left\{ \frac{2 - 3\cos\theta + \cos^3\theta}{4} \right\}$$

where  $\gamma_{vf}, \gamma_{fs}, \gamma_{sv}$  are the surface energy or interface energy of the solution-nucleus, nucleus-substrate, and solution-substrate, respectively, while  $a_1, a_2, a_3$  are geometric constants:

$$a_1 = 2\pi(1 - \cos\theta)$$

$$a_2 = \pi \sin^2\theta$$

$$a_3 = 3\pi(2 - 3\cos\theta + \cos^2\theta)$$

It can be seen from the equations that the heterogeneous nucleation takes place easier if the contact angle (angle between the surface and the substrate) is  $\theta = 0^\circ$ , this happens when the substrate material is the same as that of the nuclei to be formed.

### **b. Growth of nuclei**

The most important factors in the growth process are the concentration gradient and the temperature. Depending on these factors primary stable nanoparticles or particles with larger size can be formed. The primary nanoparticles take place in the diffusion limited process and those of larger size in aggregation and coalescence processes that promote secondary growth.

When the solute concentration falls below  $C_{\min}$ , growth takes place and for diffusion growth the rate of growth is given by:

$$\frac{dr}{dt} = DV_m \left( \frac{1}{\delta_i} + \frac{1}{r} \right) (C_b - C_i)$$

Where  $r$  is the radius of the spherical nucleus,  $t$  the time,  $D$  the diffusion coefficient of the monomers towards the nucleus surface,  $\delta_i$  the thickness of the layers over which the concentration changes from  $C_b$ , the solute concentration far away from the growth surface, and  $C_i$  the concentration in the vicinity of the crystal surface<sup>39,40</sup>. The Gibbs-Thompson

relation establishes a connection between the monomer concentration and the crystal growth<sup>43</sup>:

$$C(r)_e \cong C_\infty \left( \frac{1 + 2V_m \gamma}{R_G T} \right)$$

where  $R_G$  is the universal gas constant,  $T$  the temperature, and  $\gamma$  the surface tension at the interface. It is possible to express a relation between the growth rate  $G$  and the rate of supersaturation ( $\sigma$ ):

$$G = k_G \sigma^g$$

where  $G$  is the constant of the ratio of growth, and  $g$  the growth order. The diffusion controlled growth process promotes more uniform particle sizes. When the diffusion of the monomers is very fast, the concentration in the vicinity of the surface of the growing nucleus is equal to the concentration far away ( $C_b = C_i$ ) and the growth is controlled by two surface process mechanisms: mono-nuclear growth, where the growth takes place layer by layer and poly-nuclear growth, where the layers grow almost simultaneously<sup>44</sup>. The mono-nuclear growth depends on the monomer concentration and time, while for the poly-nuclear growth the growth rate only depends on the temperature, i.e., it is constant and takes place when the surface concentration  $C_i$  is very high. A secondary process that can occur, in which kinetic effects dominate over thermodynamic effects, is described by Wilhelm Ostwald. In this process, an unstable state makes a direct transition into a stable state or occurs via intermediate states. The stability of a system is given by its solubility, being more stable the more soluble it is. If the system has two phases with different solubility, the one with higher solubility will crystallize first. Immediately after, the solubility in the vicinity decreases until reaching a critical value. The system is now supersaturated with respect to the phase with lower solubility. The phase that precipitated first remains in a metastable state until the

phase with lower solubility also precipitates (formation of the first crystals in the phase). When this happens, the solubility of the system is going to decrease again and the precipitated crystals from the first phase (higher solubility) become unstable and dissolve to form solution species that precipitate to contribute to the growth of the more stable phase. In other words, during the growth process, the smallest particles are consumed by the bigger ones.

### **c. Termination of growth and nanoparticles stability**

The nanoparticles obtained by precipitation from solutions will be agglomerated unless a stabilizing agent is used. In colloidal dispersions there exist different types of interaction between the particles, among them van der Waals interaction and in the case of magnetic materials also magnetostatic interaction. In the case of nanoparticles, the van der Waals interaction increases due to their small size. There are different mechanisms to achieve stability of the nanoparticles<sup>39</sup>, among the most widely used are electrostatic stabilization (kinetic stabilization) and esteric stabilization (thermodynamic stabilization).

In simplified terms, it is possible to stabilize particles grown from a solution by covering them with ions or molecules, which bring an electric charge to the particles surface generating a Coulomb potential and hence achieve electrostatic stability. For the oxides, the surface charge is mainly derived from the preferential deposition and dissolving of ions. In this case the charge is determined by (positive) protons or negative hydroxyl groups, OH<sup>-</sup> on the surface. With the surface charge density in place, there are electrostatic forces between the charged particles in proximity, which segregate the positive and negative charges. However, due to entropic forces and Brownian motion, the particles tend to distribute homogeneously throughout the solution<sup>39</sup> On the other hand, when using a non-polar solvent

the agglomeration of the particles is avoided by absorption of long molecules of organic acids or thioles. This case corresponds to esteric stabilization.

### 2.3 Ferrofluids and the Magnetocaloric Pump

Ferrofluids are colloidal suspensions made of magnetic nanoparticles dispersed in a carrier liquid (see figure 18). The magnetic nanoparticles are coated by a surfactant/polymer dispersant layer of approximately 2 nm thickness, which prevents agglomeration of the nanoparticles<sup>45</sup>. The surfactant or coating agent must be compatible with the carrier liquid and it must overcome the van der Waals and magnetic forces. When the ferrofluid is exposed to external magnetic fields, the nanoparticles are attracted towards the magnetic field. Thermal energy on the other hand generates random motion that allows the particles to remain dispersed in the fluid. The colloidal magnetic fluid contains on the order of  $10^{23}$  particles per cubic meter, hence interparticle collision are frequent. The proper particle size must be between 3 nm – 15 nm.

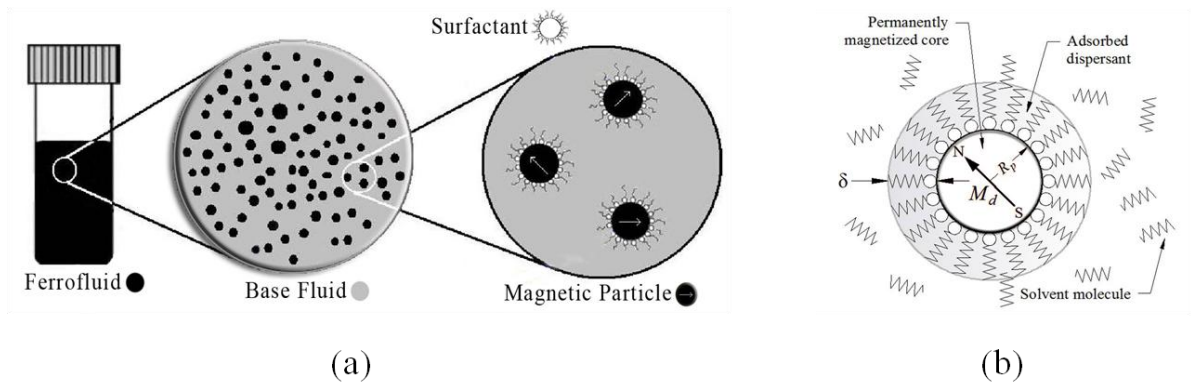


**Figure 18.** (a) Schematic representation of a ferrofluid and (b) magnetic nanoparticle coated by the surfactant.  $R_p$  is the radius of the nanoparticle,  $M_d$  is the magnetization and  $\delta$  represents the thickness of the surfactant that was adsorbed by the nanoparticle<sup>45</sup>.

Ferrofluids retain the properties of a fluid even in high magnetic fields. These fluids can be used in a great variety of applications such as targeted drug delivery<sup>46-48</sup>, magnetocaloric pump<sup>11,14,49</sup>, etc. The magnetocaloric pump is a device that can pump a ferrofluid using only external thermal and magnetic fields. When exposing a column of magnetic fluid to a uniform magnetic field coincident with a temperature gradient, a pressure gradient in the magnetic fluid is set up. As the fluid heats up, it loses its attraction to the magnetic field and is displaced by the cooler fluid. In this way, obtaining fluid propulsion without moving mechanical parts is possible (see Figure 19).

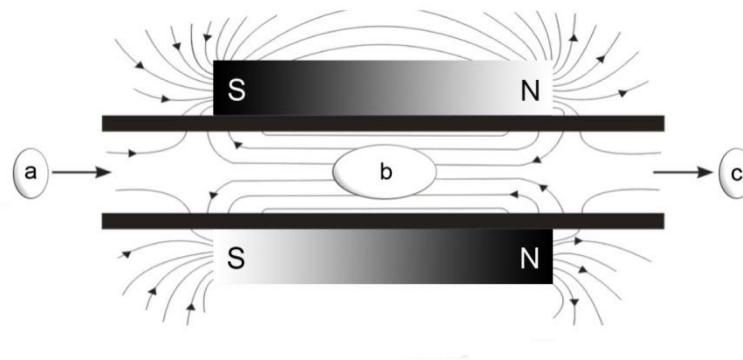


**Figure 19.** Schematic representation of a magnetocaloric pump. The cooler magnetic fluid is entering from the left (zone a), is heated (zone b) and exits on the right (zone c). The magnetic fluid in zone c experiences smaller attractive magnetic forces than in zone a.

## 2.4 Fundamentals of Experimental Design

The application of industrial engineering concepts, such as design of experiments and optimization, to laboratory settings can be useful to researchers to study the effect among the desired variables and optimize the desired properties, therefore reducing costs and material usage. Designing experiments consist of three phases: planing, execution, and analysis, which are excellent for experiments in early stages because it is sequential, followed by optimization of the system.

A strategy of experimentation that is used extensively is the **one-factor-at-a-time** approach, which consists of selecting a starting point, or a baseline set or levels for each factor<sup>50</sup>. In this case all experiments are performed and a series of graphs is usually constructed showing how the response variable is affected by varying each factor with all other factors held constant. The principal disadvantage is that it fails to consider any possible “interaction” between the factors. An interaction is the failure of one factor to produce the same effect on the response at different levels of another factor. Furthermore, the approach that considers any possible interaction of the factors is the **factorial strategy** in which the factors are varied together, instead of one at a time. The most important case of the factorial strategy is the  $2^K$  strategy, which takes K factors (or controllable parameters) with two levels each. The levels of K, for the present work are quantitative, a high and a low level with  $2 \times 2 \times 2 \dots \times 2 = 2^K$  experimental runs. When considering only two factors, i.e., A and B, each experimental run with two levels is called  **$2^2$  factorial design**. For this research the  $2^2$  factorial design is used to determine the influence of the factors (synthesis parameters) in the responses of interest (magnetic and structural properties), with 4 possible combinations and 4 replicas in the center of the square (Figure 20 a) to estimate the error. The data collected was analyzed using MINITAB15. The analysis of variance (ANOVA) is used to quantify and evaluate the importance of possible sources of variation. It provides the basic information necessary for making statistical inference either in terms of tests of hypotheses (or tests of significance) or confidence interval estimation (F-test). The statistical results will have to be interpreted in terms of the originally formulated hypotheses. A test of a hypothesis is a rule to determine whether a hypothesis is rejected or not and it is based on sample statistics called test statistics. The hypothesis is usually stated in null form, since these are the only easily

testable statements. The p-value of a test is the probability of obtaining a value of the test statistic that is at least as extreme as the calculated value when the null hypothesis is true. It is the smallest significance level at which the null hypothesis can be rejected. Thus, if the agreed-upon value of  $\alpha$  is less than the observed p value the null hypothesis is not rejected<sup>51</sup>.

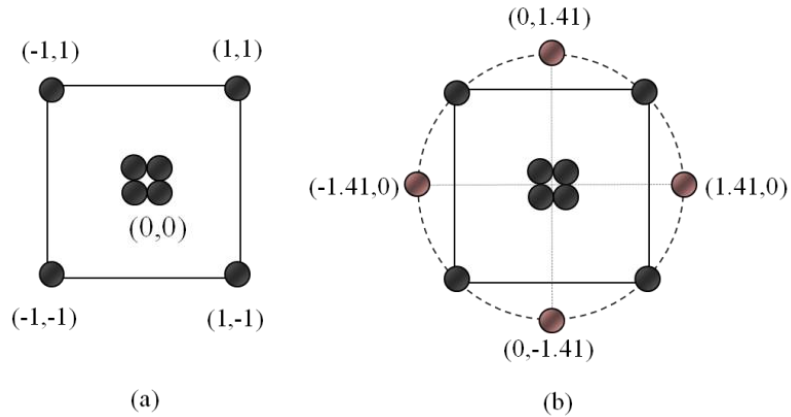


**Figure 20.** (a) Combinations in the  $2^2$  factorial design and (b) CCD design.

After determining which parameters have an influence on the responses (structural and magnetic properties), and considering the contour plots that represent the synthesis parameters showing interpolated values of the responses, the Central Composite Design is used in the next step.

**The Central Composite Design** (a) is balanced (2 levels per factor and two factors), (b) has curvature, (c) is modular, and (d) is economic. The CCD, for short, studies the effect of each factor and interaction between them at the center (curvature) and axial points (Figure 20-b). For the present work axial points are added to the initial design. Finally, statistical characterization of the magnetic and structural properties will be performed to study the effect of the factors against  $\alpha=0.05$ .

### CHAPTER III: PREVIOUS RELATED WORKS

Co-ferrite has been widely studied because of its peculiar properties, such as high saturation magnetization, high coercivity, and large magnetic anisotropy. Co-ferrite nanoparticles have potential applications in the industry and sciences. Research in different areas is trying to control structural, mechanical, electrical, and magnetic properties. This is possible by controlling the synthesis process. Morais *et al* 2001 investigated the effect of stirring variation on the synthesis. It has been found that higher stirring speeds decrease the nanoparticles size. The mechanism of nucleation of the nanoparticles, under intensive stirring, is associated with the ions diffusion during the reaction<sup>52</sup>. Therefore, the higher speed of the stirring promotes the nucleation, however not the crystalline growth. Chinnasamy *et al* 2002, 2003 studied the effect of OH<sup>-</sup> excess on the reaction in the co-precipitation method, varying the NaOH concentration. Through this variation one aims to improve on the nucleation rate and restrict the growth of nanoparticles by aggregation. This mechanics increases the electrostatic repulsion on the surface of the nanoparticles. Furthermore, the coercivity was 2290 Oe for the synthesis at 1.13 mol of NaOH. Also, the effect of reaction temperature was evaluated. As expected, higher reaction temperatures favored the ferrite formation at early reaction times; also the nanoparticles synthesized at lower temperature were smaller in size. Nanoparticles with small diameters exhibit high Ms, suggesting that the increment of solubility of the intermediate phase with a rising temperature may promote the selective dissolution of Co(II) ions and the nonstoichiometry of CoFe<sub>2</sub>O<sub>4</sub>. Also, the coercivity increases for higher reaction temperatures. H<sub>ci</sub> was found to be 560 Oe at 98 °C and 0.73M of NaOH<sup>53,54</sup>. Kumar *et al* 2008 investigated the annealing effect (at temperatures between 375 and 1173K) on structural's properties of Co-ferrite and verified the gradual increase of nanoparticles diameter with the increase in annealing temperature<sup>55</sup>.

Recent research demonstrated that when  $Zn^{2+}$  substitutes  $Co^{2+}$  in Co-ferrite, the nanoparticles may have distorted inverse spinel structure.  $Co_{1-x}Zn_xFe_2O_4$  exhibited improved properties such as excellent chemical stability, magnetostriction and magneto-optical properties<sup>19</sup> (Vaidyanathan *et al* 2008). On the other hand, Arumulruga *et al* 2005 synthesized  $Co_{1-x}Zn_xFe_2O_4$  ( $x = 0.1 - 0.5$ ) nanoparticles by co-precipitation method and obtained nanoparticles of average crystal size less than 12 nm. It was found that with higher content of  $Zn^{2+}$  ions, the average crystal size decreases. This behavior was explained with the increase in  $Zn^{2+}$  ions favoring the formation of nucleation sites and preventing the growth of the nanoparticles. For  $Co_{0.5}Zn_{0.5}Fe_2O_4$  nanoparticles spherical morphology was observed. The lattice parameters did not present a noticeable change due to the similar ionic radii of  $Co^{+2}$  and  $Zn^{2+}$  ions. Magnetic properties such as saturation magnetization (which was between 54emu/g to 39.6emu/g), coercivity, remanence magnetization, and Curie temperature were measured at room temperature in a maximum field of 10 kOe and a strong influence on the  $Zn^{+2}$  content was found. This can be understood with the influence of the cationic stoichiometry and its occupancy of the specific lattice sites. Other influences include dead layers on the surface and the existence of spin canting on the surface of the nanoparticles<sup>3</sup>. Duong *et al.* 2006 synthesized  $Co_{1-x}Zn_xFe_2O_4$  ( $x = 0.0 - 0.4$ ) ferrite nanocrystals by forced hydrolysis. They obtained monodispersed nanoparticles with an average crystallite size of about 3nm. With Mössbauer spectroscopy a superparamagnetic behavior at room temperature was determined. The saturation magnetization at temperatures below 100K for CoZn ferrite with  $x = 0.0, 0.2, 0.4$  was 72.1, 89.7, 99.7emu/g, respectively. The increase of the saturation magnetization with increasing  $Zn^{2+}$  ions substitution ( $x = 0.0 - 0.4$ ) is demonstrated. This fact is explained by the decrease in magnetic moments on the sublattice of tetrahedral A-sites due to  $Zn^{2+}$  ions substitution, resulting in the increase of the total magnetic moment. At room temperature, the

saturation magnetization, coercivity, and Curie temperature all decrease, which is attributed to the spin canting effect in the nanoparticles with higher Zn-content<sup>56</sup>.

Vaidyanathan *et al* 2008 investigated in detail the CoZn ferrite nanoparticle system and also magnetic fluids. They synthesized  $\text{Co}_x\text{Zn}_{1-x}\text{Fe}_2\text{O}_4$  ferrite with  $x$  varying from 0.0 to 1.0 by co-precipitation method in an alkaline medium at 85°C for 1 hour and obtained a spinel structure for all concentrations of Co. The lattice parameter increased with the increase in  $\text{Zn}^{2+}$  ions from 8.384Å to 8.451Å, which is attributed to the large ionic radii of  $\text{Zn}^{2+}$  ions. The average crystallite size decreases from 12.02 nm to 6.92 nm with the  $\text{Zn}^{2+}$  increase. The magnetic properties decrease with the increase of  $\text{Zn}^{2+}$  ions; the maximum value reached by the magnetization was 46.55 emu/g with coercivity of 120 Oe for  $x = 0.1$  Zn-content. Magnetic remanence and coercivity also decrease for high Zn-content. This effect is explained in terms of the influence of the cationic stoichiometry, their occupancy of the specific sites, dead layer formation on the surface, and the existence of spin canting of particle surface spins. FTIR was used to confirm the formations of Fe-O bonds and the presence of the associated water content in the samples<sup>57</sup>.

Singhal *et al* 2010 investigated the effect of Zn-substitution in the Co-ferrite nanoparticles on the magnetic properties. Co-Zn nanoparticles ( $x = 0.0, 0.2, 0.4, 0.8, \text{ and } 1.0$ ) was synthesized by the sol-gel route and the annealing effect in the samples at 400, 600, 800, and 1000 °C for  $\text{Co}_{0.4}\text{Zn}_{0.6}\text{Fe}_2\text{O}_4$  confirms the increase of the average crystalline size with the increase in the annealing temperature. The lattice parameter increases linearly with the Zn-concentration, which is attributed to the larger ionic radius of  $\text{Zn}^{2+}$  (0.88 nm) as compared to  $\text{Co}^{2+}$  (0.84 nm). The saturation magnetization increases from 84.5 emu/g to 91.6emu/g for the samples with Zn-content ranging between  $x = 0.0$  and 0.4. This is attributed to the increase of the total magnetic moment of the samples. With further increase in the Zn-content ( $x = 0.6, 0.8 \text{ and } 1.0$ ) the

saturation magnetization decreased from 54.4 emu/g to 17.7 emu/g. This was attributed to the larger Zn-content reducing the superexchange interaction between the A and B sites, thereby producing an increase in the B-B site interaction, which in turn decreases the saturation magnetization. It was found that the coercivity decreases in conjunction with the increase of the grain size. This trend is explained with the overall domain structure, critical diameter and crystalline anisotropy. Hou *et al* 2010 synthesized  $\text{Co}_{1-x}\text{Zn}_x\text{Fe}_2\text{O}_4$  ( $x = 0.0 - 1.0$ ) ferrite nanospheres by the solvothermal method. There, glycol was used as solvent, anhydrous sodium acetate as an alkaline additive and polyethylene glycol was used as surfactant. It was reported that the lattice parameter decreases with  $\text{Zn}^{2+}$  increase. Scanning electron microscopy of  $\text{Co}_{0.5}\text{Zn}_{0.5}\text{Fe}_2\text{O}_4$  revealed the spherical shape of the nanospheres, whose constituents were 10 - 15nm diameter nanocrystals of the same material. The diameter of the nanospheres was between 100 and 200 nm. This behavior was explained with a growth model, which is called “oriented aggregation”. The authors suggest that when the nanoparticles are not subject to restrictions by a surfactant, they randomly grow in an isotropic fashion and eventually form polycrystalline spheres. The saturation magnetization increases for Zn-content below  $x = 0.5$ . The highest saturation magnetization value was obtained for  $\text{Co}_{0.5}\text{Zn}_{0.5}\text{Fe}_2\text{O}_4$  yielding 64.6emu/g. On the other hand, for  $x > 0.5$ , the saturation magnetization decreases. This behavior is attributed to spin canting in the surface layers due to a decrease in the exchange coupling, which is caused by the lack of oxygen mediating the super exchange interaction between  $\text{Fe}^{3+}$  ions at the surface. It is also attributed to the enhancement of the surface potential barrier due to distortion of the crystal lattice caused by the atoms deviating from the normal position in the surface layers<sup>58</sup>.

Another material studied in great detail is the Mn-Zn ferrite. This inverse ferrite is considered as soft magnetic material with low Curie temperature, a moderate magnetization and low coercivity,

thereby being a promising material for magnetocaloric pump applications. Feng *et al* 2007 synthesized MnZn ferrite nanoparticles by hydrothermal method at 250°C for 12h in alkaline medium. The grain size decreases with the increase of Zn<sup>2+</sup> ions from 50nm (x = 0.0) to 15 nm (x = 1.0). The smaller nanoparticles were observed for the samples without content of Mn<sup>2+</sup> ions. Meanwhile, agglomeration phenomena occurred. The addition of Zn<sup>2+</sup> ions contributes to a decrease in the nanoparticles size, which was explained in terms of the ionic radii of the divalent metals Zn<sup>2+</sup> (0.074 nm) and Mn<sup>2+</sup> (0.093 nm). The lattice parameter decreases when the Zn<sup>2+</sup> ions substituted the Mn<sup>2+</sup> ions in the tetrahedral A sites in the crystalline lattice. Furthermore, the surface energy of the nanoparticles may be increased with the addition of Zn<sup>2+</sup> ion content. In the magnetic properties it was found that the Curie temperature (T<sub>C</sub>) and saturation magnetization (M<sub>s</sub>) depend on Zn<sup>2+</sup> content in the samples. T<sub>C</sub> and M<sub>s</sub> increase with increasing Zn<sup>2+</sup> ion content for x ≤ 0.3, which was explained with a more uniform grain size and the spin ordering change from Y-K to Neel type with Zn<sup>2+</sup> ion content. The energy required for offsetting the antiparallel spin alignment in Neel type is more than that required in Y-K type order. For the values x > 0.3, T<sub>C</sub> decreases and this was explained by the fact that Zn<sup>2+</sup> are non-magnetic ions. Thus, the exchange interaction A-B is weakened with the increase of non-magnetic Zn<sup>2+</sup> ions. Others factors associate with the decrease of the magnetic properties are defects and surface effects due to small particles or variations in the moments on the divalent sites<sup>59</sup>.

Nalbandian *et al* 2008 synthesized MnZn ferrite nanoparticles by hydrothermal process with ammonia as precipitating agent at 180 °C for 2 h. In their XRD patterns they found the presence of the Hematite phase ( $\alpha$ -Fe<sub>2</sub>O<sub>3</sub>), which can be understood by the fact that during the hydrothermal treatment a small part of iron hydroxide may be directly transformed to hematite through dissolution and re-precipitation. There exists a strong dependence between crystallite

size and  $Zn^{2+}$  ions content. The average crystallite size decreases with the increase of  $Zn^{2+}$  ions and it has been interpreted based on the strong chemical affinity of  $Zn^{2+}$  ions to the tetrahedral sites on the spinel lattice. Transmission electron microscopy analysis reveals for MnZn ( $x = 0.8$ ) that compounds of spherical nanoparticles with sizes between 8 and 30 nm are single crystals. As far as the magnetic properties are concerned, the saturation magnetization ( $M_s$ ) and coercivity ( $H_{ci}$ ) decrease with increasing the  $Zn^{2+}$  content.

Up to the present time, it has been established that the magnetic behavior of ferrites is dominated by the antiferromagnetic superexchange interaction between  $Fe^{+3}$  ions. Therefore, introducing trivalent rare earth (RE) cations into the ferrite lattice will also induce  $RE^{3+}-Fe^{3+}$  interactions, which should modify the corresponding magnetic properties. Furthermore, Gd-ferrite is known for its low Curie temperature ( $T_c = 24^\circ C$ ) and high pyromagnetic coefficient ( $\partial M/\partial T$ ). For this reason, Upadhyay et al 1999 synthesized fine MnZn nanoparticles doped with  $Gd^{3+}$  ions by co-precipitation method. These particles were coated with oleic acid and dispersed first in kerosene and later in diester to obtain a ferrofluid. The structural and magnetic properties were studied, finding that the substitution of Gd has an influence on the average crystal size, which decreases from 6.7 to 6.0nm for the samples without and doped with  $Gd^{3+}$  ions, respectively. The magnetization and Curie temperature increase with the substitution of  $Gd^{3+}$  ions, where  $T_c$  varied from  $340^\circ C$  to  $348^\circ C$ . Thus, the pyromagnetic coefficient increased. Brusentsova *et al* 2005 investigated the effect of Gd-substitution on MnZn ferrite with different composition. They synthesized Gd-doped MnZn ferrite nanoparticles by co-precipitation method. The Curie temperature was found to be between  $44^\circ C$  and  $47^\circ C$ .

Ateia *et al* 2006 studied the effect of rare earth (RE) doping on the structural and transport properties of MnZn ferrite. No secondary phases were formed for a concentration of rare earths

(Dy, Gd) below 0.03. This was attributed to the partial incorporation of RE<sup>3+</sup> ions with small ionic radii. For RE > 0.03 secondary phases formed on the grain surface. The lattice parameter was distorted<sup>60</sup>.

Considering the abovementioned results, here we investigate (i) the effect of the synthesis conditions, such as precipitation agent (NaOH) molarity, reaction stirring velocity, and the ratio of the added metal salts, (ii) the effect of the composition (pure CoZn versus Gd & Dy doped CoZn ferrite) on the structural and magnetic properties, and (iii) the effect of synthesis temperature on the structural and magnetic properties, for which the ferrite nanoparticles were grown by the hydrothermal method.

## CHAPTER IV: EXPERIMENTAL DETAILS

### 4.1 Synthesis of CoZn Ferrite Nanoparticles

Control of the size of nanoparticles can improve their magnetic properties for applications in magnetocaloric pumps. Hence, knowing and controlling the synthesis is a crucial step.

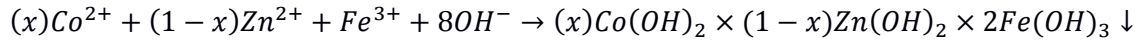
#### 4.1.1. Materials

All precursors were of chemical grade and used without further purification. Required weights of  $\text{FeCl}_3 \cdot 6\text{H}_2\text{O}$  (purity of 97%),  $\text{ZnCl}_2$  (purity  $\leq 98\%$ ),  $\text{CoCl}_2 \cdot 6\text{H}_2\text{O}$  (purity of 98%–102%) salts were dissolved in de-ionized water to achieve the desired ( $\text{Fe}^{3+}/\text{Co}^{2+} + \text{Zn}^{2+}$ ) mole ratio of 2/1 according to  $\text{Co}_x\text{Zn}_{1-x}\text{Fe}_2\text{O}_4$  stoichiometry composition. NaOH purity of 98% was used as the alkaline agent.

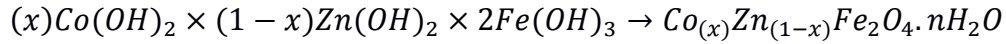
#### 4.1.2. Conventional Co-Precipitation Method

$\text{Co}_x\text{Zn}_{1-x}\text{Fe}_2\text{O}_4$  ferrite nanocrystals were synthesized by the conventional co-precipitation method, with  $x = 0.5, 0.6, 0.7, 0.8, 0.9$  and  $1.0$ . In the conventional route, an aqueous solution of  $0.055 \text{ M}$  ( $\text{Co}^{2+} + \text{Zn}^{2+}$ ) and  $0.11 \text{ M}$  ( $\text{Fe}^{3+}$ ) was mixed with a boiling  $0.48 \text{ M}$  NaOH solution under mechanical stirring at  $500 \text{ rpm}$ . The resulting suspension was kept boiling for  $1 \text{ h}$  of reaction time to allow the complete dehydration and atomic rearrangement involved with the formation of ferrite particles. The nanoferrites are formed by conversion of metal salts into hydroxides (Fe-Co), which take place immediately, in the presence of an excess of  $\text{OH}^-$  (that improve on the nucleation rate and restrict the growth of nanoparticles by aggregation). The solid metal hydroxides were transformed to Co-Zn ferrite by heating in the alkaline medium.

*The first step: Hydroxides of metal cations*



*The ferritization step:*



At the end of the reaction time, the nanoparticles were washed 5 times with de-ionized water using magnetic separation, dried at 60 °C for 24 h, pulverized with an agate mortar and finally submitted for characterization. Figure 21 shows the experimental procedure.

#### **4.1.3. Size-Controlled Co-Precipitation Method**

Co-Zn ferrite nanocrystals with  $x = 0.7, 0.8, 0.9,$  and  $1.0$  were synthesized by size-controlled co-precipitation method. The conventional route was modified by controlling the addition of metal salts into the alkaline medium solution at a predetermined flow rate. For this purpose, a microperistaltic pump with precise control of flow rate was used. The aim of this controlled addition of the metal ions is to promote heterogeneous nucleation. Here, the nucleation and growth processes are separated and hence agglomeration and aggregation avoided during the reaction step. With this synthesis route one tries to control the size of the particles and evaluate the relation between the average crystallite size and its corresponding magnetic properties. This synthesis method has been development in the Nanomaterials laboratory- UPRM.<sup>61-64</sup>

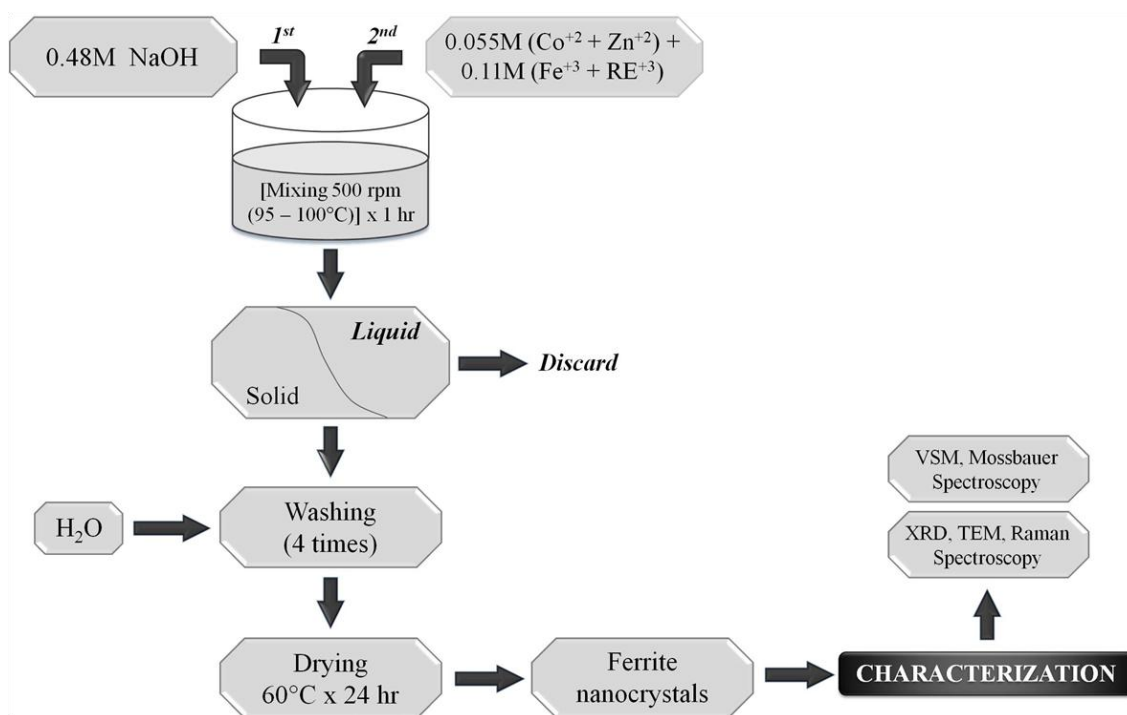


**Figure 21.** Schematic representation of the nanoparticles synthesis by the conventional co-precipitation method. In the size controlled method, the metal salts (identified as 2<sup>nd</sup>) are added at different flow-rates using a peristaltic pump.

#### 4.2 Synthesis of Co<sub>0.7</sub>Zn<sub>0.3</sub>Fe<sub>2</sub>O<sub>4</sub> Nanoparticles by Hydrothermal Method

The hydrothermal technique is advantageous for obtaining nanoparticles with narrow size distribution, as well as for the growth of crystals with polymorphic modification, and growth of crystals with low and ultra low solubilities.

For the present work this process was used in order to study the effect of temperature and pressure in the formation and the magnetic properties of Co<sub>x</sub>Zn<sub>1-x</sub>Fe<sub>2</sub>O<sub>4</sub> (x=0.7) ferrite nanoparticles, synthesized under the same chemical conditions as in the co-precipitation method. Under hydrothermal conditions, it is expected that the solution will be in thermodynamic equilibrium. Consequently, the crystal-size is enhanced and the ion distribution in the ferrite structure should be promoted.

#### 4.2.1. Materials and Procedure

The same metal salts as for the co-precipitation method (section 4.1.2) was used, however, according to the  $\text{Co}_{0.7}\text{Zn}_{0.3}\text{Fe}_2\text{O}_4$  stoichiometry.

$\text{Co}_{0.7}\text{Zn}_{0.3}\text{Fe}_2\text{O}_4$  ferrite nanocrystals were synthesized by hydrothermal method. An aqueous solution of 0.055 M ( $\text{Co}^{2+} + \text{Zn}^{2+}$ ) and 0.11 M ( $\text{Fe}^{3+}$ ) diluted in 106mL of deionized water was contacted with a room temperature 0.48 M NaOH solution diluted in 200 mL of deionized water. The mixed solution was poured into a stainless-steel autoclave under mechanical stirring at 500 rpm at 100, 150 °C and 250 °C for 1h, after reaching the set temperature. At the end of the reaction time, the nanoparticles were washed 5 times with deionized water, using magnetic separation, dried at 60 °C for 24 h, then pulverized with an agate mortar and finally submitted for characterization.

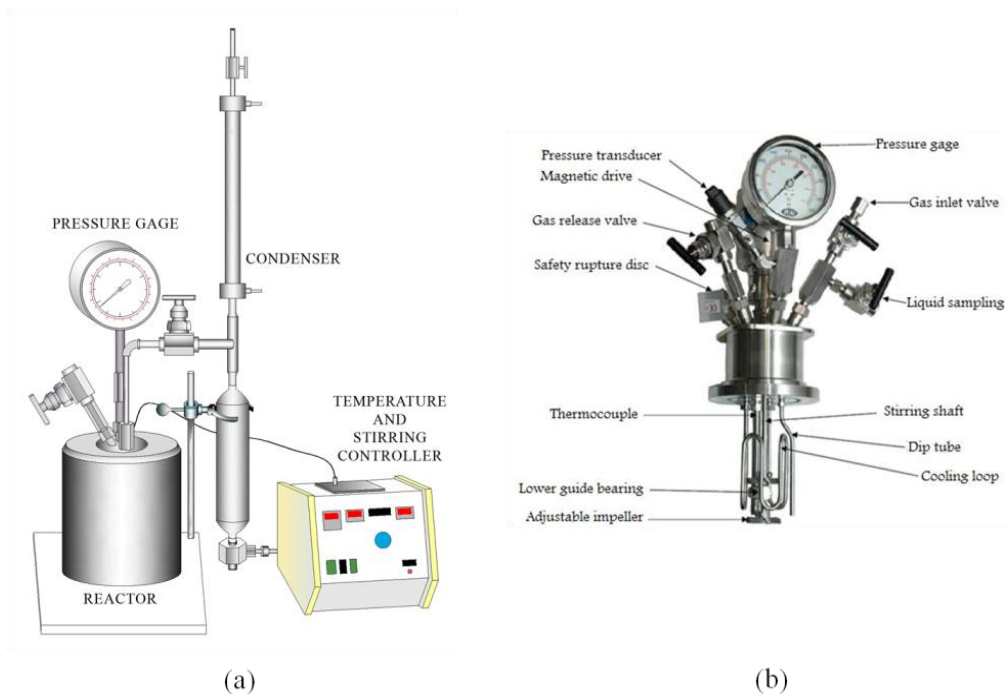


**Figure 22.** (a) Schematic representation of autoclave used, and (b) 475 HP/HT pressure reactor from parr Instruments company

### 4.3 Synthesis of RE doped $\text{Co}_{0.7}\text{Zn}_{0.3}\text{Fe}_2\text{O}_4$ Nanoparticles (RE=Dy or Gd)

It is known that introducing small quantities of trivalent rare earth (RE) cations into the inverse ferrite lattice should modify the corresponding magnetic properties<sup>6</sup>. Here the RE cations Dy and Gd were utilized.  $\text{Dy}^{3+}$  ( $4f^95s^2p^6$ ) and  $\text{Gd}^{3+}$  ( $4f^75s^2p^6$ ) are stable metals with an ionic radius of 0.091 nm and 0.097 nm, respectively and Curie temperatures of 88 K and 292 K, respectively. The compound Gd-ferrite exhibits a Curie temperature of 298 K and has a high pyromagnetic coefficient. These facts could open the possibility to tune M and  $T_d$  in Co-Zn ferrites by controlled incorporation of these rare-earth elements into the host structure.

#### 4.3.1. Materials

In this process  $\text{DyCl}_3 \cdot 6\text{H}_2\text{O}$  (purity of 99.9%) and  $\text{GdCl}_3 \cdot 6\text{H}_2\text{O}$  salts were added to the same metal salts used in the synthesis of  $\text{Co}_{0.7}\text{Zn}_{0.3}\text{Fe}_2\text{O}_4$  ferrite nanoparticles.

#### 4.3.2. Conventional Co-Precipitation Method

$\text{Co}_{0.7}\text{Zn}_{0.3}\text{Fe}_{2-y}\text{RE}_y\text{O}_4$  ferrite nanocrystals with  $y=0.01, 0.03, 0.05$  were synthesized by co-precipitation method. The initial molar ratio of the salts  $(\text{Co}^{2+} + \text{Zn}^{2+}) / (\text{Fe}^{3+} + \text{RE}^{3+})$  was 0.5. The molarity of the precipitating agent (NaOH) was 0.48M. The process is the same as related in section 4.1.1.

#### 4.3.3. Size-Controlled Precipitation Method

$\text{Co}_{0.7}\text{Zn}_{0.3}\text{Fe}_{2-y}\text{RE}_y\text{O}_4$  ferrite nanocrystals with  $y=0.01, 0.03$  were synthesized by size-controlled co-precipitation method as described in section 4.1.3.

## 4.4 Synthesis of Gd doped $\text{Co}_{0.7}\text{Zn}_{0.3}\text{Fe}_2\text{O}_4$ Nanoparticles Using a Statistical Model

### 4.4.1. Materials and Procedure

$\text{Co}_{0.7}\text{Zn}_{0.3}\text{Fe}_{2-y}\text{Gd}_y\text{O}_4$  ferrite nanoparticles were synthesized by conventional co-precipitation method (explained in section 4.1.2). In this case the interaction of NaOH molarity and atomic fraction of Gd<sup>3+</sup> ions was evaluated. NaOH molarity was evaluated between 0.24-0.72 M and Gd-concentration was evaluated in the range 0.01-0.03. A composite central design (CCD) was used as the statistical model. For the CCD  $2^2$  factors were used and the runs were created by the Minitab program.

## 4.5 Characterization of Ferrite Nanocrystals

Structural analyses of the powdered ferrites were carried out in a Siemens D5000 x-ray diffractometer using the Cu-K $\alpha$  radiation. All the scans were recorded in the  $2\theta$  regions of 15-75° at a scan rate of 0.02° per second. The average crystallite size of the samples was calculated from the line width of the [400] and [440] diffraction peaks using Scherrer's equation. The nanometric size and distribution size of the particles was corroborated by a JEOL 2011 transmission electron microscope (TEM). A Raman spectrometer model Renishaw micro-Raman system with a He-Ne laser operating at 785 nm at room temperature was used to study the incorporation of species into the ferrite host lattice. Magnetic measurements on the powdered samples were performed in a LakeShore 7400 Series vibrating sample magnetometer. Magnetization (M-H) measurements were performed at room temperature in fields up to 22 kOe. The corresponding magnetization-temperature (M-T) profiles were obtained at 5 kOe. Mössbauer spectroscopy was used to determine the  $\text{Fe}^{3+}$  ion distribution in the ferrites. The spectra of the samples were recorded in constant

acceleration mode. A  $^{57}\text{Co}$  radioactive source was used and the spectrometer was calibrated using  $\alpha\text{-Fe}$ .

#### 4.5.1. X-Ray Diffractometry (XRD)

XRD is a technique used for determination of crystal phases, lattice parameters, preferential orientation of the crystal, as well as the average crystal size. Given that photons are particles with zero mass and without charge, the interaction with the materials investigated occurs without damaging the sample, making the XRD technique non-destructive. X-rays are electromagnetic waves with wavelength on the order of a few Ångström and hence on the same order as the crystallographic lattice spacing in crystals. When a monochromatic X-ray beam is incident on a crystalline solid, diffraction or constructive interference occurs from atomic lattice planes with interatomic distance  $d_{hkl}$ , when the Bragg law is satisfied, which is given by:

$$2d\sin\theta = n\lambda$$

where  $\lambda=1.54056\text{Å}$  was used,  $d$  is the interplanar distance,  $n$  is an integer indicating the order of diffraction, and  $\theta$  is the Bragg angle.

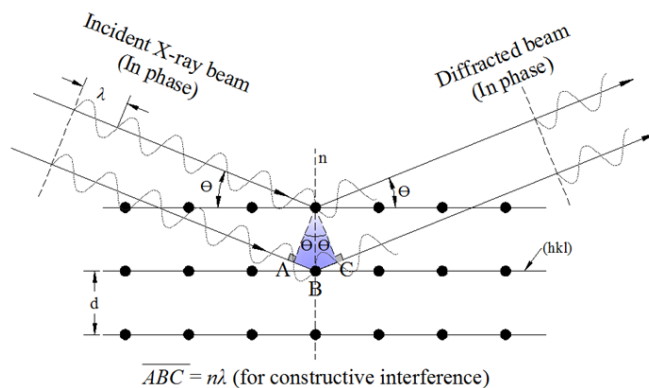


**Figure 23.** Scheme for derivation of the Bragg equation<sup>24</sup>.

In a simple diffraction experiment, the sample is being rotated relative to a fixed incident beam and the angle  $\theta$  is varied until the Bragg equation is satisfied. The diffraction peaks in the resulting spectra are indexed according to the set of planes from which they originate. It is possible to identify each crystallographic plane using Miller indices, which is performed with the FJCPDS file no 22-1086. Once the Miller indices and the corresponding interplanar distances are determined, the lattice parameter of the unit cell can be calculated. For the cubic lattice, the following relation applies<sup>65</sup>:

$$a = d_{hkl} \sqrt{h^2 + k^2 + l^2}$$

In the case of nanoparticles, the diffraction peaks are broadened, with the width being related to the size of the nanoparticles. To quantify this assertion, one considers a powder sample of tiny cubic crystals free of strain and faulting. Hence, from the observed broadening of the peaks for tiny particles it is possible to estimate the average crystal size by the following Scherrer's equation<sup>65,66</sup>

$$D = \frac{0.9\lambda}{\beta \cos\theta}$$

where  $D$  is the particle diameter,  $\theta$  is the diffraction angle, and  $\beta$  is the full width at half maximum (FWHM). The factor  $K$  involves different instrumental aspects, such as geometry, penetration of X-rays into the sample, etc. In this case, the value  $K=0.9$  was used. One has also take into account that broadening of the diffraction peaks occurs due to crystal defects, while if the broadening is larger, the sample might be amorphous.<sup>4</sup>



*Figure 24. Siemens D500 X-Ray Diffractometer.*

#### **4.5.2. Raman Spectroscopy (RS)**

Raman spectroscopy is a technique widely used for the study of structures of materials, which gives information about different modes of vibration of the atoms and molecules in the crystalline lattice. The Raman effect occurs when a photon of energy  $\hbar\omega_E$  interacts with the electronic cloud of a given molecule<sup>67,68</sup>. This interaction produces an excited state of the molecule taking it into a virtual state of higher energy than it was initially. To maintain equilibrium in the system, the molecule liberates energy in the form of a photon.

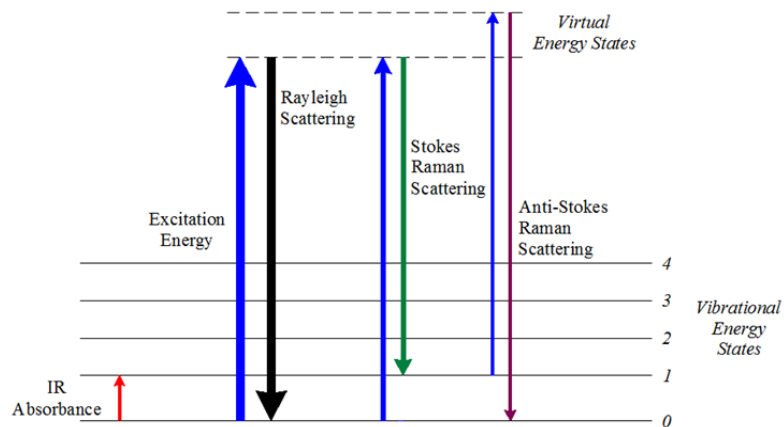


**Figure 25.** Schematic representation of the energy levels showing the state involved in Raman signal.

The photon is inelastically scattered, where Raman Stokes scattering can occur with the molecule changing from its fundamental state ( $\hbar\omega_0$ ) into a virtual state and eventually relaxing with emission of a photon of energy ( $\hbar\omega_E - \hbar\omega_1$ ) and decaying into a state of vibrational excitation. If the molecule was in a vibrationally excited state, Raman anti-Stokes scattering occurs. Rayleigh scattering occurs when the molecule initially was in its ground state and after excitation returns to its ground state again.

#### 4.5.3. High Resolution Transmission Electron Microscopy (HRTEM)

This diffraction technique is used for the analysis of structures of materials and has nanometer size resolution. Furthermore, it has been found that TEM can be used for determination of the melting point of nanocrystals and for measurements of mechanical and electrical properties of nanotubes and nanowires. The operating principle of the TEM is based on the same principle that is used in light microscopes, the difference between them lies in the use of electrons instead of a light source. In TEM the electrons are accelerated to voltages between  $100\text{keV} - 1\text{MeV}$  and are projected onto a sample by electromagnetic

lenses, in order to concentrate the electrons into a thin beam. These electron beams penetrate through the sample and depending on the density will be more or less scattered by elastic and inelastic processes. In elastic scattering there will be no loss of energy giving rise to a diffraction pattern of the sample. The inelastic scattering between the incoming electrons and electrons from sample irregularities gives rise to absorption and dispersion effects that cause variation in the intensities of the transmitted electrons.

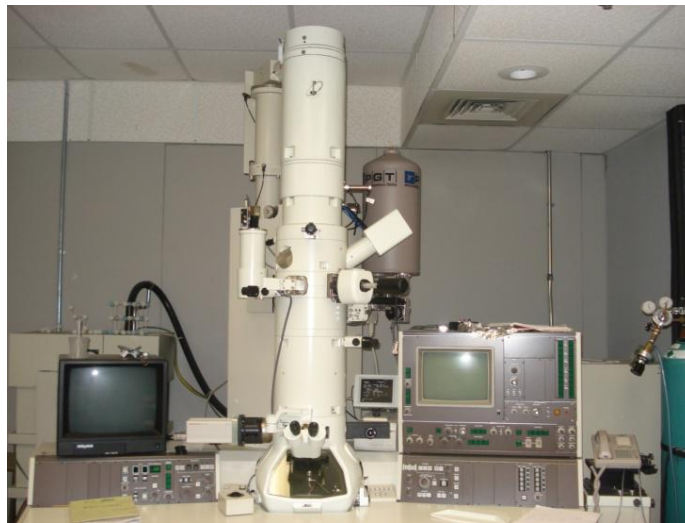


*Figure 26. JEOL 2011 Transmission Electron Microscope.*

One of the main advantages of TEM is its high resolution and magnification, which is possible because of the small wavelength of the accelerated electrons ( $\lambda$  is the de Broglie wavelength). The higher the accelerating voltage the higher the resolution.

A limitation of this technique is that images taken of three-dimensional samples are projected onto two dimensions, while another difficulty is the complexity of sample preparation.

#### 4.5.4. Vibrating Sample Magnetometry (VSM)

This technique permits studying magnetic properties of the materials and measuring hysteresis loops of ferromagnetic and ferrimagnetic materials. The sample is placed in a constant magnetic field and vibrated at right angles to the field at a fixed frequency ( $\cong 80\text{Hz}$ )<sup>26</sup>. The magnetic dipole moment of the sample will create a magnetic field around it, which varies with time due to the vertical motion of the sample. The variation of this magnetic field will be detected by a set of pick-up coils (placed perpendicular to the main magnetic field), inducing an electrical current according to Faraday's law. This induced current is proportional to the magnetization of the sample. The higher the magnetization the greater will be the induced current. The induced current is an AC signal, but is often converted to DC. The AC signal is measured by a lock-in amplifier. Figure 28 shows a schematic of a typical VSM<sup>29</sup>. In order to increase the sensitivity of the signal a second pair of reference pick-up coils is placed with a small permanent magnet in a distant part of the system of vibration. The difference of both signals is then processed.



**Figure 27.** *Lakeshore 7400Series Vibrating Sample Magnetometer.*

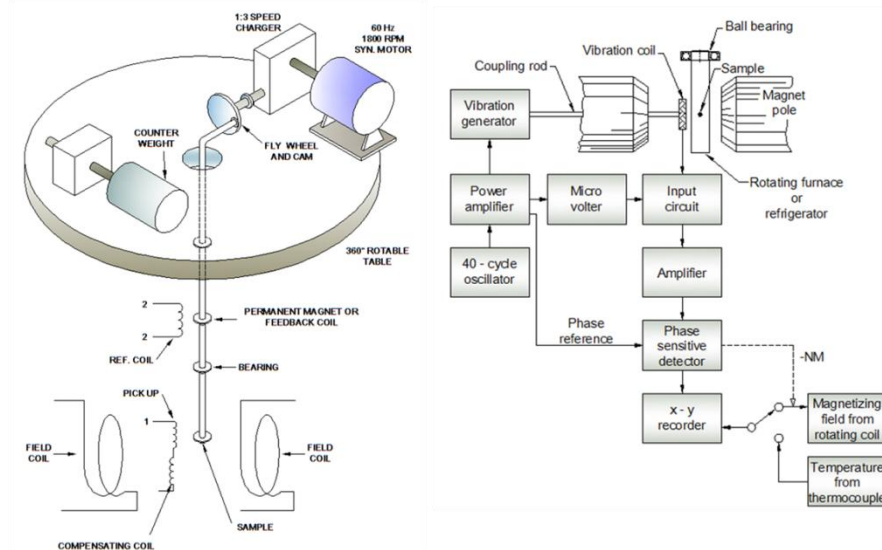


**Figure 28.** Schematic representation of a Vibrating Sample Magnetometer<sup>29</sup>.

#### 4.5.5. Mössbauer Spectroscopy (MS)

The Mössbauer effect utilizes resonant nuclear absorption (without recoil during emission and absorption) of radiation emitted by a nucleus.<sup>23</sup>

Mössbauer spectroscopy is a technique that allows the study of transitions between different energy states of a material, in which electromagnetic radiation is emitted or absorbed by the material.<sup>69</sup> This technique employs recoilless  $\gamma$ -rays emitted by a source consisting of a radioactive isotope. These rays are then absorbed by another identical isotope present in the absorber or a study sample. For the study of the magnetic properties of the material, the source used is the same as the material, such as cobalt. A Co isotope is put in an inert matrix in order to prevent backsliding in both the emission and the absorption. The Co nucleus emitting the radiation is not in a magnetic environment, while the absorbing Co in the study sample is found in a more complex magnetic configuration. The Co nuclear levels in the sample will be influenced by their magnetic environment and can be studied by this

technique. The source must be placed in a cart, which moves at a speed ( $v$ ) with respect to the position of the sample. Thus the gamma ray energy ( $E_\gamma$ ) will experience a shift ( $\epsilon = \frac{v}{c}E_\gamma$ ) due to the Doppler effect. This makes it possible to controllably adjust the frequency of the emission by varying the speed of the source and measure resonance absorption curves of the modulation function of the energy of the gamma rays emitted. Due to the high resolution of Mössbauer spectroscopy it is possible to measure small effects such as hyperfine interactions, which are electromagnetic interactions that occur between the nucleus and its environment (next to the core electrons).

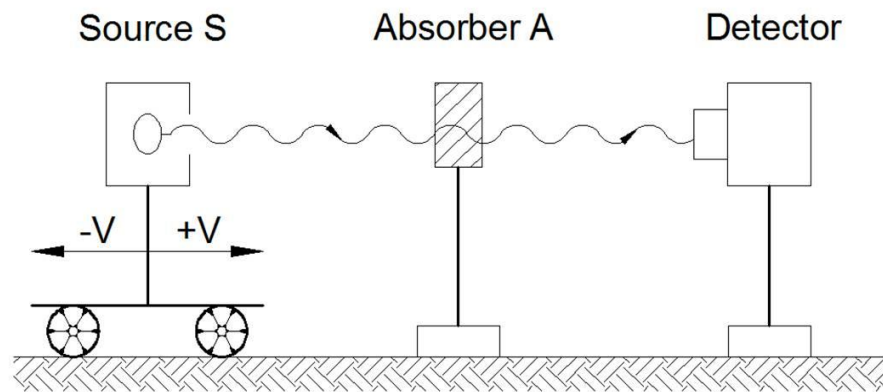


**Figure 29.** Experimental device for Mössbauer spectroscopy.

The three main hyperfine interactions are: (i) Electric monopolar interaction between electric charge and nuclear charge, which gives rise to a Mössbauer spectrum shift called isomer shift ( $\delta$ ); (ii) Magnetic dipole interaction between the magnetic moment of the nucleus and a magnetic field (external or internal). This interaction causes the hyperfine splitting of the spectrum, which depends on the nuclear spin. This phenomenon is known as quadrupole splitting; (iii) Electric quadrupole interaction between the nuclear quadrupole

moment and magnetic field gradient tensor. In this case there is also a splitting of the spectrum. This interaction will cause the Zeeman effect.

***Isomer shift ( $\delta$ ):*** This interaction produces a shift in energy levels of nuclei, produced by the interaction between the nucleus and the electrons close to it. This interaction results in a shift of the excited and fundamental levels and consequently a shift in the resonance energy. This shift will depend on the state of ionization of atoms, giving information about electronic densities of nuclei in different compounds.

***Quadrupole splitting:*** In nuclei with different spin  $1/2$  and  $0$  the spatial charge distribution is not symmetric, so that it generates a quadrupole moment, which by interacting with an electric field gradient, will produce a splitting of the excited energy levels of the nucleus.

***Zeeman Effect:*** In the presence of a magnetic field (which could be produced by the crystal lattice by exchange interactions or by an external field applied), the energy levels are split into sub-levels. This split is proportional to the magnetic field and the quantum number. Depending on the sample, transitions between nuclear states occur with different probabilities.

In the case of magnetic materials, there will always be a magnetic field in the nucleus, called hyperfine field. The hyperfine field originates from the interaction of magnetic moments of electrons with the spin of the nucleus. The intensity of the hyperfine field can be determined from the distance between the lines of the spectra.

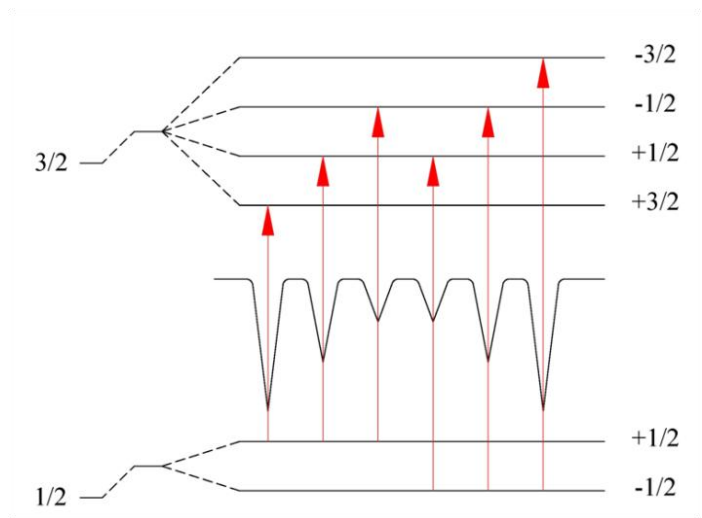


**Figure 30.** Splitting of nuclear levels in  $^{57}\text{Fe}$  by a magnetic field. One can observe the isomeric shift and transitions giving rise to the characteristic sextet of Fe.



**Figure 31.** WEBRES spectrometer operating in the transmission mode, with  $^{57}\text{Co}$  source in a Rh matrix (Ritverc, GmbH).

## CHAPTER V: RESULTS AND DISCUSSION

### 5.1 Tuning of Magnetic Properties in $\text{Co}_x\text{Zn}_{1-x}\text{Fe}_2\text{O}_4$ Ferrite Nanocrystals Synthesized by a Size Controlled and Conventional Co-Precipitation Method

#### 5.1.1. Conventional (i.e., no control on flow-rate) ferrite synthesis

##### 5.1.1.1. Structural Analyses

The ferrite structure for all Co-atomic fractions, 'x', see Figure 32(a), and flow-rates was confirmed by X-ray diffractometry. No secondary or impurity phases were detected. The average crystallite size was calculated using Scherrer's equation in the crystallographic plane 400 and 440. The average crystalline size for the powders synthesized by the conventional co-precipitation route increased from  $(6.50 \pm 0.21)$  nm to  $(13.08 \pm 1.01)$  nm in the 'x' = 0.5-1.0 range as seen in the *Table 3*. Zinc has a high affinity for oxygen and its variable content in the evaluated compositional range should have influenced the solubility of the metal hydroxide precursors and therefore the nucleation rate of generated ferrite crystals.

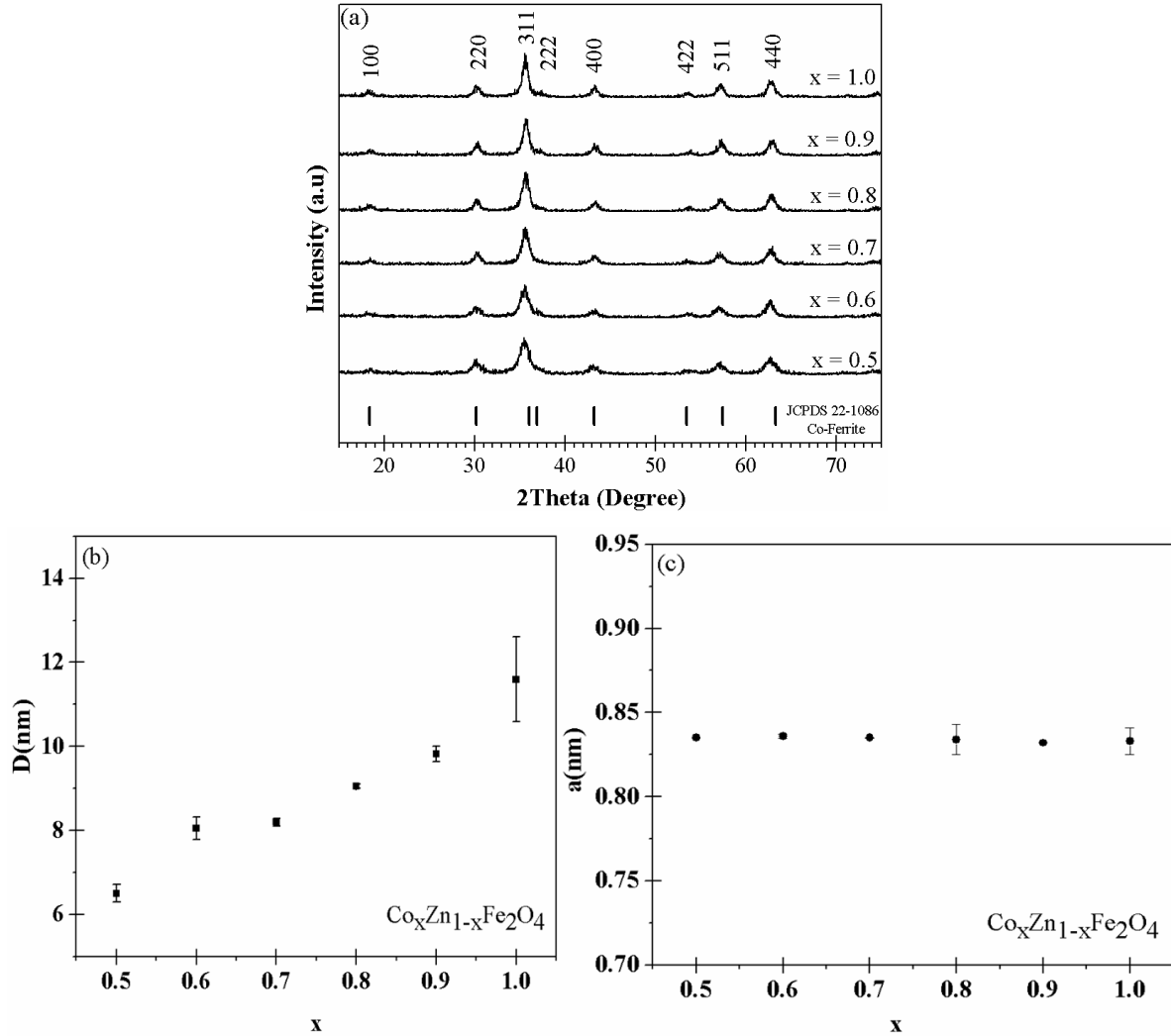


**Figure 32.** (a) XRD patterns for CoZn ferrite powders synthesized by the conventional (i.e., without control of flow-rate) co-precipitation method and at different Co atomic fractions, 'x'; (b) average crystallite size as function of 'x', and (c) variation of ferrite lattice parameter as function 'x' value.

As Figure 32(c) shows, the lattice parameter does not show a remarkable variation when the Co atomic fraction value, 'x', was increased. This parameter varied between  $(0.836 \pm 0.0014)$  nm and  $(0.832 \pm 0.0004)$  nm. These values are very close to the lattice parameter for bulk cobalt ferrite ( $a=0.838$  nm)<sup>70</sup> and zinc ferrite ( $a=0.843$  nm)<sup>70</sup>. Table 3 summarizes the average crystallite size 'D' and lattice parameter 'a'. D400 and D440 represent the average crystallite size for the crystallographic planes 400 and 440, respectively.

**Table 3.** Average crystallite size,  $D$ , and lattice parameter,  $a$ , for  $\text{Co}_x\text{Zn}_{1-x}\text{Fe}_2\text{O}_4$  synthesized at different Co atomic fractions, 'x', by the conventional co-precipitation method.

Co atomic fraction, 'x'	$D_{400} \pm \Delta D_{400}$ (nm)	$D_{440} \pm \Delta D_{440}$ (nm)	$D \pm \Delta D$ (nm)	$a \pm \Delta a$ (nm)
x= 0.5	6.2±0.07	6.8±0.07	6.50±0.21	0.835±0.0003
x= 0.6	7.8±0.06	8.31±0.08	8.05±0.26	0.836±0.0014
x= 0.7	8.1±0.08	8.12±0.07	8.2±0.09	0.835±0.0002
x= 0.8	9.1±0.07	9.0±0.08	9.05±0.05	0.834±0.0009
x= 0.9	10±0.12	9.65±0.08	9.82±0.18	0.832±0.0004
x= 1.0	14.1±0.13	12.07±0.08	13.08±1.01	0.833±0.0008

### **Raman Analyses of $\text{Co}_x\text{Zn}_{1-x}\text{Fe}_2\text{O}_4$ ferrite nanocrystals synthesized by the conventional co-precipitation method**

In the following, Raman scattering results are presented and discussed. All cubic inverse spinels have the  $O_h^7(Fd\bar{3}m)$  space group with 39 normal modes:

$\Gamma = A_{1g} + E_g + T_{1g} + 3T_{2g} + A_{2u} + 4T_{1u} + 2T_{2u}$ , where the following five optic modes are Raman active ( $A_{1g} + E_g + 3T_{2g}$ )<sup>71</sup>. These five active frequencies will depend on the ferrite composition and synthesis method. It has been reported that the mode  $A_{1g}$  appears near to  $650\text{cm}^{-1}$  and is related to the motion of oxygen around the tetrahedral lattice site. The mode  $T_{2g}$  appears close to  $470\text{cm}^{-1}$  and is related to the motion of oxygen around octahedral sites<sup>72</sup>. Figure 33 shows the Raman spectra for the  $\text{Co}_x\text{Zn}_{1-x}\text{Fe}_2\text{O}_4$  ( $x = 0.5, 0.7, \text{ and } 0.9$ ) ferrite synthesized by conventional co-precipitation method. Two vibration modes are clearly visible for all Co atomic fractions, summarized in *Table 4*. The table also contains values for pure Co-ferrite synthesized also by co-precipitation and taken from Yu et al.<sup>71</sup>

**Table 4.** Summary of the Raman shifts for tetrahedral and octahedral sites in Co-Zn ferrite.

$\text{Co}_x\text{Zn}_{1-x}\text{Fe}_2\text{O}_4$	$A_{1g} (\text{cm}^{-1})$	$T_{2g} (\text{cm}^{-1})$	Reference
x=0.5	653	476	This work
x=0.7	625	470	This work
x=0.9	625	477	This work
x=1.0	695	480	T. Yu <i>et al.</i>

The vibrational mode  $A_{1g}$  in the observed spectrum of the Co-Zn ferrite corresponds to  $\text{Fe}^{3+}$  and  $\text{Zn}^{2+}$  ions of the lattice. If the ion masses are taken into account, one would expect that with decreasing Zn-content, the Raman shift for the mode  $A_{1g}$  increases. For  $x = 0.5$ ,  $A_{1g}$  is larger than for  $x = 0.7$  and  $0.9$ , suggesting the presence of the more Co-ions in the tetrahedral sites. Experimentally, it was found that the Co-ferrite structure is not completely inverse, which means that there are  $\text{Co}^{2+}$  ions in the tetrahedral ( $A_{1g}$ ) site as well as in the octahedral ( $T_{2g}$ ) site<sup>73</sup>. For the samples with  $x = 0.7$  and  $0.9$  a superposition of two vibration modes is observed, which manifests itself as a small shoulder next to the main peak. This shoulder is more pronounced in the CoZn ( $x = 0.7$ ) ferrite, suggesting a distortion of the crystalline lattice. The vibrational mode  $T_{2g}$  is generated by the presence of  $\text{Fe}^{3+}$  and  $\text{Co}^{2+}$  ions. The Raman shift obtained for CoZn ( $x = 0.5$ ) ferrite is higher than for CoZn ( $x = 0.7$ ), which is due to the presence of  $\text{Fe}^{3+}$  ions in the octahedral site and decrease of the  $\text{Co}^{2+}$  ions.

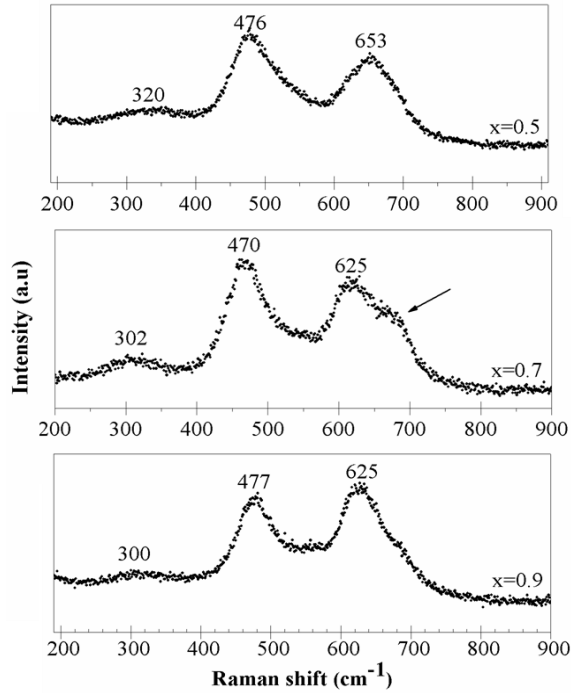


**Figure 33.** Raman spectra for the CoZn ( $x = 0.5, 0.7, 0.9$ ) ferrite synthesized by the co-precipitation method. The arrow in the middle panel ( $x = 0.7$ ) indicates the shoulder appearing as discussed in the text.

In the case of CoZn ( $x = 0.9$ ) ferrite one observes that the Raman shift for the  $T_{2g}$  mode appearing at  $477 \text{ cm}^{-1}$  (Figure 33) is close to the corresponding value for pure Co ferrite, which appears at  $480 \text{ cm}^{-1}$ . This is attributed to the decrease in the lattice distortion and the presence of  $\text{Co}^{2+}$  ions. In summary, the  $\text{Co}_{0.7}\text{Zn}_{0.3}$  ferrite shows a double  $A_{1g}$  peak structure, suggesting an increased presence of defects.

### 5.1.1.2. Magnetic Measurements

In Figure 34 are shown room temperature M-H loops for  $\text{Co}_x\text{Zn}_{1-x}\text{Fe}_2\text{O}_4$  ( $0.5 \leq x \leq 1.0$ ) ferrite synthesized by the conventional method (34a), and trend of the magnetization (M) and coercivity (H) as function of Co atomic fraction (34b). These values are also summarized in Table 5. The maximum magnetization ranged from  $48 \text{ emu/g}$  ( $x=0.5$ ) to  $60 \text{ emu/g}$  ( $x=1.0$ ).

This enhancement in magnetization is attributed to the increase in magnetic  $\text{Co}^{2+}$  ions replacing non-magnetic  $\text{Zn}^{2+}$  ions, thereby affecting the superexchange interaction.<sup>74,75</sup> Furthermore, the coercivity of the samples was also increased by increasing the contents of Co. This trend in coercivity can be attributed to the ferrite composition and the distribution of metal ions in specific lattice sites in the ferrite structure, as well as the fact that  $\text{Co}^{2+}$  changes the crystal field and induces anisotropy in the system. As mentioned above, for this mixed ferrite structure the magnetic ordering is determined by super-exchange interactions between metal ions on the lattice A- and B-sites. The  $\text{Fe}^{3+}$  ions in cobalt-free  $\text{ZnFe}_2\text{O}_4$  occupy the octahedral B-sites and half of the tetrahedral A-sites with the other half of A-sites occupied by  $\text{Zn}^{2+}$  species. However, the divalent  $\text{Co}^{2+}$  and  $\text{Zn}^{2+}$  species in  $\text{Co}_x\text{Zn}_{1-x}\text{Fe}_2\text{O}_4$  structure are expected to occupy the octahedral B-sites whereas only  $\text{Fe}^{3+}$  species would be located in the tetrahedral A-sites.

**Table 5.** Magnetization (*M*) and coercivity (*H*) for the CoZn ferrite at different *x*- values, synthesized by the conventional co-precipitation method.

Sample ( $\text{Co}_x\text{Zn}_{1-x}\text{Fe}_2\text{O}_4$ )	M (emu/g)	H (Oe)
x= 0.5	48	8
x= 0.6	48	8
x= 0.7	63	35
x= 0.8	62	48
x= 0.9	62	150
x= 1.0	60	300

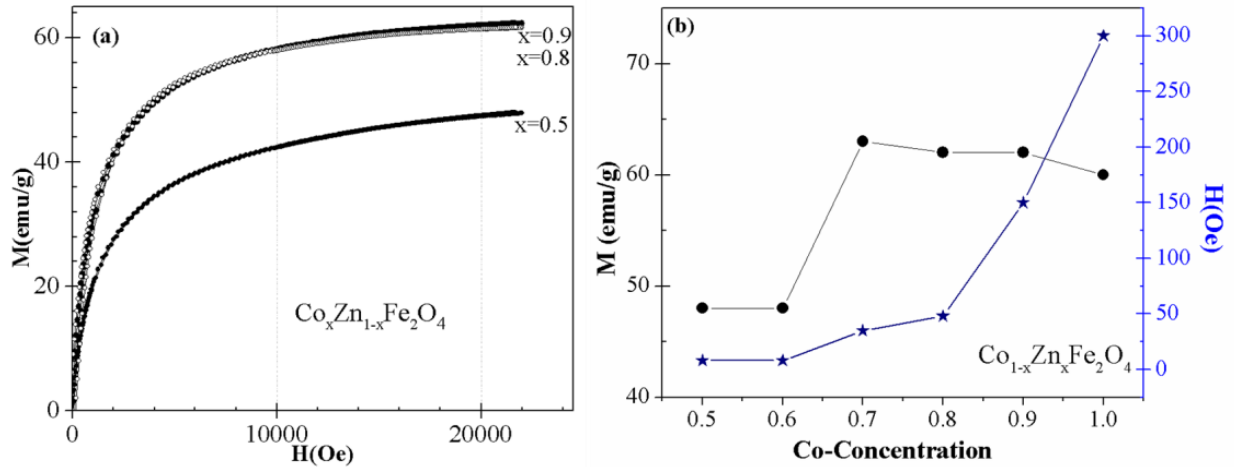


**Figure 34.** (a)  $M$ - $H$  curves for  $\text{CoZn}$  ferrite powders synthesized by the conventional co-precipitation method and different cobalt atomic fraction 'x'; (b) maximum magnetization and coercivity as function of 'x'.

#### M-T measurements for $\text{Co}_x\text{Zn}_{1-x}\text{Fe}_2\text{O}_4$ ferrite

The demagnetization temperature ( $T_d$ ) was determined by extrapolating the linear part of the  $M$ - $T$  curves. The non-linear part in the  $MT$  plot is a consequence of the redistribution at higher temperatures of the  $\text{Zn}^{2+}$ ,  $\text{Co}^{2+}$  and  $\text{Fe}^{3+}$  ions in the tetrahedral A-sites and octahedral B-sites of the ferrite. As Figure 35 and Table 6 evidence,  $T_d$  was increased from  $106^\circ\text{C}$  to  $510^\circ\text{C}$  for powders synthesized in the 0.5-0.9 'x'-range and with no control on flow-rate. This rising trend in  $T_d$  with 'x' could be attributed to the strong superexchange interaction promoted by the larger amounts of magnetic  $\text{Co}^{2+}$  species in the ferrite lattice. A stronger exchange energy coupling between the magnetic moments reinforces the alignment and more thermal energy is needed to destroy this order. This dependence of  $T_d$  with composition of the material has also been observed in  $\text{Mn-Zn}$  and  $\text{Ni-Zn}$  ferrites. This expectation was confirmed for all Co-concentrations in the  $\text{Co}_x\text{Zn}_{1-x}\text{Fe}_2\text{O}_4$  ( $0.5 \leq x \leq 1.0$ ) system and also for  $\text{Mn-Zn}$  ferrites.<sup>76</sup>

**Table 6.** Demagnetization temperature ( $T_d$ ) for the CoZn ( $x=0.5, 0.7, 0.8, 0.9$  and  $1.0$ ) ferrite synthesized by the conventional co-precipitation method.

$(\text{Co}_x\text{Zn}_{1-x}\text{Fe}_2\text{O}_4)$	$T(^{\circ}\text{C})$
$x= 0.5$	106
$x= 0.7$	350
$x= 0.8$	364
$x= 0.9$	510
$x= 1.0$	590

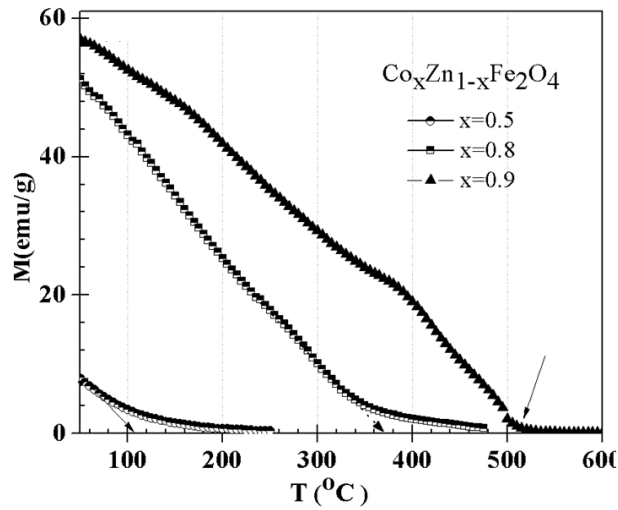


**Figure 35.**  $M$ - $T$  profiles for CoZn ferrites,  $x= 0.5, 0.8,$  and  $0.9$  synthesized by the conventional coprecipitation method. The arrows indicate the demagnetization temperatures. The external magnetic field was 5 kOe.

The pyromagnetic coefficient ( $K_T$ ) was calculated, from the slope of the linear portion in  $MT$  plots. The  $K_T$  values did not change with the synthesis method and ranged between  $0.19\text{emu/g-K}$  and  $0.17\text{ emu/g-K}$  when ‘ $x$ ’ varied from 0.5 to 0.9, respectively. This values were not significant, since that for the Co-Zn and Mn-Zn ferrite this values is around  $0.3\text{ emu/g-K}^{77,78}$ .

### 5.1.1.3. Mössbauer Spectroscopy Analyses

The Mössbauer spectra of Figure 36 clearly show that the increase in Co atomic fraction favors the magnetic ordering in the ferrite structure; doublet peaks, typical of superparamagnetic behavior, were observed for the powders synthesized at 'x'= 0.5 whose average particle size are less than 10 nm, whereas well-defined hyperfine splitting became evident for 'x' 0.8 and 0.9. The spectrum for these samples, synthesized with no control of flow-rate (N-F) yields an internal magnetic field shown in the *Table 7*.

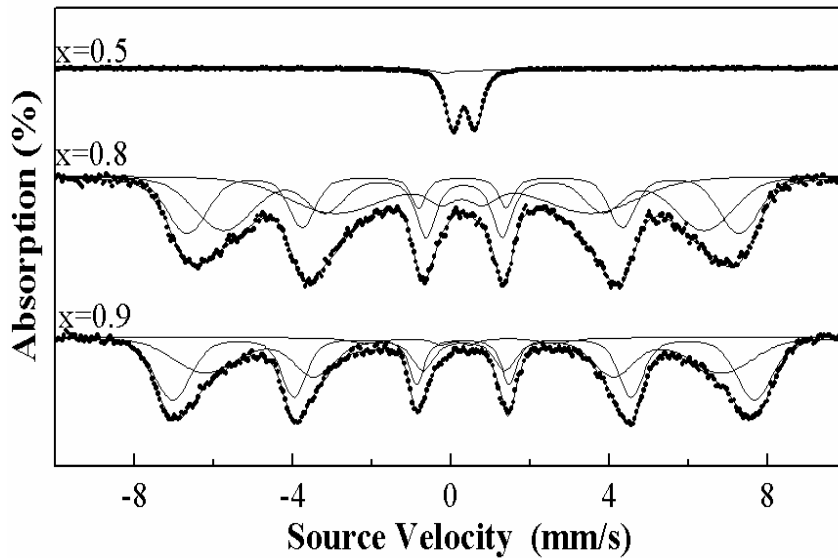


**Figure 36.** Room-temperature Mössbauer spectra for CoZn ferrites, 'x'= 0.5, 0.8, and 0.9, synthesized by the conventional co-precipitation method.

**Table 7.** Mössbauer parameters for the CoZn ( $x=0.5, 0.8, \text{ and } 0.9$ ) ferrite nanocrystals synthesized by the conventional co-precipitation method.

<b>x=0.5</b>	<b>H<sub>f</sub> (kOe)</b>	<b>RA %</b>	<b>IS (mm/s)</b>	<b>QQ (mm/s)</b>	<b>FWHM (mm/s)</b>	<b>h<sub>1</sub>/h<sub>3</sub></b>	<b>h<sub>2</sub>/h<sub>3</sub></b>
Site-1	-	8.61	0.133	0.615	0.285	-	-
Site-2	-	91.39	0.023	-0.629	0.259	-	-
Site-3	-	-	-	-	-	-	-
Site-4	-	-	-	-	-	-	-
<b>x=0.8</b>	<b>H<sub>f</sub> (kOe)</b>	<b>RA %</b>	<b>IS (mm/s)</b>	<b>QQ (mm/s)</b>	<b>FWHM (mm/s)</b>	<b>h<sub>1</sub>/h<sub>3</sub></b>	<b>h<sub>2</sub>/h<sub>3</sub></b>
Site-1	431.45	29.80	0.298	2.240e-2	0.380	3.982	2.523
Site-2	375.44	41.30	0.329	-6.64e-3	0.500	0.966	2.141
Site-3	202.27	28.90	0.288	2.718e-2	0.770	4.000	0.135
Site-4	-	-	-	-	-	-	-
<b>x=0.9</b>	<b>H<sub>f</sub> (kOe)</b>	<b>RA %</b>	<b>IS (mm/s)</b>	<b>QQ (mm/s)</b>	<b>FWHM (mm/s)</b>	<b>h<sub>1</sub>/h<sub>3</sub></b>	<b>h<sub>2</sub>/h<sub>3</sub></b>
Site-1	454.67	48.72	0.308	2.086e-2	0.403	2.630	1.833
Site-2	403.66	47.42	0.321	-1.06e-2	0.550	2.548	1.940
Site-3	147.15	3.86	0.174	0.122	0.491	1.392	0.000
Site-4	-	-	-	-	-	-	-

The fitting of the Mössbauer spectra was carried out by using the hyperfine field distribution model. This model considers four sites in the magnetic structure of the ferrite. The site-1 corresponds to the octahedral position, the site-2 corresponds to the tetrahedral position, and the site-3 and 4 is attributed to the surface. H<sub>f</sub> corresponds to the internal magnetic field and is associated to the hyperfine splitting of the nuclear levels. RA% is the relative abundance percentage of the Fe-ions for each site in the magnetic structure of the ferrite. IS represents the isomer shift which is related to the s-electron density in chemical bonds. QQ represents the quadrupole splitting. The 3/2 state in Fe is degenerate with respect to an asymmetric electrostatic field, and in such a field these levels will be split into  $\pm 3/2$  and  $\pm 1/2$  levels. One can observe transitions either to or from these two levels to the

ground state, which constitutes the quadrupole splitting. FWHM is the full width at half maximum peak-height and corresponds to nuclear transitions. Finally,  $h_1/h_3$  and  $h_2/h_3$  are the ratios between peaks from the hyperfine splitting.

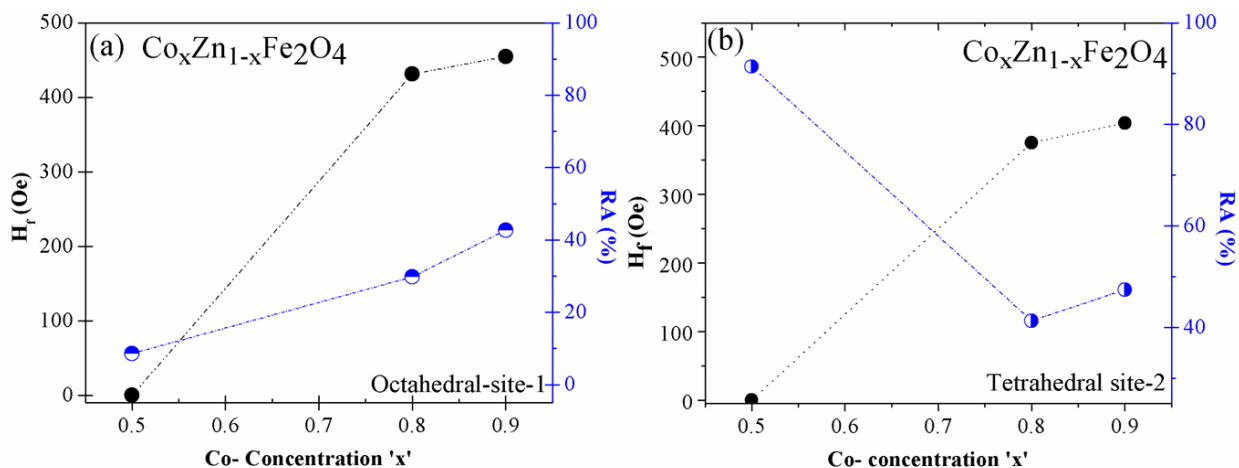


**Figure 37.** Mössbauer parameters  $H_f$  (Oe) and (RA%) as function of cobalt concentration 'x' for octahedral, (a), and tetrahedral, (b), sites.

The information provided by Figure 37 evidences that with an increment of the  $\text{Co}^{2+}$  ions in the ferrite structure, migration of the  $\text{Fe}^{3+}$  ions from the tetrahedral site to the octahedral site was promoted. The migration of Fe-ions from the tetrahedral (A-site) to the octahedral site (B-site) and the decrease in the amount of the  $\text{Zn}^{2+}$  ions caused a drop in the average electron density of the  $\text{Fe}^{3+}$  ions that remain in the tetrahedral site and also increased the corresponding isomer shift (IS). For the B-site, the isomer shift increased with the increment of  $\text{Co}^{2+}$  ions in the B-site and with the fact that greater quantities of oxygen ions are bonded in the B-site than the A-site ( $\text{Fe}_2\text{O}_4$  (A) and  $\text{Fe}_2\text{O}_6$  (B)).

The low values of the quadrupole splitting of the tetrahedral (A) and octahedral (B) sites for the samples with  $x=0.8$  and  $0.9$  would suggest that the local symmetry of the A-site is close

to cubic while that of the B-site is close to trigonal. For the sample with  $x=0.5$ , the quadrupole doublet splitting were very similar ( $QQ=0.615$ -A and  $0.619$ -B).

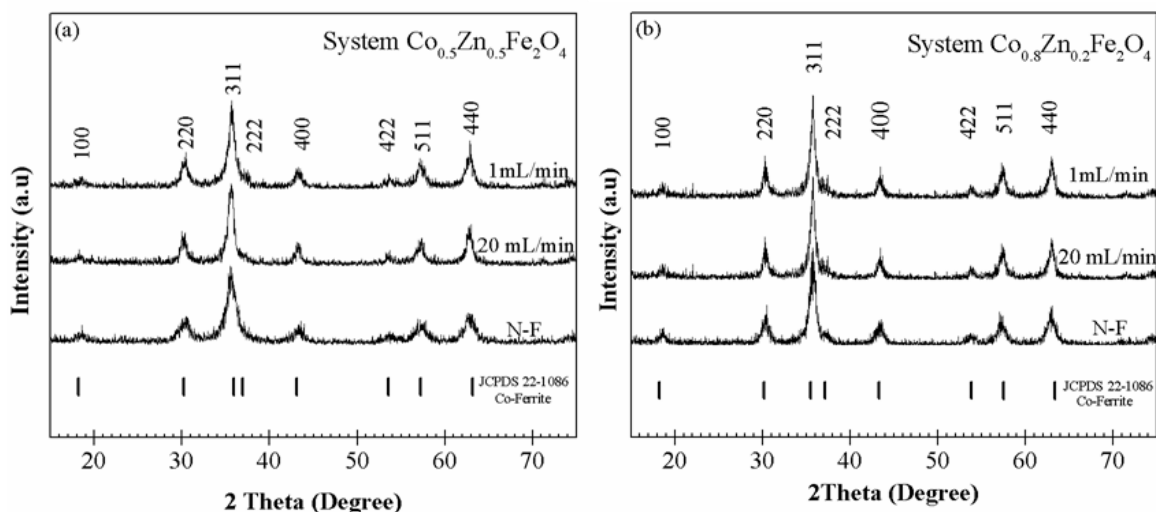
The magnetic hyperfield field,  $H_f$ , arises from three different components: The polarization of  $s$ -electrons by the magnetic moments of the  $d$ -electrons, the dipolar fields of the surrounding magnetic ions and their distribution in A- and B-sites, and from the magnetic moments of the nearest neighboring cations<sup>79</sup>. Figure 37 shows that the magnetic hyperfine field of the tetrahedral site was greater than that of the octahedral site, and both increased with 'x'. This fact can be explained on the basis of the covalent character of the bond  $Fe^{3+} - O^{2-}$  and differences in its length at tetrahedral-A and octahedral-B sites. The bond  $Fe^{3+} - O^{2-}$  is more covalent at the A-site than at the B-site, because the  $s$ -electron charge density at the A-site ( $Fe^{3+}$ ) is larger<sup>79</sup>; this results in a higher internal magnetic field  $H_B$  than  $H_A$ . The increment of the hyperfine magnetic field with the increase in  $Co^{2+}$ -ions was expected since  $Co^{2+}$  has a magnetic moment ( $3 \mu_B$ ) while  $Zn^{2+}$  is non magnetic ( $0 \mu_B$ ). Hence, an increment in the interaction Fe-O-Co is manifested in the increment in the  $H_f$  in the A-site and B-site.

## 5.1.2. Size-controlled synthesis

### 5.1.2.1. Structural Analyses

The influence of flow-rate control on the crystal growth was investigated for  $x = 0.5, 0.8$  and  $0.9$ . Figure 38 shows the X-ray diffraction patterns for CoZn ( $x=0.5$ ) samples synthesized at  $1 \text{ mL/min}$ ,  $20 \text{ mL/min}$ , and with no control on the flow-rate (N-F), while Figure 38 shows the corresponding results for CoZn ( $x=0.8$ ). The average crystallite size for  $x=0.5$  increased from  $(6.50 \pm 0.21) \text{ nm}$  (N-F) up to  $(10.77 \pm 0.08) \text{ nm}$  for  $1 \text{ mL/min}$  and for  $x=0.8$ , the corresponding average crystallite size was increased from  $(9.05 \pm 0.05) \text{ nm}$  (N-F) up to  $(13.44 \pm 0.29) \text{ nm}$  when  $1 \text{ mL/min}$  was selected (included in Figure 39(c)). Furthermore,

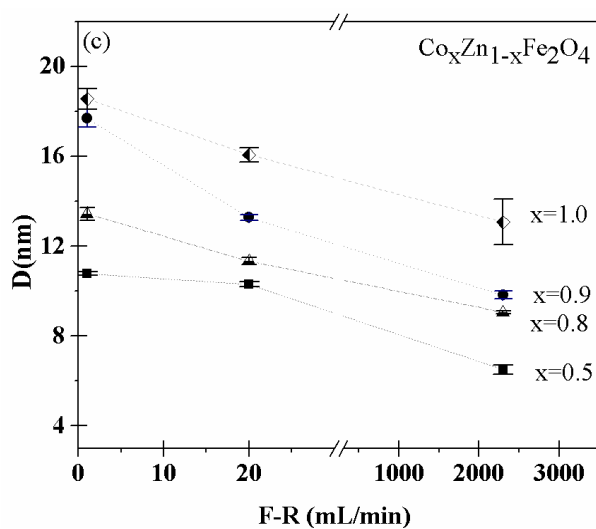
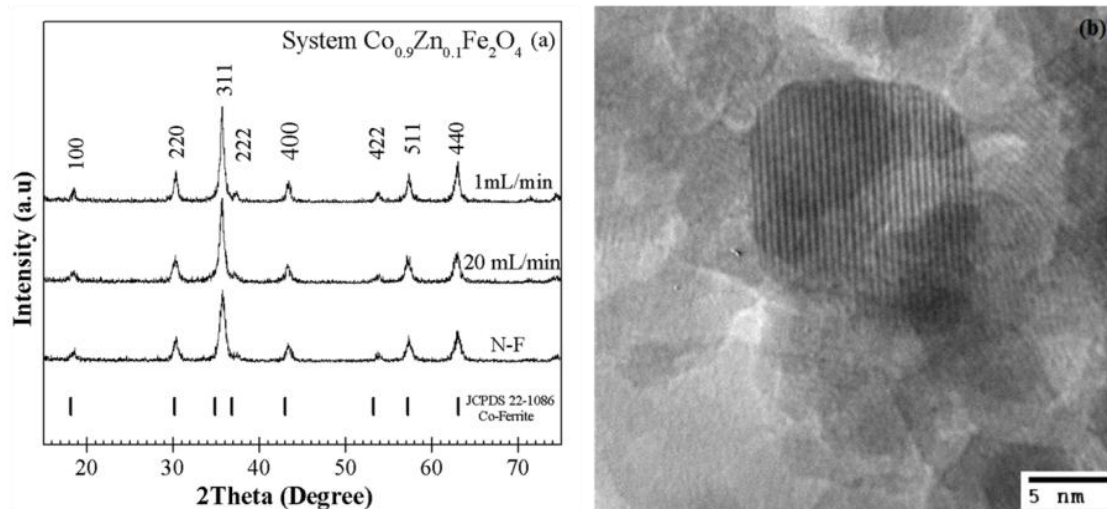
Figure 39(a) shows the X-ray diffraction patterns for CoZn ( $x=0.9$ ) samples synthesized at 1 mL/min, 20 mL/min, and with no control on the flow-rate (N-F). The corresponding average crystallite size is shown in Figure 39(c) and was increased from  $(9.82\pm 0.18)$  nm (N-F) up to  $(17.69\pm 0.39)$  nm when 1 mL/min was selected. The promotion of heterogeneous nucleation, where early generated ferrite nuclei would act as pre-existent seeds, by the controlled addition of the reactants can explain the enlargement of the crystal size. Other secondary processes conducive to grain coarsening, such as Ostwald ripening<sup>42</sup>, could have also been favored. The promotion of crystal growth with low flow-rates has also been verified in pure Cobalt ferrite<sup>63</sup>. Figure 39(b) shows the TEM image corresponding to  $\text{Co}_x\text{Zn}_{1-x}\text{Fe}_2\text{O}_4$  ( $x=0.9$ ) ferrite synthesized at 1 mL/min. The image evidenced the nanometric size of the particles although they are still agglomerated. Moreover, lattice fringes are clearly visible evidencing the good crystallinity of the particles even at the nanoscale.



**Figure 38.** (a) XRD patterns for CoZn ferrite ( $x=0.5$ ), (b) ( $x=0.8$ ) powders synthesized with and without (N-F) control of flow-rate.

**Table 8.** Average crystallite size,  $D$ , lattice parameter,  $a$ , for  $\text{Co}_x\text{Zn}_{1-x}\text{Fe}_2\text{O}_4$  synthesized at different Co atomic fractions, ( $x=0.5, 0.8, 0.9, 1.0$ ) by size-controlled synthesis method.

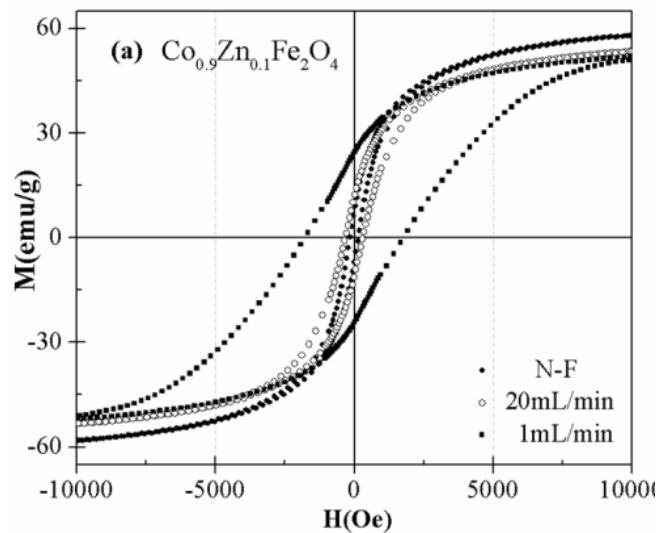
Sample (CoZn)		$D_{400} \pm \Delta D_{400}$ (nm)	$D_{440} \pm \Delta D_{440}$ (nm)	$D \pm \Delta D$ (nm)	$a \pm \Delta a$ (nm)
x=0.5	N-F	6.2±0.07	6.8±0.07	6.50±0.21	0.835±0.0003
	20mL/min	10.4±0.18	10.20±0.10	10.3±0.1	0.838±0.0002
	1mL/min	10.69±0.23	10.85±0.10	10.77±0.08	0.836±0.0008
x=0.8	N-F	9.1±0.07	9.0±0.08	9.05±0.05	0.834±0.0009
	20mL/min	11.49±0.18	11.17±0.08	11.33±0.16	0.834±0.0014
	1mL/min	13.73±0.18	13.15±0.10	13.44±0.29	0.834±0.0014
x=0.9	N-F	10.0±0.12	9.65±0.08	9.82±0.18	0.832±0.0004
	20mL/min	13.4±0.18	13.13±0.1	13.27±0.13	0.836±0.0002
	1mL/min	18.10±0.2	17.27±0.13	17.69±0.39	0.834±0.0003
x=1.0	N-F	14.10±0.13	12.07±0.08	13.08±1.01	0.833±0.0008
	20mL/min	16.21 ±0.15	15.93±0.1	16.07±0.32	0.834±0.0003
	1mL/min	18.10 ±0.23	19.02±0.24	18.56±0.46	0.837±0.0002



**Figure 39.** (a) XRD patterns for CoZn ferrite ( $x=0.9$ ) powders synthesized with and without, (N-F), control of flow-rate. (b) TEM image for CoZn nanocrystals synthesized at  $x=0.9$  and 1 mL/min, and (c) average crystallite size as function of flow rate for different Co fraction values.

### 5.1.2.2. Magnetic Measurements

The complete M-H loops shown in Figure 40(a) evidenced the drop in magnetization when the powders ( $x=0.9$ ) were synthesized under flow-rate controlled conditions; the maximum magnetization decreased from 62emu/g (N-F) to 48emu/g (1mL/min). The promotion of random spin canting on the crystals surface, favored by competing ferrimagnetic exchange interaction and the further development of a magnetic dead layer<sup>24,80-82</sup>, could be involved with the observed trend in magnetization. The coercivity was increased from 150Oe up to 1775Oe, ( $x=0.9$ ), when the flow-rate was as low as 1mL/min. This rise in coercivity at such a low flow-rate was also observed for the powders synthesized at  $x=0.8$  (from 48Oe to 716Oe) and  $x=1.0$  (from 300Oe to 2752Oe), see Figure 39(c). The enhancement of coercivity is attributed to the enlargement of the crystal size, as suggested by our XRD measurements within the single magnetic domain range. *Table 7* summarizes magnetization and coercivity results.



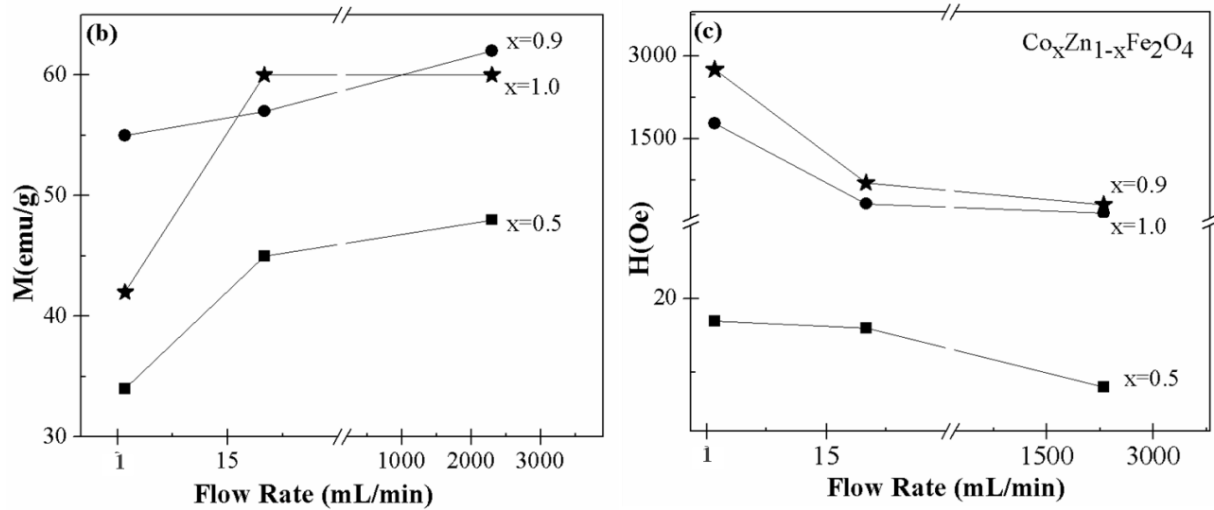


**Figure 40.** (a) Complete hysteresis loop for CoZn ferrite ( $x = 0.9$ ) powders synthesized with and without, (N-F), control of flow-rate; (b) maximum magnetization as function of flow rate for different cobalt atomic fractions, 'x', and (c) coercivity as function of flow rate for different cobalt atomic fractions, 'x'.

If the size of the particle falls below the thickness of a domain wall, no domains can exist. On the other hand, the magnetic energy of the particle decreases with the volume, while the wall energy decreases with the area<sup>27</sup>. Below a certain particle diameter, the decrease in the magnetostatic energy implies an increase in exchange energy and an increase in anisotropy energy inside the domain wall. The coercivity is related to the anisotropy, therefore, when the anisotropy increases, the coercivity increases as well.

**Table 9.** Maximum magnetization (*M*) and coercivity (*H*) for the CoZn (*x*=0.5,0.8,0.9 and 1.0) ferrite synthesized by co-precipitation method with different flow rates.

Sample (CoZn)		M (emu/g)	H(Oe)
x=0.5	N-F	48	8
	20mL/min	45	16
	1mL/min	34	17
x=0.8	N-F	62	48
	20mL/min	55	293
	1mL/min	48	716
x=0.9	N-F	62	150
	20mL/min	57	316
	1mL/min	55	1775
x=1.0	N-F	60	300
	20mL/min	61	697
	1mL/min	42	2752

#### M-T measurements for Co<sub>x</sub>Zn<sub>1-x</sub>Fe<sub>2</sub>O<sub>4</sub> ferrite

Figure 41 shows the increase in  $T_d$  from 105°C to 170°C when CoZn (*x*=0.5) ferrite was synthesized with no control on flow-rate and at 1 mL/min, respectively. As known, the coercivity is related to the strength of the magnetocrystalline anisotropy, which is the energy necessary to overcome the spin-orbit coupling and rotate the spins away from the easy direction<sup>27</sup> and vanishes at  $T_d$ . Accordingly, the larger the coercivity, the higher the demagnetization temperature.

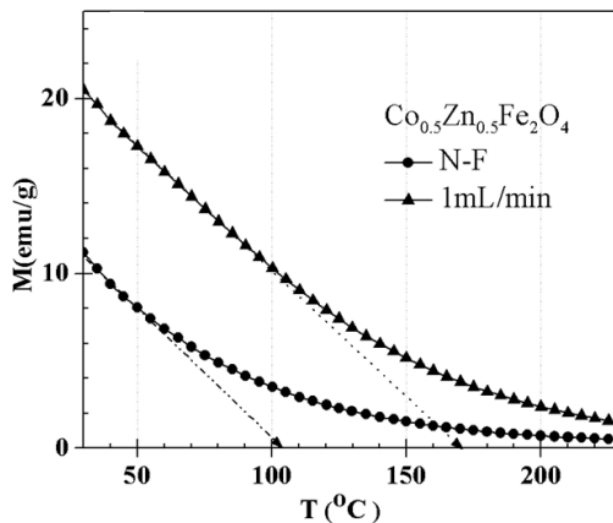


**Figure 41.** *M-T curves for CoZn ferrite powders,  $x=0.5$ , synthesized with no control of flow-rate (N-F) and 1 mL/min. The arrows indicate the demagnetization temperatures. The external magnetic field was 5 kOe.*

### 5.1.2.3. Mössbauer Spectroscopy Analyses

In the Figure 42(a), superparamagnetic behavior at room temperature is seen for all samples, as revealed by the lack of magnetically split peaks. These were therefore fitted with two sub-sites or Fe-environments. The *Table 10* shows the Mössbauer parameters determined from the fittings. Furthermore, magnetically ordered peaks were observed for ‘ $x$ ’= 0.9 independent of the synthesis route, i.e. with and with no control on flow-rate as seen in Figure 42(b). These spectra were resolved with multiple sites comprising of octahedral-Fe, tetrahedral-Fe, and distribution of Fe-sites within the octahedral sites. The presence of asymmetric peaks can be attributed to a lack of random distribution of Fe-cations within the octahedral sites. The magnetic fields were 450.1kOe and 470.8kOe, respectively, for those samples synthesized at 20 mL/min and 1 mL/min. The internal magnetic fields corresponding to the tetrahedral sites were 403.7kOe, 401.8kOe, and 442.2kOe. In addition,

the distribution of Fe within octahedral sites attributed to surface Fe-cations, reported internal fields that ranged from 310kOe to 101kOe, which accounted for about 13%, 4% and 25% of the total spectrum for the samples synthesized with no control on flow-rate (N-F), 20mL/min and 1mL/min, respectively. The corresponding tetrahedral site population was within 54.6% and 47.4% for the samples synthesized at 1 mL/min and 20 mL/min, whereas the isomer shifts for the various sites were all within 0.30mm/s. The results of Mössbauer analyses suggest that the variations in the magnetic behavior of nanosize CoZn ferrites can be attributed to morphological changes associated with the crystal growth process promoted by the low flow-rates. The cationic distribution in the ferrite structure could be affected by the competition of kinetic and thermodynamic factors related to these nucleation and crystal growth events.

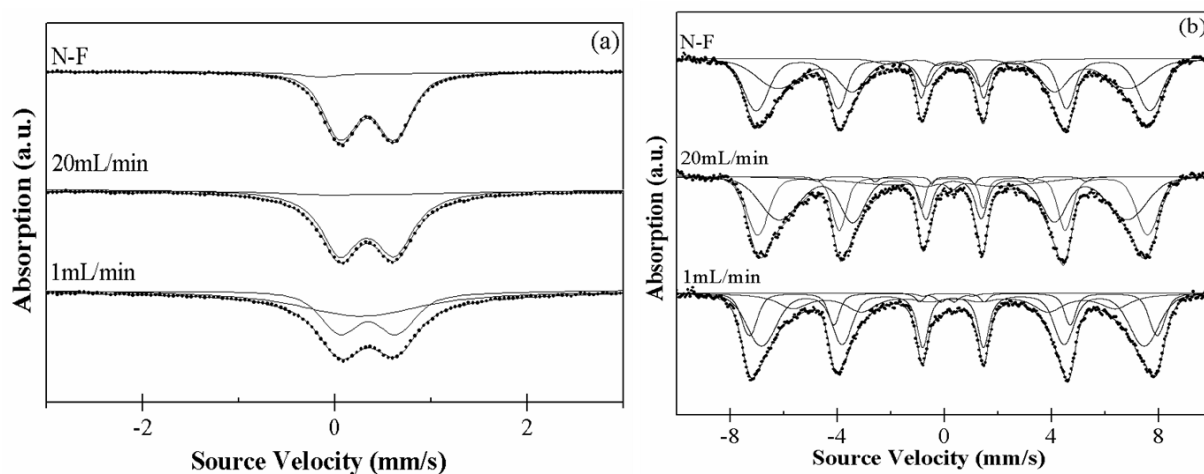


**Figure 42.** Room-temperature Mössbauer spectra for CoZn synthesized at different flow rate conditions for  $x = 0.5$ , (a) and  $x = 0.9$ , (b).

**Table 10.** Mössbauer parameters for the CoZn ( $x=0.9$ ) ferrite nanocrystals synthesized by conventional co-precipitation (N-F) and size-controlled method at 20mL/min and 1mL/min.

N-F	H <sub>f</sub> (kOe)	RA %	IS (mm/s)	QQ (mm/s)	FWHM (mm/s)	h <sub>1</sub> /h <sub>3</sub>	h <sub>2</sub> /h <sub>3</sub>
Site-1	454.67	48.72	0.308	2.086e-2	0.403	2.630	1.833
Site-2	403.66	47.42	0.321	-1.06e-2	0.550	2.548	1.940
Site-3	147.15	3.86	0.174	0.122	0.491	1.392	0.000
Site-4	-	-	-	-	-	-	-
20 mL/min	H <sub>f</sub> (kOe)	RA %	IS (mm/s)	QQ (mm/s)	FWHM (mm/s)	h <sub>1</sub> /h <sub>3</sub>	h <sub>2</sub> /h <sub>3</sub>
Site-1	450.11	36.84	0.298	1.596e-2	0.308	4.000	2.623
Site-2	401.75	50.56	0.298	6.745e-2	0.414	2.66	1.896
Site-3	177.43	10.59	0.298	0.580	0.200F	4.000	2.03
Site-4	310.02	2.01	0.298	-5.16e-2	0.200F	0.873	0.824
1mL/min	H <sub>f</sub> (kOe)	RA %	IS (mm/s)	QQ (mm/s)	FWHM (mm/s)	h <sub>1</sub> /h <sub>3</sub>	h <sub>2</sub> /h <sub>3</sub>
Site-1	470.84	19.47	0.303	5.63e-2	0.319	8.000	4.627
Site-2	442.18	54.63	0.316	-9.52e-3	0.446	2.040	1.416
Site-3	101.43	2.00	0.251	0.271	0.416	0.000	0.277
Site-4	372.50	23.90	0.369	-2.28e-2	1.351	2.270	2.742

The data in Figure 43 shows that the low flow rates favor the migration of Fe<sup>3+</sup> from octahedral B-sites to tetrahedral A-sites as well as towards the surface. In turn, the magnetic hyperfine field, H<sub>f</sub>, increases both in the A-site and the B-site. An increment of the magnetic hyperfine field in the B-site should decrease the magnetic hyperfine field in the A site, however, this does not occur. This behavior can be explained by the polarization of s-electrons by the magnetic moments of the d-electrons and the dipolar field of the surrounding magnetic ions and their distribution in tetrahedral and octahedral sites.

The increase of H<sub>f</sub> in the B-site can be explained by the Sawatzky et al model<sup>83</sup>, which considers the ionic distribution of the first magnetic neighbors of the Fe<sup>3+</sup> ions.

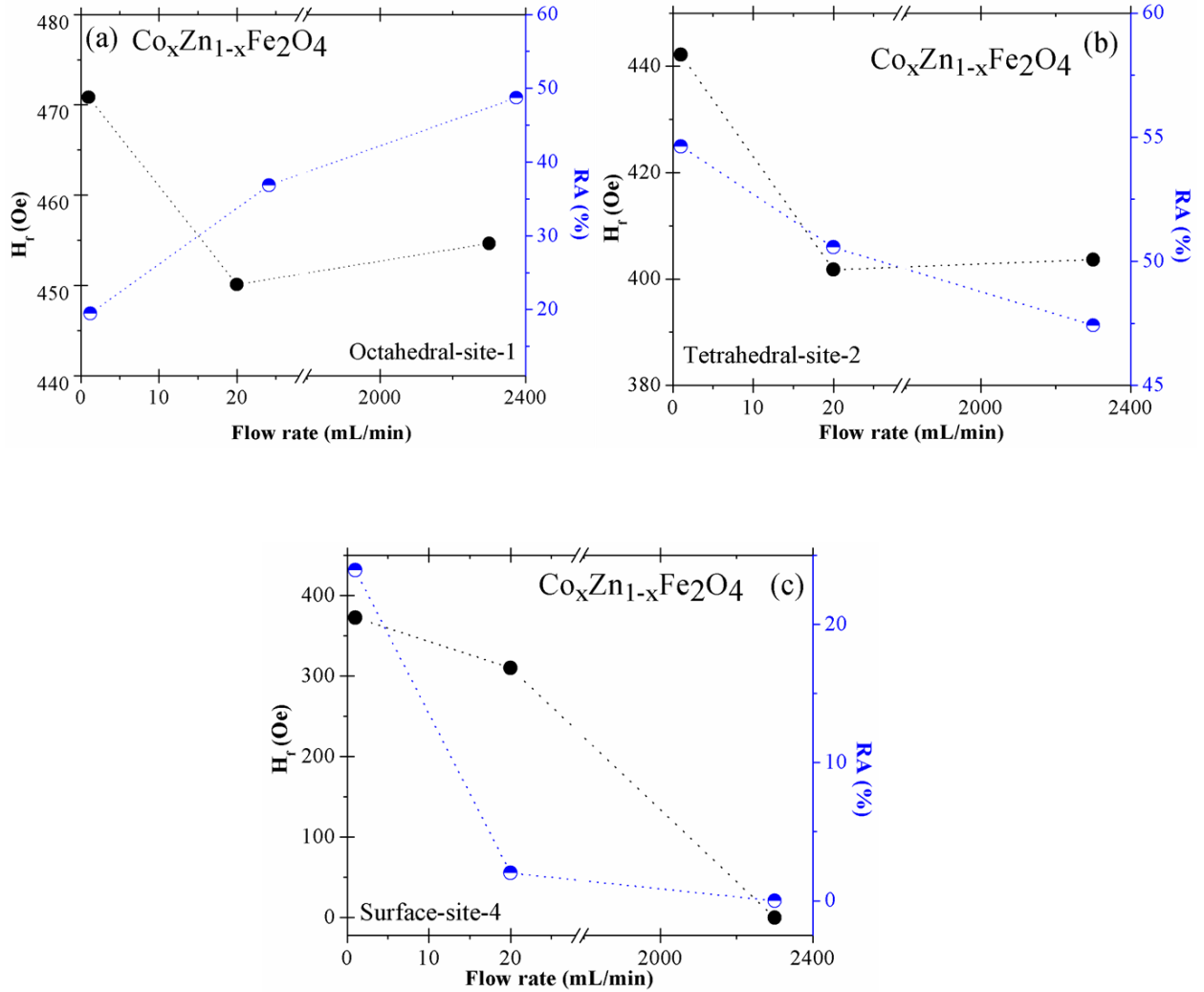


**Figure 43.** Mössbauer parameters  $H_f$  (Oe) and (RA%) for CoZn ferrite ( $x=0.9$ ) as function of flow-rate for the octahedral site, (a), tetrahedral site, (b), and surface, (c).

Taking into account that a Fe-ion in the B-site is surrounded by 6 magnetic ions of the A-site, and a Fe-ion in the A site is surrounded by 12 magnetic ions of B-site, an increase of the Fe-population in the A-site implies an increase of the nearest magnetic neighbors for the Fe-ion located in the B-site. As the number of Fe(A)-O-Fe(B) bonds increases, the internal magnetic field at the B-site increases.

#### 5.1.2.4. Concluding Remarks

The average crystallite size was increases from  $(6.50 \pm 0.21)$  nm to  $(13.08 \pm 1.01)$  nm at 50% and 100%  $\text{Co}^{2+}$  atomic fraction. This variation in the crystallite size is attributed to low affinity to oxygen of  $\text{Co}^{2+}$  compared to  $\text{Zn}^{2+}$  in the intermediate ferrite compound. The crystallinity of the CoZn ferrite was corroborated by HRTEM analysis. Raman analysis suggest that the principal vibration modes were affected by the simple composition, suggest lattice distortion for  $\text{CoZn}(x=0.7)$  ferrite.

The increment of Co atomic fraction from 50% to 100%, causes an increment in the maximum magnetization from 48emu/g to 60emu/g, This variation in magnetization was attributed to the strong exchange interaction promoted by the magnetic  $\text{Co}^{2+}$  ions. The increase in coercivity with a raising Co atomic fraction, from 8 Oe to 300 Oe, was explained in terms of changes in the crystal field and in the magnetic anisotropy, due to the presence of  $\text{Co}^{2+}$  ions. As expected, the demagnetization temperature was also increased with the increment of  $\text{Co}^{2+}$  ions.

The increment in a 30% of the average crystallite size attained at lower flow-rates, particularly at 1mL/min, was caused by the promotion of heterogeneous nucleation and Ostwald ripening processes. The coercivity was enhanced in a factor to 9 in the sample synthesized at 1mL/min. This fact was attributed to the formation of the random spin canting, which promoted the magnetically dead surface layer, and the enlargement of the crystal size within the single magnetic domain range. The pyromagnetic coefficient ( $\Delta M/\Delta T$ ) did not change with the synthesis method and varied between 0.19 emu/g-K and 0.17 emu/g-K when 'x' in the 0.5-0.9 interval.

## 5.2 Effect of Temperature on the $\text{Co}_x\text{Zn}_{1-x}\text{Fe}_2\text{O}_4$ ( $x=0.7$ ) Nanoparticles Synthesized by Hydrothermal Method

The hydrothermal technique is advantageous for obtaining nanoparticles with narrow size distribution, as well as for the growth of crystals with polymorphic modification, and growth of crystals with low and ultra low solubilities. For the present work this process was used in order to study the effect of temperature and pressure in the formation of the  $\text{Co}_{0.7}\text{Zn}_{0.3}\text{Fe}_2\text{O}_4$  ferrite nanoparticles, synthesized under the same chemical conditions of the co-precipitation method.

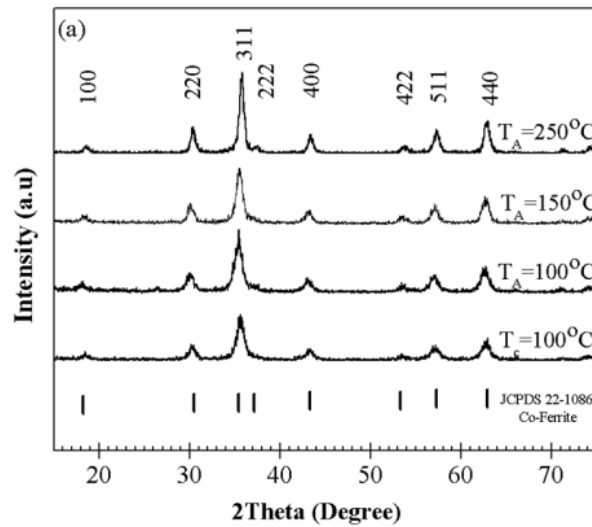
### 5.2.1. Structural Analyses

All the diffraction peaks match well the characteristic diffraction of  $\text{CoFe}_2\text{O}_4$  (JCPDS file no 22-1086). Figure 44(a) shows the XRD patterns for the  $\text{Co}_{0.7}\text{Zn}_{0.3}\text{Fe}_2\text{O}_4$  samples synthesized by co-precipitation at 100 °C and hydrothermal method at 100-250 °C of temperature range. The XRD patterns clearly evidence the formation of the spinel structure in which no secondary phases appear. Very well defined and sharp peaks and an increase of intensity with increasing temperature and pressure evidence high crystallinity. The average crystallite size was calculated using Scherrer's equation in the crystallographic plane 400 and 440. The *Table 11* shows that the average crystallite size was increased from (9.96±0.16) nm to (14.73±0.24) nm, for 100°C and 250°C respectively, and the lattice parameter remains approximately constant ( $a = 0.838\pm 0.001\text{nm}$ ), approaching the bulk value of Co-ferrite. When comparing the  $\text{Co}_{0.7}\text{Zn}_{0.3}\text{Fe}_2\text{O}_4$  samples synthesized by co-precipitation with the ones synthesized by the hydrothermal method at 100 °C, an increase of the average crystal size from (8.2±0.09) nm to (9.96±0.16) nm was found. These results were expected since at high temperatures the diffusion process is better controlled and dissolution of smaller crystals is

promoted while promoting crystal growth by Ostwald ripening process. The nanoparticles were produced because the high temperatures cause the metal hydroxides to form rapidly before significant growth takes place. The rate of dehydration could increase while the particle size is small and the reaction rate could be less affected by the diffusion through the particles. Figure 44(b-c) show the average crystallite size and lattice parameter as function of synthesis temperature with the respective error bar.

**Table 11.** Average crystal size,  $D$ , and lattice parameter,  $a$ , for the  $Co_{0.7}Zn_{0.3}Fe_2O_4$  ferrite at different temperatures of the synthesis. The powders were synthesized by co-precipitation ( $T=100^{\circ}C$ ) and hydrothermal method ( $100^{\circ}C-250^{\circ}C$ ).

Temperature $^{\circ}C$	Pressure (psi)	$D_{400} \pm \Delta D_{400}$ (nm)	$D_{440} \pm \Delta D_{440}$ (nm)	$D \pm \Delta D$ (nm)	$a \pm \Delta a$ (nm)
100	14.7	$8.1 \pm 0.08$	$8.12 \pm 0.07$	$8.2 \pm 0.09$	$0.835 \pm 0.0002$
100	22	$10.12 \pm 0.12$	$9.80 \pm 0.08$	$9.96 \pm 0.16$	$0.839 \pm 0.0001$
150	120	$10.41 \pm 0.12$	$11.01 \pm 0.07$	$10.71 \pm 0.3$	$0.836 \pm 0.0005$
250	580	$14.49 \pm 0.13$	$14.97 \pm 0.07$	$14.73 \pm 0.24$	$0.839 \pm 0.0008$



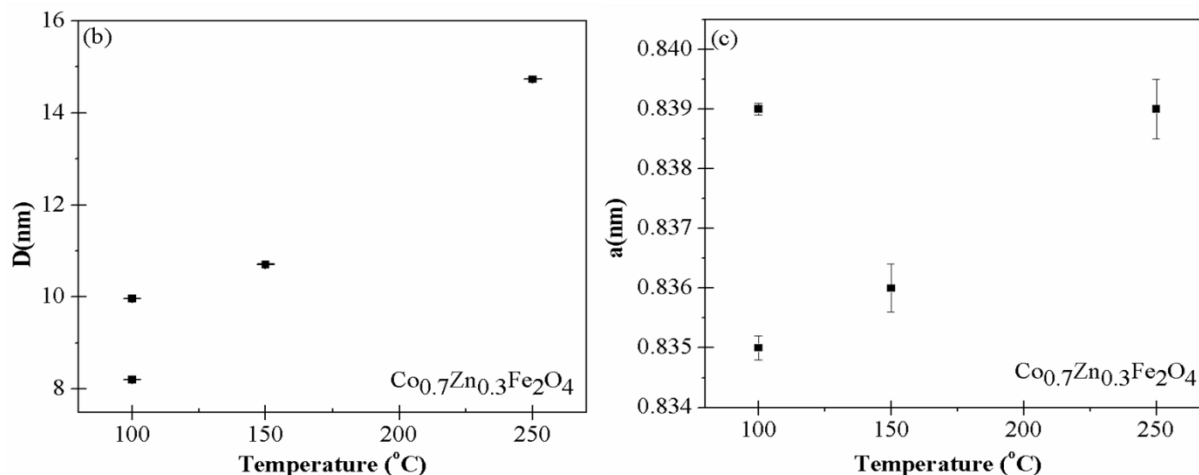


**Figure 44.** (a) XRD spectra for  $\text{CoZn}$  ( $x=0.7$ ) ferrite synthesized by hydrothermal method and co-precipitation ( $T_c$ ); (b) average crystallite size as function of synthesis temperature [lower point at 100 °C corresponds to the sample produced by co-precipitation], and (c) lattice parameter as function of the synthesis temperature [lower point at 100 °C corresponds to the sample produced by co-precipitation].

### HRTEM analysis for Co-Zn ferrite nanocrystals ( $x=0.7$ ) synthesized by hydrothermal method

Figure 45 TEM images corresponding to Co-Zn ( $x=0.7$ ) ferrite nanocrystals synthesized without control on flow-rate, (a), by hydrothermal method at 100 °C, (b), and 250 °C, (c). Particles sizes of, ~9 nm, ~13 nm, and ~16 nm, respectively, are observed. These sizes agree well with the values estimated from XRD analyses, which suggests the formation of single crystals. Some individual particles clearly show the lattice fringes, evidencing the high crystallinity of the products even at the nanoscale.

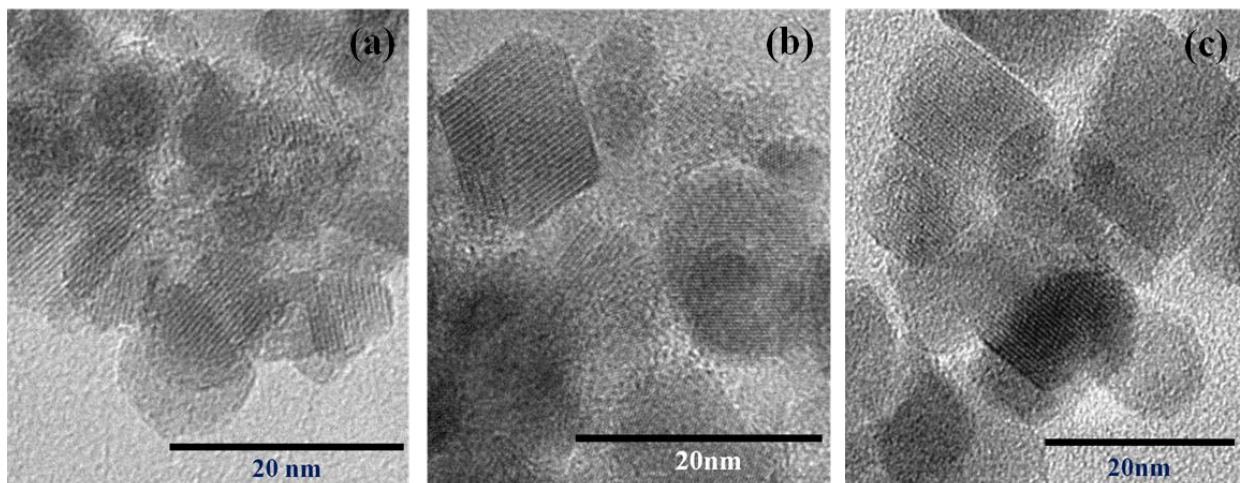


**Figure 45.** TEM images for Co-Zn ferrite ( $x=0.7$ ) synthesized by: (a) co-precipitation, and hydrothermal method at  $100^{\circ}\text{C}$ , (b) and  $250^{\circ}\text{C}$ , (c). Lattice fringes are clearly visible in all cases.

### 5.2.2. Magnetic Measurements

The M-H curve of the  $\text{Co}_{0.7}\text{Zn}_{0.3}\text{Fe}_2\text{O}_4$  synthesized by hydrothermal method at  $100^{\circ}\text{C}$ ,  $150^{\circ}\text{C}$  and  $250^{\circ}\text{C}$  are shown in the Figure 46(a), in (b) and (c) the plots of the magnetization and coercivity as function of temperature are shown. The maximum magnetization and coercivity increase from  $66\text{emu/g}$  to  $73\text{emu/g}$  and from  $55\text{Oe}$  to  $559\text{Oe}$  when the temperature increases from  $100^{\circ}\text{C}$  to  $250^{\circ}\text{C}$  (Table 12). The increment in the magnetic properties is associated with the increment in the size of the nanoparticles and the change of shape, which influences the surface anisotropy. Furthermore, the high temperatures would promote the migration of the  $\text{Fe}^{3+}$  to octahedral site, enhancing the strength of the interaction  $\text{Fe}^{3+}\text{-O-Fe}^{3+}$ .

**Table 12.** Summary of magnetic properties for the  $\text{Co}_{0.7}\text{Zn}_{0.3}\text{Fe}_2\text{O}_4$  ferrite at different temperatures of the synthesis. The powders were synthesized by co-precipitation ( $T=100^\circ\text{C}$ ) and hydrothermal methods.

Temperature $^\circ\text{C}$	Vapor Pressure (psi)	M(emu/g)	H(Oe)
100	14.7	63	35
100	22	66	55
150	120	69	200
250	580	73	559

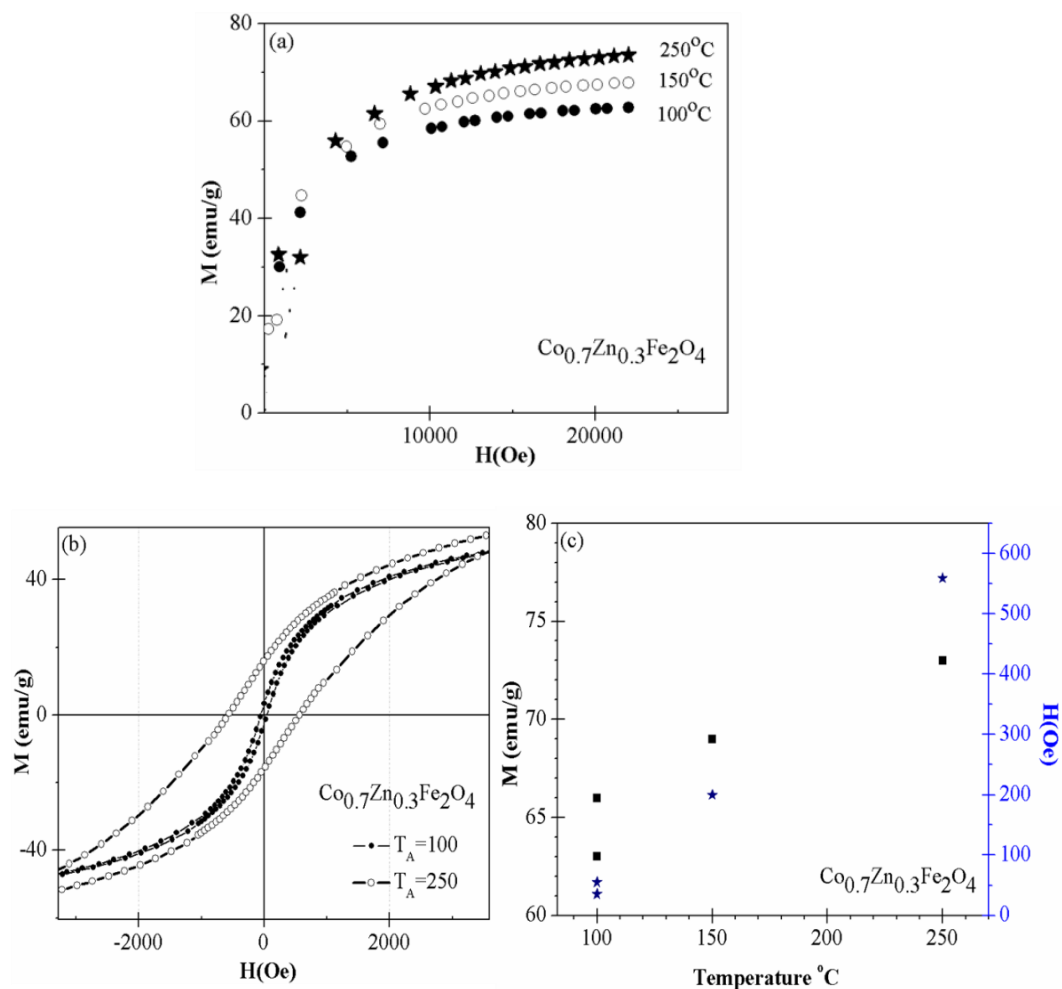


**Figure 46.** (a)  $M$ - $H$  curves for  $\text{CoZn}$  ( $x=0.7$ ) ferrite synthesized by the hydrothermal method at 100°C, 150°C and 250°C; (b) complete hysteresis loops for  $\text{CoZn}$  ( $x=0.7$ ) ferrite synthesized by the hydrothermal method at 100°C and 250°C; (c) maximum magnetization and coercivity as function of temperature.

### **M-T measurements for Co-Zn (x=0.7) ferrite synthesized by hydrothermal method**

M-T profiles for Co-Zn ferrite powders synthesized by hydrothermal method at 100°C, 150°C, and 250°C are shown in Figure 47. These measurements were carried out under an external magnetic field of 5kOe. The demagnetization temperature,  $T_d$ , was determined by extrapolating the linear part of the M-T plot to zero magnetization. The estimated  $T_d$ -values increased from 350 °C to 390°C for the synthesis temperature between 100°C and 250°C, respectively (*Table 12*). This behavior can be explained in terms of the crystal growth within the ferrite single domain region, which in turn promotes an enhancement of the coercivity.

The corresponding pyromagnetic coefficients increased slightly from 0.16 emu/g-K for the sample synthesized at  $T=100^\circ\text{C}$  to 0.19 emu/g-K for the sample synthesized at  $T = 250^\circ\text{C}$ .

**Table 13.** Demagnetization temperature for the  $\text{Co}_{0.7}\text{Zn}_{0.3}\text{Fe}_2\text{O}_4$  ferrite at different temperatures of the synthesis. The powders were synthesized by co-precipitation and hydrothermal methods.

<b>Sample Co -Zn (x=0.7)</b>	<b><math>T_d</math> (°C)</b>
100	350
150	375
250	390

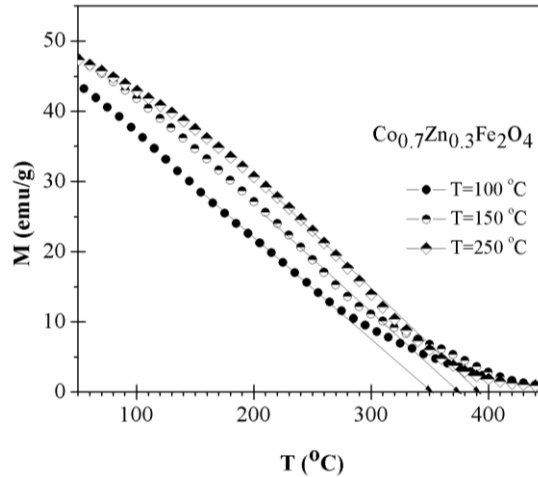


**Figure 47.** *M-T profiles for CoZn ferrites ( $x=0.7$ ), synthesized by hydrothermal method at  $T=100^{\circ}\text{C}$ ,  $150^{\circ}\text{C}$ , and  $250^{\circ}\text{C}$ . The arrows indicate the demagnetization temperatures. The external magnetic field was 5 kOe.*

### 5.2.3. Concluding Remarks

The average crystallite size of CoZn ( $x = 0.7$ ) ferrite synthesized by the hydrothermal method increased from  $(9.96 \pm 0.24)$  nm to  $(14.73 \pm 0.24)$  nm, when the synthesis temperature varied from  $100^{\circ}\text{C}$  to  $250^{\circ}\text{C}$ . At higher temperatures, the dissolution of smaller particle and the growth of the larger ones were promoted. The corresponding crystal growth explains the rise in both, coercivity, and demagnetization temperature. The increases in the maximum magnetization can be a consequence of differences in the distribution of the magnetic ions in the ferrite structure promoted by the higher temperatures.

### **5.3 Effect of Dy Doping on the Structural and Magnetic Properties of $\text{Co}_x\text{Zn}_{1-x}\text{Fe}_2\text{O}_4$ (x=0.7) Ferrite Nanocrystals**

#### **5.3.1. Conventional (i.e, no control on flow-rate) ferrite synthesis**

##### **5.3.1.1. Structural Analyses**

Figure 48 shows the results of XRD measurements for samples synthesized with different Dysprosium (Dy) atomic fraction. The absence of any isolated diffraction peaks of Dy-oxides suggests its incorporation into the Fe-sub lattice. The average crystallite size of the ferrite particles synthesized with no control on flow-rate was dependent on the atomic fraction of  $\text{Dy}^{+3}$  ('y') and varied from  $(8.2\pm 0.09)$  nm ( $y = 0$ ) to  $(17.25\pm 0.13)$  nm ( $y = 0.2$ ). Presumably, the Dy-fraction affected the solubility of the hydroxide precursors and therefore, the nucleation rate of ferrite particles. The ferrite lattice parameter without doping was  $(0.835\pm 0.0002)$  nm not differing so much from the values in doped samples, which varied between  $(0.832\pm 0.0017)$  nm and  $(0.838\pm 0.0023)$  nm, which is in good agreement with the bulk value for cobalt ferrite and zinc ferrite  $a=0.838$  nm<sup>70</sup> and  $a=0.843$ nm<sup>70</sup>, respectively. Similar observations are found for different flow rates as suggested by the XRD peak sharpening in those sample produced at lower flow-rates (see next section).

**Table 14.** Average crystallite size,  $D$ , lattice parameter,  $a$ , for Gd doped Co-Zn ferrite synthesized at different Dy atomic fractions, 'y' by conventional co-precipitation method.

Sample ( $\text{Co}_{0.7}\text{Zn}_{0.3}\text{Fe}_{2-y}\text{Dy}_y\text{O}_4$ )	$D_{400} \pm \Delta D_{400}$ (nm)	$D_{440} \pm \Delta D_{440}$ (nm)	$D \pm \Delta D$ (nm)	$a \pm \Delta a$ (nm)
y=0.00	8.1±0.08	8.12±0.07	8.2±0.09	0.835±0.0002
y=0.01	9.34±0.12	9.52±0.08	9.43±0.13	0.838±0.0007
y=0.03	11.09±0.06	11.64±0.08	11.37±0.40	0.836±0.0007
y=0.05	13.14±0.13	13.34±0.07	13.24±0.14	0.838±0.0023
y=0.1	15.65±0.20	15.88±0.09	15.77±0.16	0.835±0.0006
y=0.2	17.16±0.20	17.34±0.15	17.25±0.13	0.832±0.0017

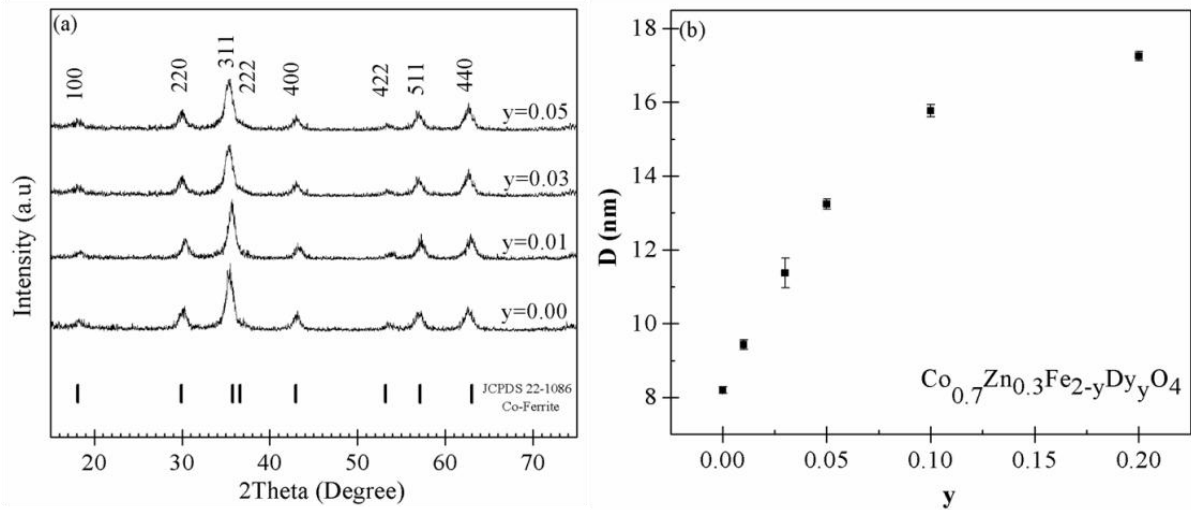


**Figure 48.** (a) XRD spectra for Dy-doped CoZn ( $x=0.7$ ) ferrite synthesized by co-precipitation; (b) average crystallite size as a function of Dy-concentration 'y'.

### Raman Analyses of Dy (0.01) doped Co-Zn ferrite nanocrystals

Co-ferrite has an inverse spinel structure with cubic  $\text{Oh}^7$  ( $\text{Fd}3\bar{m}$ ) symmetry that explain the five active Raman modes,  $3 T_{2g} + E_g + A_{1g}$ . The details of the Raman spectra for ferrites,

however, can vary depending on the composition 9. Generally, the modes below about  $600\text{ cm}^{-1}$  are attributed to vibrations of oxygen within the octahedral site, while vibrations within tetrahedral sites appear above  $600\text{ cm}^{-1}$ . T. Yu et al. identified the two most intense Raman modes in Co-ferrite nanocrystals as the octahedral  $T_{2g}$  band centered on  $474\text{ cm}^{-1}$  and the tetrahedral  $A_{1g}$  one at  $682\text{ cm}^{-1}$  71. Figure 49 shows Raman spectra for non-doped and  $y = 0.01$  doped ferrite nanocrystals. In both cases, the samples were synthesized with no control on flow rate. For the non-doped ferrite sample, the two most intense Raman bands appeared at  $468\text{ cm}^{-1}$  and  $619\text{ cm}^{-1}$  and can be assigned to the  $T_{2g}$  and  $A_{1g}$  modes, respectively. The intensity of the two previously identified Raman modes decreased and was shifted to  $479\text{ cm}^{-1}$  ( $T_{2g}$ ) and  $630\text{ cm}^{-1}$  ( $A_{1g}$ ), respectively, for the Dy-doped sample. This shift in the Raman bands can be attributed to the actual incorporation of Dy-dopant in to the ferrite lattice<sup>84</sup>. Furthermore, the spectra did not exhibit any other Raman modes that would correspond to impurity phases.

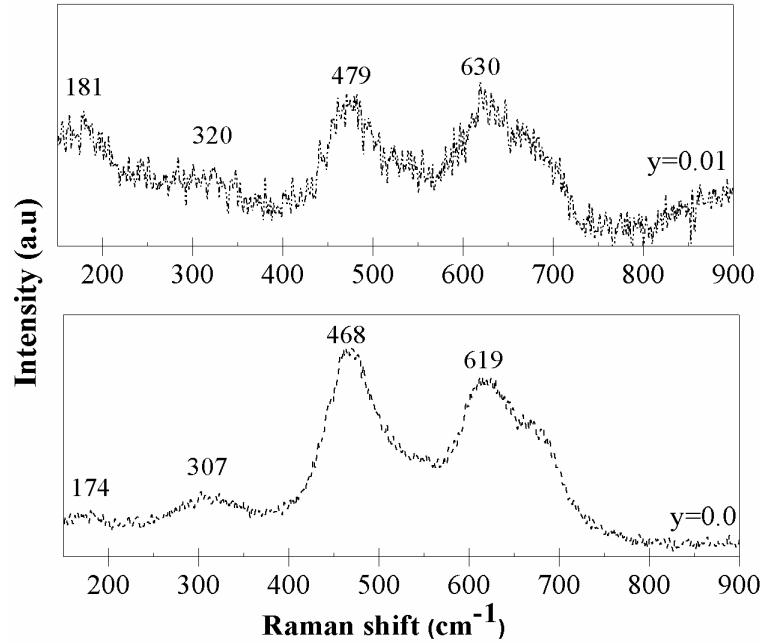


**Figure 49.** Raman spectra of non-doped ( $y = 0.0$ ) [lower panel] and Dy-doped Co-Zn ferrite ( $y = 0.01$ ) [upper panel].

### 5.3.1.2. Magnetic Measurements

Doping rare earth ions into ferrites is generally known to decrease the maximum magnetization, because of their paramagnetic nature and lower magnetic moments as compared to ferromagnetic  $\text{Fe}^{3+}$ . Some of the rare earth ions like  $\text{Dy}^{3+}$  ( $5\mu_{\text{B}}$ ) have magnetic moments compared to  $\text{Fe}^{3+}$  ions ( $5\mu_{\text{B}}$ ).

Figure 50 shows the room-temperature M-H profiles for Co-Zn ferrite without ( $y = 0.0$ ) and with Dy-doping in the 0.01 - 0.2 range. All samples were synthesized with no control of flow-rate. The drop in the maximum magnetization from 63 emu/g ( $y = 0.00$ ) to 29 emu/g ( $y = 0.2$ ) can be attributed to the disturbance of the antiferromagnetic exchange interaction in the ferrite lattice by substitution of ferromagnetic  $\text{Fe}^{3+}$ -ions by paramagnetic  $\text{Dy}^{3+}$ -ions. The  $\text{Dy}^{3+}\text{-O-Dy}^{3+}$  and  $\text{Fe}^{3+}\text{-O-Fe}^{3+}$  superexchange interactions are weak, because of the stronger localization of the 4f electrons and screening by the outer shell  $5s^2$  and  $5p^6$  electrons.

Another reason for this reduction is perhaps spin canting in the B-sublattice and can be explained on the basis of the Yafet–Kittel model of triangular spins<sup>24</sup>.

The corresponding coercivity also decreased slightly from 28 Oe to 18 Oe. In general, introducing RE ions in small quantities into the spinel structure increases the coercivity<sup>30</sup>.

The reason for this behavior may lie in the larger ionic radii of rare earth ions compared to Fe<sup>3+</sup> ions. Hence, the low crystal field symmetry and low electric potential may lead to a strong magnetocrystalline anisotropy. On the other hand, stronger spin-orbit coupling is promoted by the RE ions.

The earlier mentioned decrease in the coercivity can be attributed to rearrangement of the ions in the spinel structure, to volumen/surface ratio effects, and to polycrystallinity of the samples<sup>30</sup>. *Table 14* summarizes the magnetization and coercivity data.

**Table 15.** Magnetization (*M*) and coercivity (*H*) of Dy-doped CoZn ferrite synthesized at different Dy atomic fractions, ‘y’, synthesized by the co-precipitation method without flow rate control.

Sample Dy-concentration	M (emu/g)	H(Oe)
y= 0.0	63	28
y= 0.01	55	28
y= 0.03	54	28
y= 0.05	53	20
y= 0.1	47	20
y= 0.2	29	18

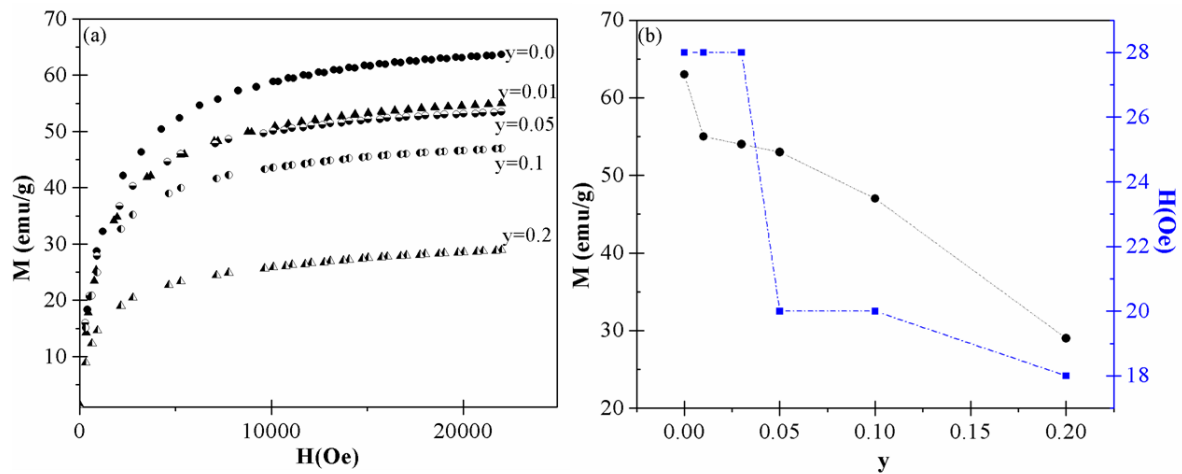


**Figure 50.** (a) *M-H* curves of Dy doped CoZn ( $x=0.7$ ) ferrite synthesized by co-precipitation method; (b) maximum magnetization and coercivity as function of the Dy atomic fraction, 'y'. The lines are guide to the eyes.

### M-T measurements for Dy doped $\text{Co}_x\text{Zn}_{1-x}\text{Fe}_2\text{O}_4$ ( $x=0.7$ ) ferrite

M-T profiles for the above mentioned Co-Zn ferrite powders are shown in Figure 51. These measurements were carried out under an external magnetic field of 5kOe. The demagnetization temperature,  $T_d$ , was determined by extrapolating the linear part of the M-T plot to zero magnetization. Accordingly, estimated  $T_d$ -values decrease from 350 °C to 245°C for Dy-doping levels between 0.00 and 0.2, respectively, see *Table 16*. The weakening of the Fe-Dy super-exchange interaction when  $\text{Fe}^{3+}$  is substituted by  $\text{Dy}^{3+}$  (due to screening of the

4f electrons by the outer electrons), and the paramagnetic character of the Dy<sup>3+</sup> ions could explain this trend in T<sub>d</sub>. A similar behavior has also been previously reported<sup>85,86</sup>.

The corresponding pyromagnetic coefficients increased from 0.16 emu/g-K (y =0.0) to 0.20 emu/g-K (y = 0.01). This increase doesn't appear significant, since the values for Co-Zn and Mn-Zn ferrite are around 0.3 emu/g-K<sup>77,78</sup>.

**Table 16.** Demagnetization temperature (T<sub>d</sub>) for Dy-doped CoZn ferrite at different Dy atomic fractions, 'y'. Samples were synthesized by the conventional co-precipitation method.

Sample Dy-concentration	T(°C)
y= 0.0	350
y= 0.01	320
y= 0.05	308
y= 0.1	285
y= 0.2	245

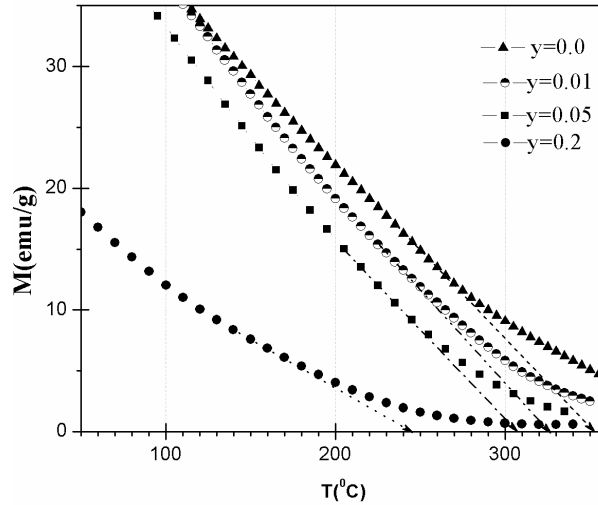


**Figure 51.** *M-T profiles for Co-Zn ( $x=0.7$ ) ferrite at different Dy-concentrations. The dotted lines extrapolate the linear part of the curves and indicate the demagnetization temperature  $T_d$ .*

### 5.3.2. Size-controlled synthesis

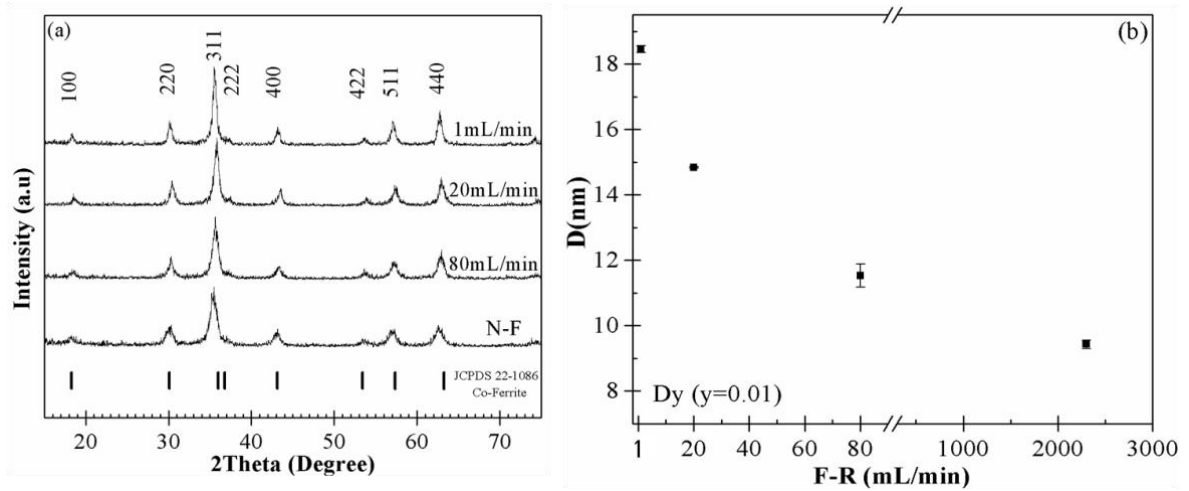
#### 5.3.2.1. Structural Analyses

Figure 52 shows the results of XRD measurements for samples synthesized at various flow rates in the 1 mL/min-80 mL/min range. The pattern indicating “no flow rate” corresponds to synthesis by the traditional co-precipitation method. The absence of any isolated diffraction peaks of Dy-oxides suggests its incorporation into the Fe-sub lattice. The most remarkable effect of the flow-rate control was on the average crystallite size of the particles, which was enlarged from  $(9.43 \pm 0.13)$  nm (with no control) up to  $(18.45 \pm 0.11)$  nm (at 1 mL/min) for ferrites doped with  $y = 0.01$ . The suitable control of the oversaturation condition in the reacting solution, enabled by the control of the flow-rate at which the reactants are contacted, should have promoted heterogeneous nucleation and hence, crystal growth. The ferrite lattice parameter without doping was  $(0.835 \pm 0.0002)$  nm not differing so much from the values in doped samples, which varied between  $(0.832 \pm 0.0017)$  nm and

( $0.838 \pm 0.0023$ ) nm, which is in good agreement with the bulk value for cobalt ferrite and zinc ferrite,  $a=0.838 \text{ nm}^{70}$  and  $a=0.843 \text{ nm}^{70}$ , respectively.

**Table 17.** Average crystallite size,  $D$ , size and lattice parameter,  $a$ , for the Dy (0.01) doped CoZn( $x=0.7$ ) ferrite synthesized by the conventional co-precipitation method.

F-R (mL/min)	$D_{400} \pm \Delta D_{400}$ (nm)	$D_{440} \pm \Delta D_{440}$ (nm)	$D \pm \Delta D$ (nm)	$a \pm \Delta a$ (nm)
N-F	$9.34 \pm 0.12$	$9.52 \pm 0.08$	$9.43 \pm 0.13$	$0.838 \pm 0.0007$
80	$11.88 \pm 0.14$	$11.18 \pm 0.08$	$11.53 \pm 0.35$	$0.836 \pm 0.0012$
20	$14.82 \pm 0.16$	$14.86 \pm 0.10$	$14.84 \pm 0.02$	$0.832 \pm 0.0026$
1	$18.56 \pm 0.13$	$18.34 \pm 0.13$	$18.45 \pm 0.11$	$0.837 \pm 0.0002$



**Figure 52.** (a) XRD spectra for CoZn ( $x=0.7$ ) ferrite doped with Dy ( $y=0.01$ ) synthesized by co-precipitation; (b) average crystallite size as function of flow rate.

**HRTEM analysis for Dy doped Co-Zn ferrite nanocrystals ( $y=0.01$ ) synthesized by the size-controlled method at 20 mL/min**

Figure 53 shows a TEM image corresponding to Dy-doped Co-Zn ferrite nanocrystals ( $y = 0.01$ ) synthesized with control on flow-rate (20 mL/min). Although particles look agglomerated, the observed particle size ( $\sim 10$  nm) is still evident and agrees well with the value estimated from XRD analyses, which suggests the formation of single crystals. Moreover, some individual particles clearly show lattice fringes, evidencing the high crystallinity of the products even at the nanoscale.

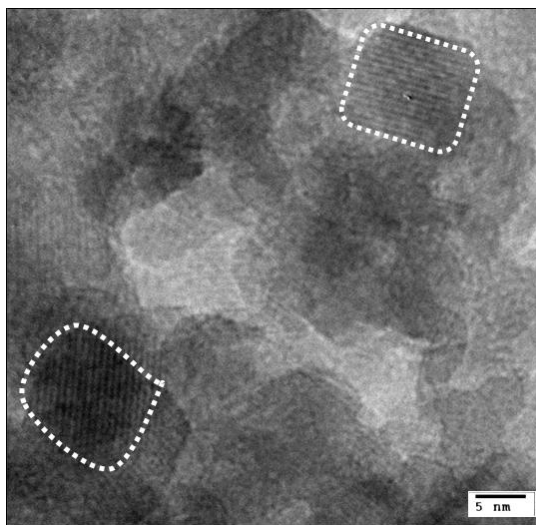


*Figure 53. TEM image of Dy-doped ( $y=0.01$ ) Co-Zn ferrite ( $x=0.7$ ) synthesized by coprecipitation at 20 mL/min flow rate. The dotted frames emphasize two crystallites with approximate sizes of 10nm. The lattice fringes are clearly visible.*

### 5.3.2.2. Magnetic Measurements

The next step was to investigate whether control of the flow rate at which the reactants are contacted would influence the magnetic properties of the resulting Co-Zn ferrite. Figure 54 (a) shows room-temperature M-H measurements for Co-Zn ( $x = 0.7$ ) ferrite with 0.01 Dy-doping synthesized at various flow-rates. The maximum magnetization increased from 55 emu/g with no control on flow-rate, up to 62 emu/g when the flow-rate was kept constant at 80 mL/min while the corresponding coercivity increased only slightly from 29 Oe to 49 Oe. On the other hand, the coercivity was dramatically increased up to 1,484 Oe for the sample synthesized at 1 mL/min. The Figure 54(b) shows full M-H hysteresis loops for  $y = 0.01$  Dy-doped samples, synthesized with 80 mL/min and 1 mL/min flow rate control. One can see the dramatic increase in the coercivity, which can be attributed to the promotion of ferrite crystal growth under these flow controlled conditions<sup>61-63</sup>.

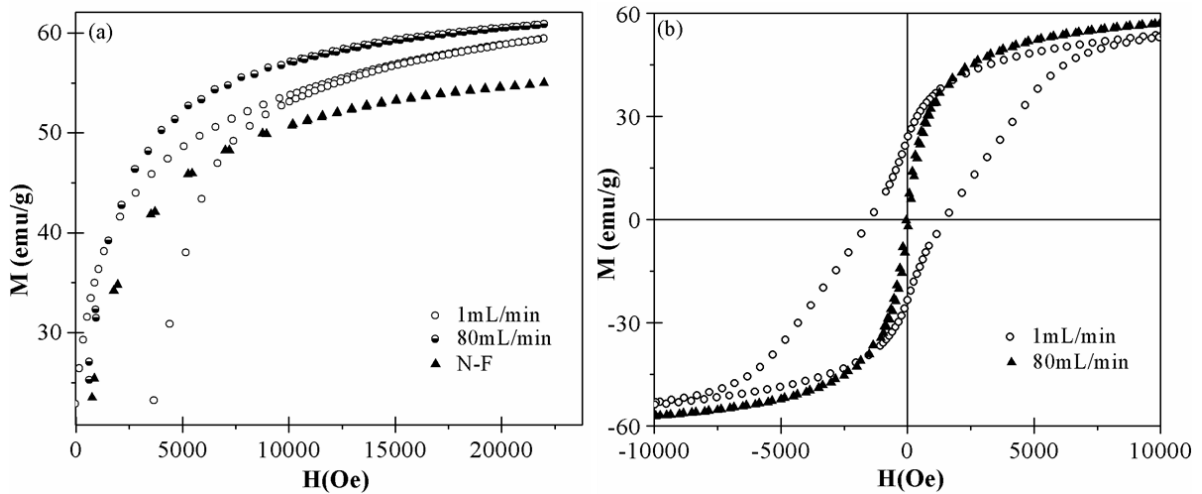


**Figure 54.** (a) M-H curves for Dy (0.01) doped CoZn ferrite ( $x' = 0.7$ ) powders synthesized with and without control of flow-rate at 1 mL/min and 80 mL/min and (b) complete hysteresis loop for the same CoZn ferrite synthesized at 1 mL/min and 80 mL/min.

### M-T measurements for Co-Zn ( $x=0.7$ ) ferrite doped with Dy ( $y0.01$ )

Figure 55 shows M-T profiles for Co-Zn ( $x=0.7$ ) ferrite with 0.01 Dy-concentration synthesized without flow-rate control (N-F) and at 1 mL/min and 80 mL/min. The demagnetization temperature is 320 °C for the synthesis without flow rate control and increases to 350 °C for 1 mL/min and then decreases again to 308 °C for 80 mL/min. This behavior is the same as seen before in Figure 39 and explained accordingly. Observed trends in  $T_d$  and magnetization in the Co-Zn ferrite system can be explained by the weak  $Fe^{3+}$ - $Dy^{3+}$  super-exchange interactions in the host ferrite lattice along with the favorable growth of the nanocrystals under flow-rate controlled synthesis conditions. The increment in the coercivity at low flow rate due to the increment in the magnetic anisotropy was discussed in the previous section.

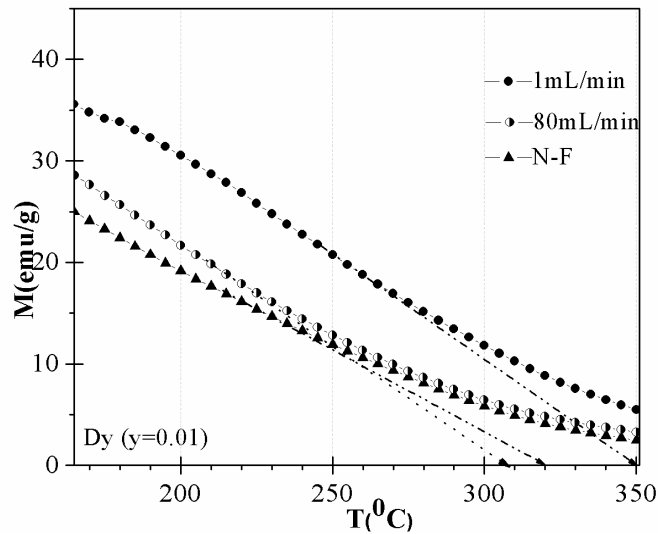


**Figure 55.** M-T profiles for Co-Zn ( $x=0.7$ ,  $y=0.01$ ) ferrite synthesized at different flow rates.

### 5.3.3. Concluding Remarks

The incorporation of the Dy causes an increment in the ferrite average crystal size, which could be attributed to the change in the solubility behavior of the ferrite precursor hosting the Dy ions. The reduction in maximum magnetization with Dy doping was due to the weak  $\text{Fe}^{3+}$ -O- $\text{RE}^{3+}$  interaction. Raman spectroscopy measurements confirmed the actual incorporation of Dy<sup>3+</sup> ions into the ferrite octahedral sites. Depending on the doping level, the demagnetization temperature was reduced from 320 °C to 245 °C.

## 5.4 Effect of Gd Doping on the Structural and Magnetic Properties of Co-Zn (x=0.7) Ferrite Nanocrystals

### 5.4.1. Conventional (i.e, no control on flow-rate) ferrite synthesis

#### 5.4.1.1. Structural Analyses

All the diffraction peaks match well the characteristic diffraction of the ferrite structure for  $\text{CoFe}_2\text{O}_4$  (JCPDS file no 22-1086). Figure 56(a) shows the XRD patterns for the Gd doped Co-Zn (x=0.7) ferrites nanocrystals synthesized by the conventional co-precipitation method. The XRD patterns evidence the formation of the spinel structure in which no secondary phases are visible. The average crystal size was calculated using Scherrer's equation in the crystallographic planes (400) and (440). *Table 17* shows that the average crystallite size was increased from (8.2±0.09) nm to (10.44±0.07) nm, when 'z' varied from 0.0 to 0.05, respectively. The lattice parameter values, 'a', varied between (0.833±0.0012) nm and (0.838±0.0007) nm, respectively, for z=0.0 and z=0.01 (see *Table 18*). Figure 56(b) shows

the average crystallite size and lattice parameter as function of Gd-concentration with the respective error bar. The increase in the average crystallite size can be attributed to the variation of the solubility of the intermediate hydroxide precursor with the different amounts of incorporated  $Gd^{3+}$  species. If the solubility conditions of the intermediate ferrite compound change, so it will do the corresponding nucleation and growth rates of the ferrite forming crystals.

**Table 18.** Average crystallite size,  $D$ , size and lattice parameter,  $a$ , for the  $Co_{0.7}Zn_{0.3}Fe_{2-z}Gd_zO_4$  ferrite synthesized at various Gd atomic fractions, 'z'. The samples were synthesized by the conventional co-precipitation method.

Gd, atomic fraction 'z'	$D_{400} \pm \Delta D_{400}$ (nm)	$D_{440} \pm \Delta D_{440}$ (nm)	$D \pm \Delta D$ (nm)	$a \pm \Delta a$ (nm)
z=0.0	8.1±0.08	8.12±0.07	8.2±0.09	0.833±0.0012
z=0.01	9.24±0.13	9.37±0.09	9.3 ±0.07	0.838±0.0007
z=0.03	10.51±0.13	10.38±0.08	10.44±0.07	0.835±0.0009
z=0.05	10.86±0.15	10.61±0.07	10.44±0.07	0.834±0.0004

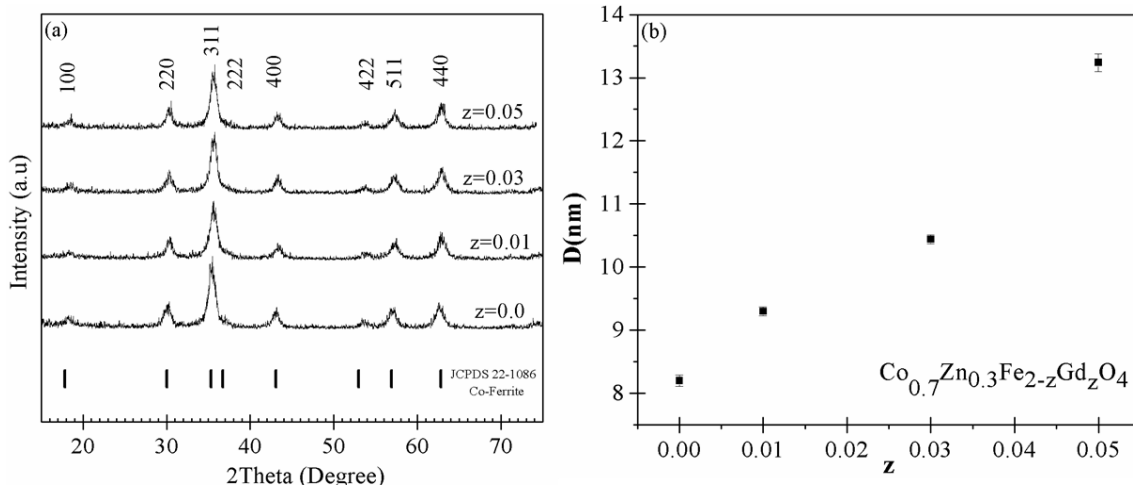


**Figure 56.** (a) XRD spectra for  $CoZn$  ( $x=0.7$ ) ferrite doped with  $Gd$ ; (b) ferrite average crystallite size as function of  $Gd$ -concentration 'z'.

### 5.4.1.2. Magnetic Measurements

Figure 57 shows the room-temperature M-H profiles for Co-Zn ferrite without ( $z = 0.0$ ) and with Gd-doping in the 0.01 - 0.05 range. All samples were synthesized with no control of flow-rate. The drop in the maximum magnetization from 63 emu/g ( $z = 0.0$ ) to 53 emu/g ( $z = 0.05$ ) can be attributed to the reduction in the net magnetic moment of the material, due to the presence of  $Gd^{3+}$  ions with  $3\mu_B$  replacing  $Fe^{3+}$  with  $5\mu_B$ , and the weak antiferromagnetic exchange interaction in the ferrite lattice by substitution of ferromagnetic  $Fe^{3+}$ -ions by paramagnetic  $Gd^{3+}$ -ions. Meanwhile, the corresponding coercivity also decreased from 28 Oe to 20 Oe. This change in the coercivity is not significant and can be within the measurement error. *Table 18* summarizes the magnetization and coercivity data.

**Table 19.** Magnetization ( $M$ ) and coercivity ( $H$ ) of  $Co_{0.7}Zn_{0.3}Fe_{2-z}Gd_zO_4$  ( $z=0.01, 0.03, 0.05$ ), synthesized by the conventional co-precipitation method.

Sample Gd-concentration	M (emu/g)	H(Oe)
$z= 0.0$	63	28
$z= 0.01$	55	28
$z= 0.03$	54	28
$z= 0.05$	53	20

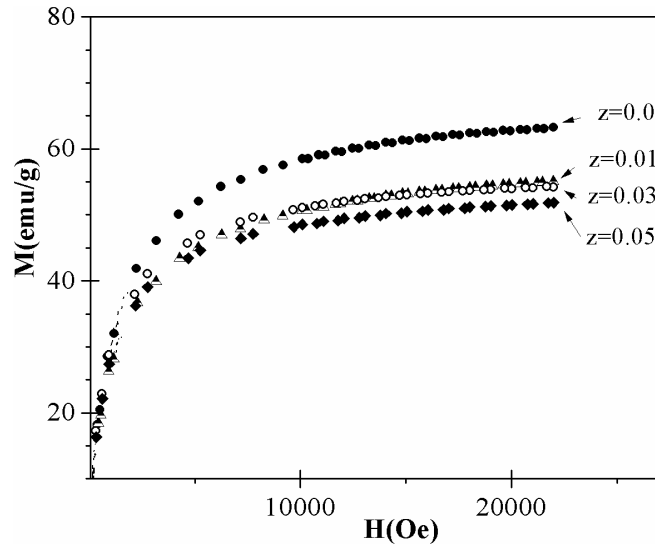


**Figure 57.** *M-H curves of Gd doped CoZn ( $x=0.7$ ) ferrite synthesized by co-precipitation method.*

#### **M-T measurements for Gd doped $\text{Co}_x\text{Zn}_{1-x}\text{Fe}_2\text{O}_4$ ( $x=0.7$ ) ferrite nanocrystals**

M-T profiles for the Co-Zn ferrite powders doped with different Gd-atomic fractions are shown in Figure 54. These measurements were carried out under an external magnetic field of 5kOe. The demagnetization temperature,  $T_d$ , was determined by extrapolating the linear part of the M-T plot to zero magnetization. Accordingly, estimated  $T_d$ -values decrease from 350 to 230°C for Gd-doping levels between 0.00 and 0.05, respectively. The weakening of the Fe-RE super-exchange interaction when  $\text{Fe}^{3+}$  is substituted by  $\text{Gd}^{3+}$  (due to screening of the 4f electrons by the outer electrons), and the paramagnetic character of the  $\text{Gd}^{3+}$  ions could explain this trend in  $T_d$ . A similar behavior has also been previously reported<sup>85,86</sup>.

The corresponding pyromagnetic coefficients increased from 0.16 emu/g-K ( $y=0.0$ ) to 0.59 emu/g-K ( $y=0.05$ ). This increase appears significant, since the values for other Mn-Zn ferrites are generally around 0.3 emu/g-K. Regarding the envisioned applications of our nanomaterials, the doping of the CoZn ferrite with Gd species will promote both, the drop in

the demagnetization temperature (it decreased from 350°C down to 230°C) and a remarkable increase of the pyromagnetic coefficient. The moderate magnetization and minimum coercivity of these nanoparticles enable them to be considered a very promising option for their application in magnetocaloric pumping systems.

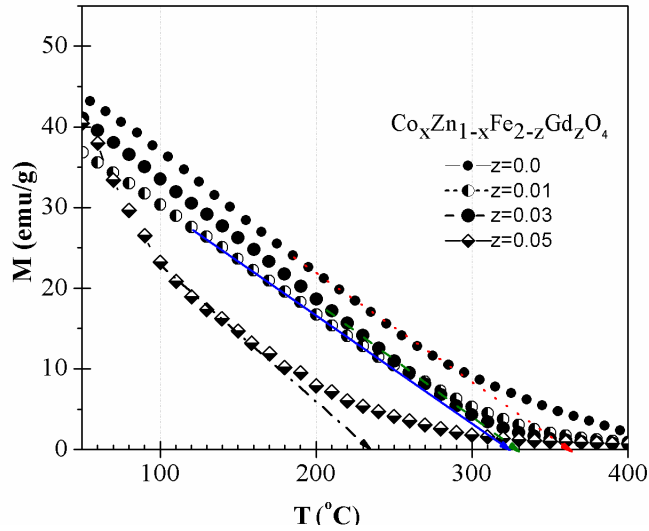


**Figure 58.** *M-T profiles for Co-Zn ( $x=0.7$ ) ferrite with Dy-concentration ( $z=0.0 - 0.2$ ) synthesized by the conventional co-precipitation method.*

## 5.4.2. Size-controlled synthesis

### 5.4.2.1. Structural Analyses

For this set of samples, data obtained for the synthesis at 1 mL/min is not included, because the obtained properties are not favorable for magnetocaloric pump applications.

The influence of flow-rate control on the crystal growth was investigated for  $z = 0.01$ , and  $0.03$ , for a  $\text{Co}_{0.7}\text{Zn}_{0.3}\text{Fe}_{2-z}\text{Gd}_z\text{O}_4$  stoichiometry. Figure 59 shows the X-ray diffraction patterns for (a)  $z=0.01$  and (b)  $z=0.03$  samples synthesized at 20 mL/min, 80 mL/min, and with no control on the flow-rate (N-F). The corresponding average crystallite size was increased from  $(9.3\pm 0.07)$  nm (N-F) up to  $(14.69\pm 0.02)$  nm when 20 mL/min was selected. In turn, the

average crystallite size was increased from  $(10.44 \pm 0.07)$  nm (N-F) up to  $(14.95 \pm 0.31)$  nm for powders synthesized at ‘z’= 0.03, respectively. The promotion of heterogeneous nucleation, where early generated ferrite nuclei would act as pre-existent seeds, by the controlled addition of the reactants can explain the enlargement of crystal size. As the data in *Table 19* evidences, there was no remarkable variation in the lattice parameter with ‘z’ or the synthesis flow-rate. This parameter varied between  $(0.834 \pm 0.0004)$  nm and  $(0.838 \pm 0.0007)$  nm, which is in good agreement with the bulk value for cobalt ferrite and zinc ferrite of  $a=0.838$  nm<sup>70</sup> and  $a=0.843$ nm<sup>70</sup>, respectively.

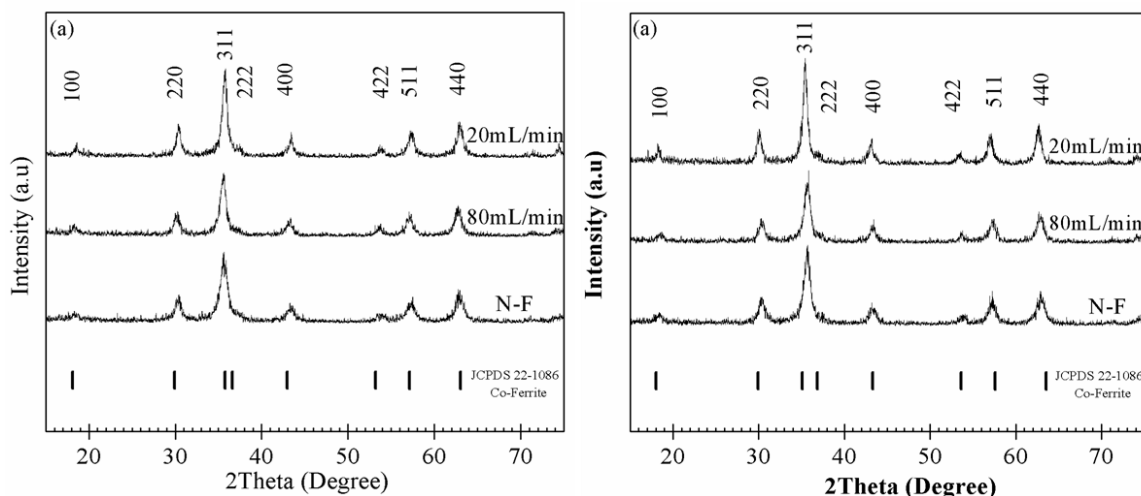


**Figure 59.** (a) XRD spectra for  $\text{CoZn}$  ( $x=0.7$ ) ferrite doped with  $\text{Dy}$  ( $y=0.01$ ) synthesized by co-precipitation at different flow rates; (b)  $\text{CoZn}$  ( $x=0.7$ ) ferrite doped with  $\text{Dy}$  ( $y=0.03$ ).

**Table 20.** Average crystallite size,  $D$ , size and lattice parameter,  $a$ , for the  $Co_{0.7}Zn_{0.3}Fe_{2-z}Gd_zO_4$  ( $z=0.01, 0.03, 0.05$ ) ferrite synthesized by the size-controlled method.

Sample		$D_{400} \pm \Delta D_{400}$ (nm)	$D_{440} \pm \Delta D_{440}$ (nm)	$D \pm \Delta D$ (nm)	$a \pm \Delta a$ (nm)
z=0.01	N-F	9.24±0.13	9.37±0.09	9.3 ±0.07	0.838±0.0007
	80mL/min	10.57±0.15	10.89±0.09	10.73±0.16	0.835±0.0003
	20mL/min	14.67±0.23	14.71±0.12	14.69±0.02	0.834±0.0014
z=0.03	N-F	10.51±0.13	10.38±0.08	10.44±0.07	0.835±0.0009
	80mL/min	12.07±0.17	11.57±0.08	12.27±0.2	0.836±0.0017
	20mL/min	14.64±0.24	15.26±0.04	14.95±0.31	0.837±0.0009

**HRTEM analysis for Gd doped Co-Zn ferrite nanocrystals (z=0.01) synthesized by conventional and size-controlled method at 80mL/min**

Figure 60 shows the TEM images corresponding to pure and Gd ( $z = 0.01$ ) doped Co-Zn ( $x=0.7$ ) ferrite nanocrystals synthesized by the conventional co-precipitation approach and at 80mL/min. Although particles look agglomerated, the observed particle sizes of respectively ~10 nm and ~13 nm are still evident and agree well with the values estimated from XRD analyses, which suggests the formation of single crystals. Moreover, some individual particles clearly show lattice fringes, evidencing the high crystallinity of the products even at the nanoscale. Also, it is clearly visible that the flow rate changes the form of the nanoparticles from quasi-spherical to polygonal-like.

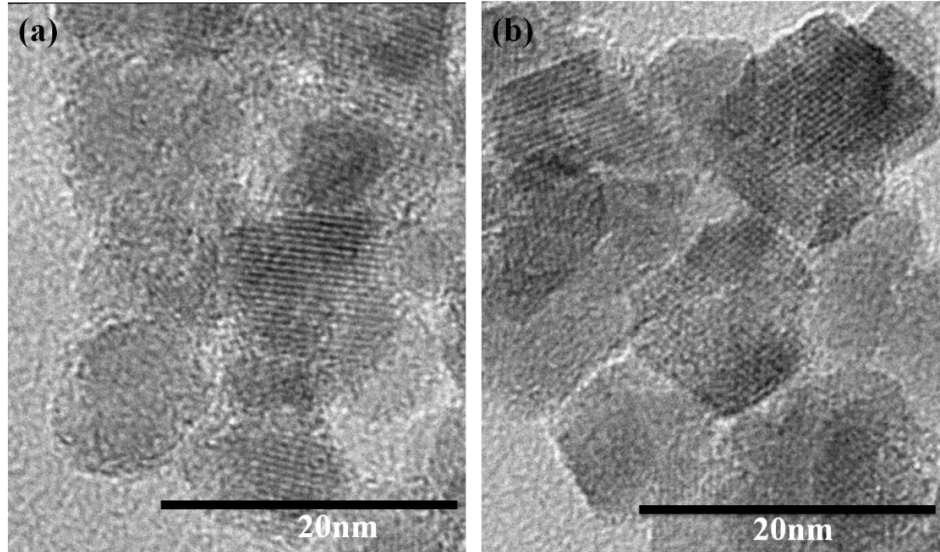


**Figure 60.** TEM images of Gd-doped ( $z=0.01$ ) Co-Zn ferrite ( $x=0.7$ ) synthesized (a) without flow rate and (b) by size-controlled co-precipitation method at 80mL/min. The lattice fringes are clearly visible.

#### 5.4.2.2. Magnetic Measurement

Figure 61(a) shows room-temperature M-H measurements for Co-Zn ( $x=0.7$ ) ferrite with (a)  $z=0.01$  and (b)  $z=0.03$  Gd atomic fraction synthesized at various fixed flow rates. The maximum magnetization for all samples was found when the flow-rate was kept constant at 80 mL/min and was virtually constant. On the other hand, the maximum magnetization for different Dy atomic fractions doped into CoZn ( $x=0.7$ ) synthesized at 80 mL/min increased. This trend can be attributed to the ion distribution in the spinel structure, apparently favoured at 80 mL/min. The corresponding coercivity increased only slightly (see *Table 20*). Furthermore, the maximum values for the coercivity were for the sample synthesized at 20 mL/min. One can see the increase in the coercivity, which can be attributed to the promotion of ferrite crystal growth under these flow controlled conditions.

**Table 21.** Maximum magnetization and coercivity for the Gd-doped  $\text{Co}_{0.7}\text{Zn}_{0.3}\text{Fe}_{2-z}\text{Gd}_z\text{O}_4$  ( $z=0.01, 0.03, 0.05$ ) ferrite synthesized by the size-controlled method.

Sample (Gd)		M (emu/g)	H(Oe)
z=0.01	N-F	55	28
	80mL/min	64	65
	20mL/min	53	140
z=0.03	N-F	54	21
	80mL/min	64	64
	20mL/min	51	124

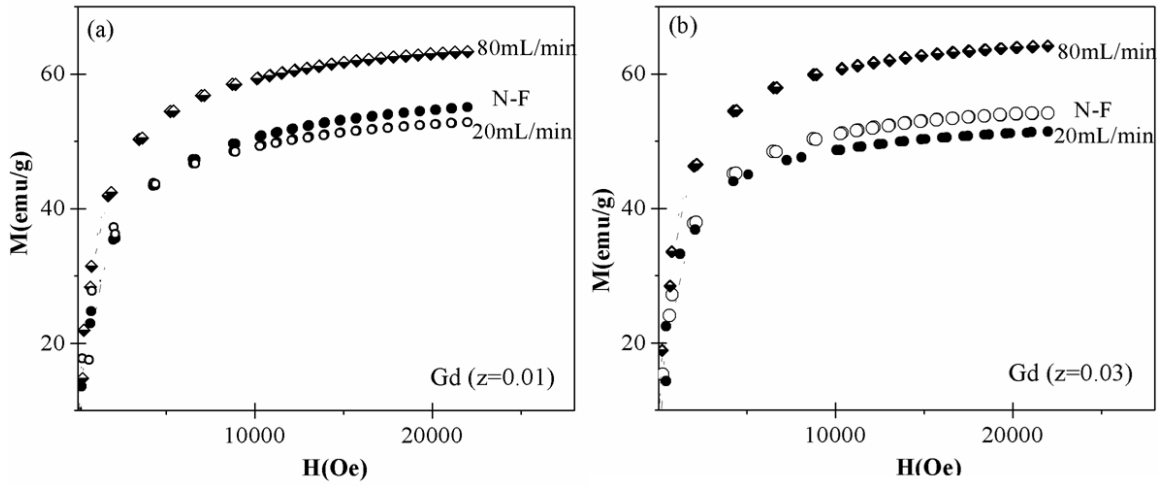


**Figure 61.** M-H curves of Gd doped CoZn ( $x=0.7$ ) ferrite synthesized by conventional (N-F,) and size-controlled method at 80 mL/min and 20mL/min. The Gd atomic fractions were, (a)  $z=0.01$ , and (b)  $z=0.03$ .

### M-T measurements for Gd doped Co-Zn ( $x=0.7$ ) ferrite nanocrystals

Figure 62 shows the M-T profiles for Co-Zn ( $x=0.7$ ) ferrite doped with 0.01 Gd-concentration synthesized without flow-rate control (N-F) and at 20mL/min and 80mL/min. The demagnetization temperature was estimated at 330 °C for the synthesis without flow rate control and increased to 350 °C for 20 mL/min.  $T_d$  slightly decrease to 340 °C for the sample synthesized at 80mL/min. This trend was similar to the one suggested by the data in Figure 41 and explained accordingly. Observed trends in  $T_d$  and magnetization in the Co-Zn ferrite system can be explained by the weak  $Fe^{3+}$ - $Gd^{3+}$  super-exchange interactions in the host ferrite lattice along with the favorable growth of the nanocrystals under flow-rate controlled synthesis conditions.

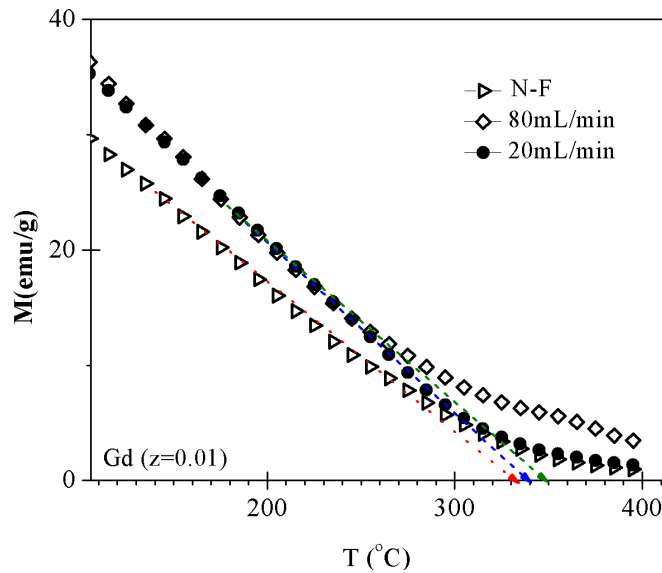


**Figure 62.** M-T profiles for Co-Zn ( $x=0.7$ ) ferrite with Gd-concentration ( $z=0.01$ ) synthesized by conventional and size-controlled co-precipitation method at 20mL/min and 80mL/min.

### 5.4.3. Concluding Remarks

Doping the CoZn ( $x=0.7$ ) ferrite with Gd promoted the enlargement in crystallite size, while decreasing the maximum magnetization, coercivity, and the demagnetization temperature. This behaviour was also found for Dy-doped system and was explained accordingly as in the section before. For Co-Zn doped with 1% Gd and synthesized by the size-controlled method at 80mL/min, the maximum magnetization increased from 54emu/g to 63 emu/g. This trend is similar as for the samples doped with 1% Dy. The demagnetization temperature remained close to the value seen for the sample synthesized without flow rate control.

Regarding the envisioned applications of our nanomaterials, the doping of the CoZn ferrite with Gd species will promote both, the drop in the demagnetization temperature (it decreased from 350°C down to 230°C) and a remarkable increase of the pyromagnetic coefficient. **The moderate magnetization and minimum coercivity of these nanoparticles, synthesized with no control on flow-rate, enable them to be considered a very promising option for their application in magnetocaloric pumping systems.**

## 5.5 Attempts to Optimize the Magnetic Properties in $Gd^{3+}$ Doped $Co_xZn_{1-x}Fe_2O_4$ ( $x=0.7$ ) Ferrite Nanocrystals Synthesized by the Conventional Co-precipitation Method

For optimum operation of the magnetocaloric pump it is required that the magnetic nanoparticles used for the magnetic fluid have certain characteristics in their structural and magnetic properties. Among other factors, it is necessary that the average crystallite size has an appropriate size. If too large, the nanoparticles will precipitate when suspended in a fluid, when too small, the maximum magnetization will be small as well. The maximum

magnetization has to be as high as possible, since this determines the changes in pressure, which ultimately drives the ferrofluid. The coercivity on the other hand should be as low as possible. The coercivity is related to the magnetic anisotropy (energy necessary to magnetize or demagnetize a solid) and for this application ferrites with low anisotropy are required. In order to find appropriate values for the ferrite particles, the effect of the interaction of two variables on the properties, in this case the Gd atomic fraction and the NaOH molarity, was evaluated.

Based on the above mentioned, the  $2^2$  factorial design was applied that permits observing when interaction between the controllable variables occurs. For further study of the results the CCD design was applied as a second stage. The  $2^2$  factorial design consists of two controllable variables, in this case Gd atomic fraction and NaOH molarity, with two levels for each variable and is formed by corner, central, and face centered points with 4 replicas in the center. On the other hand, the CCD design is based on the  $2^2$  factorial design, where axial points are added. The consistence of the design will be statistically assessed for a confidence interval  $\alpha=0.05$ .

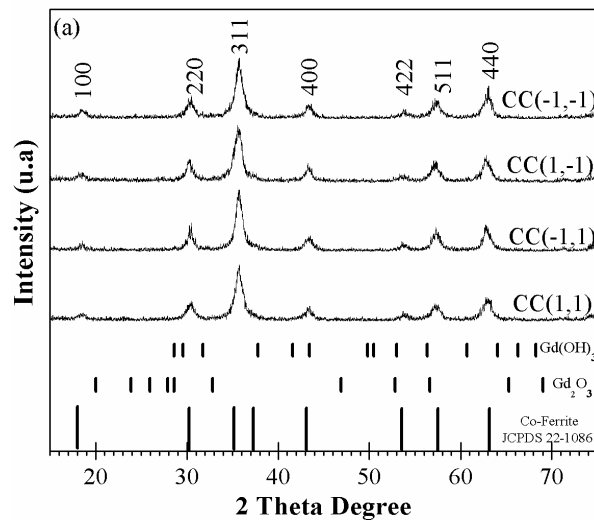
Accordingly,  $\text{Co}_{0.7}\text{Zn}_{0.3}\text{Fe}_{2-z}\text{Gd}_z\text{O}_4$  ferrite nanoparticles were synthesized by the conventional co-precipitation method. The controllable levels of the variables chosen varied in the range [0.24 – 0.72] M and [0.01 - 0.03]  $\text{Gd}^{3+}$  atomic fraction, for the  $\text{Co}_{0.7}\text{Zn}_{0.3}\text{Fe}_{2-z}\text{Gd}_z\text{O}_4$  ferrite. The dependent variables were: average crystallite size, lattice parameter, maximum magnetization and coercivity.

### 5.5.1. Effect of the selected synthesis parameters on the average crystallite size of $\text{Co}_{0.7}\text{Zn}_{0.3}\text{Fe}_{2-z}\text{Gd}_z\text{O}_4$

In the first stage of the design evaluation, the nanoparticles were synthesized according to the experimental conditions defined by the corner points and the four central points. Figure 63 shows the XRD patterns for these samples, which suggest the exclusive formation of ferrite spinel phase where secondary phases are not visible. The average crystallite size was calculated using Scherrer's equation in the crystallographic planes (400) and (440). *Table 21* shows the complete data for all samples as required by the CCD statistical model. For the samples coded with (1,-1) and (1,1), corresponding to experimental levels of 0.01 at and 0.31 M, the average crystallite size were  $(12.63 \pm 0.13)$  nm and  $(10.4 \pm 0.15)$  nm, respectively. This variation in the average crystallite size was expected because the larger concentrations of  $\text{OH}^-$ , which adsorbs on the nanocrystals surfaces, should inhibit not only the aggregation but also the growth of individual nanoparticles. For the above two samples the Gd-at and z remained constant. The same behavior occurred for the samples coded as (-1,-1) and (-1,1). The experimental levels for these two experiments were 0.01 at and 0.65 M, respectively. The corresponding results suggested that when the Gd atomic fraction is increased, while the NaOH molarity remains constant, the average crystallite size also increases.

**Table 22.** Average crystallite size,  $D$ , for the coded and experimental levels in  $2^2$  factorial and CCD experimental design applied to the synthesis of  $\text{Co}_{0.7}\text{Zn}_{0.3}\text{Fe}_{2-z}\text{Gd}_z\text{O}_4$ .

Gd (coded)	NaOH (coded)	Gd (at)	NaOH (M)	$D \pm \Delta D$ (nm)	$a \pm \Delta a$ (nm)
1	-1	0.02	0.31	$12.63 \pm 0.13$	$0.835 \pm 0.0034$
1	1	0.02	0.65	$10.4 \pm 0.15$	$0.833 \pm 0.0006$
-1	-1	0.01	0.31	$11.15 \pm 0.22$	$0.835 \pm 0.0004$
-1	1	0.01	0.65	$9.55 \pm 0.38$	$0.836 \pm 0.0007$
0	0	0.02	0.48	$10.14 \pm 1.07$	$0.835 \pm 0.0008$
0	0	0.02	0.48	$10.58 \pm 0.04$	$0.834 \pm 0.0014$
0	0	0.02	0.48	$10.56 \pm 0.47$	$0.835 \pm 0.0014$
0	0	0.02	0.48	$10.20 \pm 0.12$	$0.834 \pm 0.0014$
-1.4142	0	0.01	0.48	$8.7 \pm 0.24$	$0.836 \pm 0.0002$
1.4142	0	0.03	0.48	$11.68 \pm 0.19$	$0.834 \pm 0.0002$
0	1.4142	0.02	0.72	$7.57 \pm 0.08$	$0.840 \pm 0.0001$
0	-1.4142	0.02	0.24	$10.46 \pm 0.36$	$0.836 \pm 0.0013$



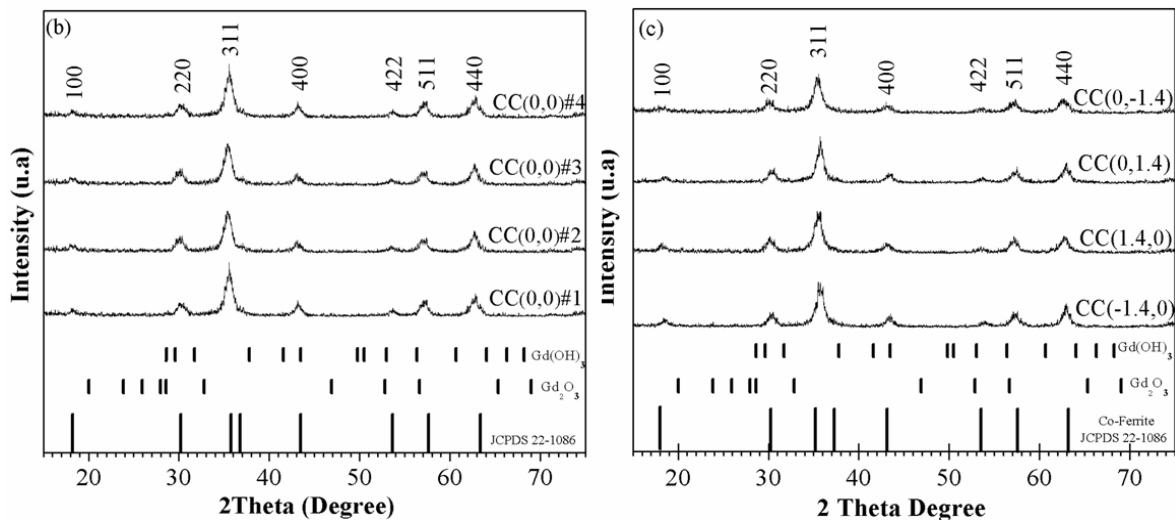


**Figure 63.** XRD Patterns corresponding to the coded and experimental levels for the  $2^2$  factorial and CCD experimental design applied to the synthesis of  $Co_{0.7}Zn_{0.3}Fe_{2-z}Gd_2O_4$ .

## Statistical Characterization

### Analysis $2^2$ factorial design

All responses of interest (average crystallite size and lattice parameter) were statistically analyzed using MINITAB15 and DOE (Design of Experiments) and response surface analyses. For the average crystallite size,  $D$  (nm), the interaction between Gd (at%) and NaOH (M) was not significant. The  $p$ -value = 0.268 obtained is higher than  $\alpha = 0.05$ . On an individual basis, each factor, Gd (at%) and NaOH (M), were found to be statistically significant ( $p$ -values < 0.05). *Table 22* summarizes the ANOVA results. Figure 64 shows in (a) a 3D-surface plot in coded variables and in (b) a contour plot in natural variables, determined from the selected design. The replicas in the center point of this design were used to determine the experimental error associated with these experiments.

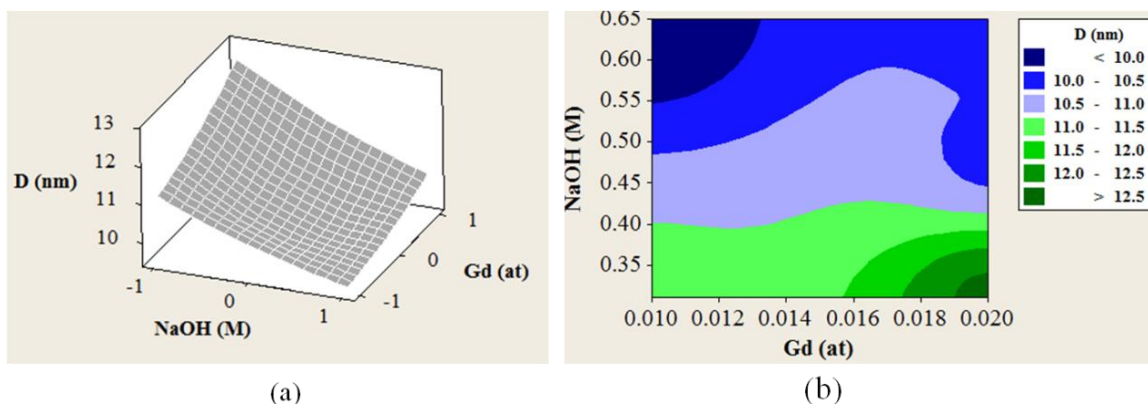


**Figure 64.** (a) 3D-surface plot for the average crystallite size,  $D$ , as function of the controllable variables and (b) contour plot for the 3D-surface plot corresponding to  $2^2$  factorial design.

From the analysis of the data shown in *Table 23* and of the contour plot in *Figure 64(b)* it can be concluded that nanoparticles of larger size ( $> 12.5\text{nm}$ ) can be obtained by increasing the factor A (Gd atomic fraction), while decreasing factor B (NaOH molarity concentration), in the dark green regions. On the other hand, the decrease in crystallite size ( $< 10\text{ nm}$ ) should be favored by increasing factor B and decreasing factor A, in dark blue region. For the lattice parameter it was found that no factors are statistically significant ( $p\text{-values} > 0.05$ ).

**Table 23.** Results for  $2^2$  factorial design; the response variable was the average crystallite size  $D$  (nm).

Term	Coefficient	p-value
Constant	10.3700	0.000
Gd	0.5825	0.015
NaOH	-0.9575	0.004
Gd*Gd	0.5625	0.042
Gd*NaOH	-0.1575	0.268

### Analysis for the central composite design

In order to refine this analysis a CCD design was applied. For this purpose axial points were added to the previous factorial scheme. Also here, the response variable was the average crystallite size determined from XRD information. The corresponding statistical analysis of the response surface evidenced that only the individual factors (Gd level and NaOH concentration) had significance. *Table 23* shows the p-values obtained for these analyses. The contour plot of Figure 65 clearly shows six different regions; the lightest green indicates the values for the Gd atomic fraction and NaOH concentration at which the average crystal size falls below 8 nm. An increment in the green intensity indicates regions where the average crystallite size is in the 8 nm-12 nm range. The darkest green regions suggest the experimental conditions at which the corresponding average crystallite sizes are larger than 12 nm, which should be achieved with Gd around 0.02 at and NaOH around 0.3 M.

*Table 24 Results for CCD design; the response variable was the average crystallite size D (nm).*

Term	Coefficient	p-value
Constant	10.3700	0.000
Gd	0.8180	0.032
NaOH	-0.9896	0.015
Gd*Gd	0.2425	0.489
NaOH*NaOH	-0.3450	0.334
Gd*NaOH	-0.1575	0.718

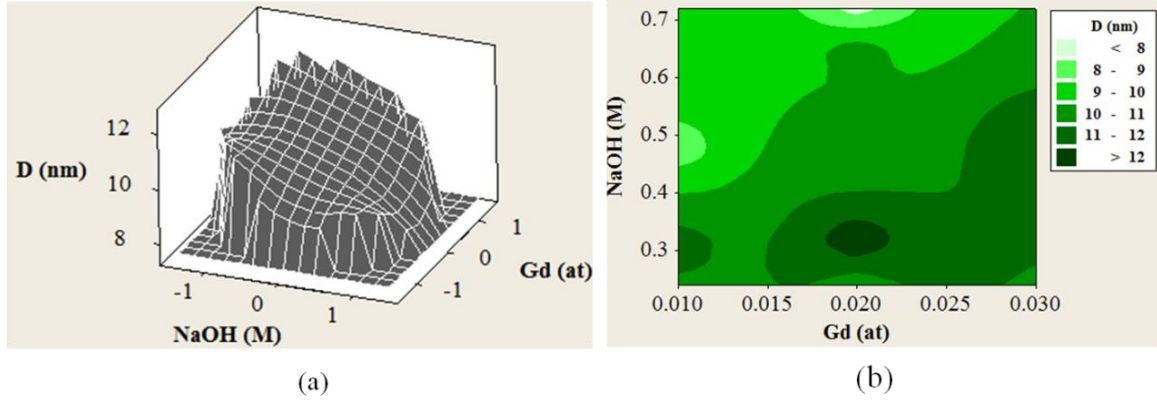


**Figure 65.** (a) 3D-surface plot for the average crystallite size,  $D$ , as function of the controllable variables and (b) contour plot for the 3D-surface plot corresponding to CCD design.

According to the CCD model, the statistical function describing the influence of the factors on the average crystallite size  $D$  is:

$$D = 10.37 + 0.8180 \cdot \text{Gd} - 0.9896 \cdot \text{NaOH}$$

Based on analysis using the CCD design, the statistical significance for the quadratic effect of the Gd atomic fraction is rejected. For magnetocaloric pump applications, the average crystallite size of the ferrite nanoparticles forming the ferrofluid can be around 15 nm. Based on the present statistical results, the amount of the corresponding Gd atomic fraction and NaOH molarity necessary for the synthesis can be obtained.

### 5.5.2. Effect of the Selected Synthesis Parameters on the Magnetic Properties of $\text{Co}_{0.7}\text{Zn}_{0.3}\text{Fe}_{2-z}\text{Gd}_z\text{O}_4$

For all the corner point samples the maximum magnetization ( $M$ ) remains approximately constant, which varied from 59 emu/g to 57 emu/g, for the samples synthesized at (0.01 of Gd - 0.65M of NaOH) and (0.02 of Gd - 0.31M of NaOH). This result not was expected because higher quantities of NaOH increase the nucleation rate and hence inhibit the growth.

It appears that a larger amount of NaOH affects the solubility of the ferrite intermediate (a mixed hydroxide compound), hence the available energy for ion rearrangement in the synthesis has been lowered. Consequently, it is possible that the spinel ferrite structure is not completely inverse and therefore the magnetization smaller. For the central point, the maximum magnetization changes by 4 units (emu/g), which indicates that this difference may be a measurement error. This hypothesis could be corroborated by enhancing the amount of replicates in the design.

The corresponding coercivity decreased from 73 Oe to 31 Oe, when the NaOH molarity decreased from 0.65M to 0.31M. When varying the Gd (at%), it is found that the coercivity also tends to decrease. *Table 24* summarizes the magnetization and coercivity data.

**Table 25** Maximum magnetization,  $M$ , and coercivity,  $H_{ci}$ , for the coded and experimental levels in  $2^2$  factorial and CCD experimental design applied to the synthesis of  $Co_{0.7}Zn_{0.3}Fe_{2-z}Gd_zO_4$ .

Gd (coded)	NaOH (coded)	Gd (at)	NaOH (M)	M (emu/g)	Hci(Oe)
1	-1	0.02	0.31	57	40
1	1	0.02	0.65	58	19
-1	-1	0.01	0.31	58	31
-1	1	0.01	0.65	59	73
0	0	0.02	0.48	57	21
0	0	0.02	0.48	57	25
0	0	0.02	0.48	57	32
0	0	0.02	0.48	61	28
-1.4142	0	0.01	0.48	58	33
1.4142	0	0.03	0.48	52	29
0	1.4142	0.02	0.72	47	36
0	-1.4142	0.02	0.24	59	39

## Statistical Characterization

### Analysis of 2<sup>2</sup> factorial design

All responses of interest (maximum magnetization and coercivity) were statistically characterized using MINITAB15 and DOE (Design of Experiments) and response surface analyses.

For the maximum magnetization neither the factors nor the interaction between them has significance since p-values > 0.05 were obtained. On the other hand, Gd, NaOH\*Gd, and the quadratic effect of the Gd were found to be statistically significant (p-values < 0.05). *Table 25* summarizes the ANOVA results for the coercivity. Figure 66 shows the (a) 3-D surface plot in coded variable and (b) contour plot for the coercivity as function of Gd and NaOH in natural variable.

The contour plot (Figure 66) clearly shows seven different regions. The darkest blue indicates the values for Gd and NaOH at which the coercivity < 20 Oe can be obtained. An abatement in the blue intensity indicates regions where the coercivity is between 20 Oe-40 Oe. An increment in green intensity regions the coercivity is between 40 Oe- 70. The darkest green regions suggest the condition to achieve a coercivity above 70 Oe, which should be achieved with a Gd at % of around 0.02 and NaOH 0.65 M.

**Table 26.** Results of the response surface analysis of the 2<sup>2</sup> factorial design for the coercivity (Oe).

Term	Coefficient	p-value
Constant	26.5	0.000
Gd	-11.250	0.017
NaOH	5.250	0.109
Gd*Gd	14.250	0.023
Gd*NaOH	-15.750	0.007

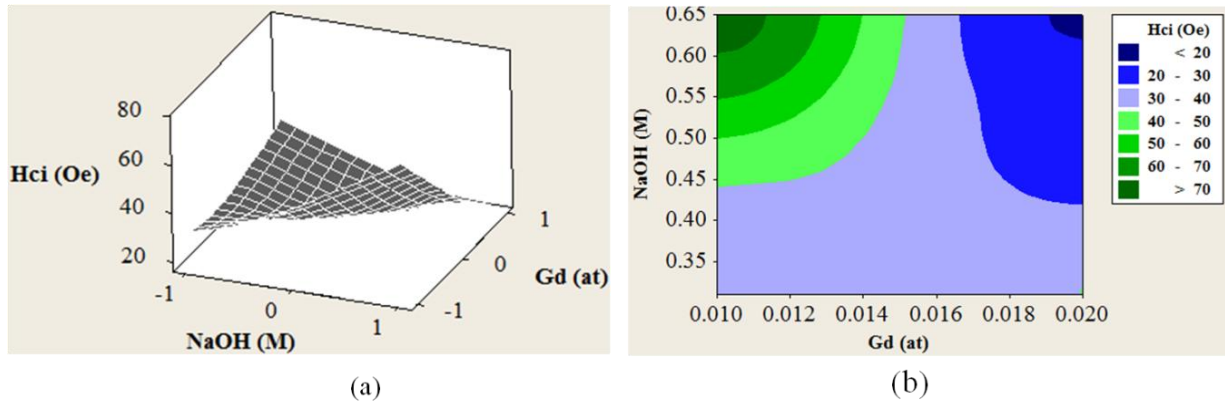


**Figure 66.** (a) 3D-surface plot for the coercivity,  $H_{ci}$ , as function of the controllable variables and (b) contour plot for the 3D-surface plot corresponding to  $2^2$  factorial design.

### Analysis for the central composite design

The corresponding response surface analyses for CCD design evidences that only the interaction of the factors (Gd\*NaOH) has statistical significance. *Table 26* shows the p-values obtained for this analysis. The contour plot (Figure 60-b) clearly shows seven different regions. The darkest blue indicates the values for Gd and NaOH at which the coercivity < 20 Oe can be obtained. The blueish zones indicate regions where the coercivity is between 20 Oe-40 Oe. The darkest green regions evidence that coercivity above 70 Oe should be achieved with Gd at.% of 0.01 and 0.65M NaOH.

**Table 27.** Results for CCD design; the response variable was coercivity (Oe).

Term	Coefficient	p-value
Constant	26.5	0.000
Gd	-6.332	0.077
NaOH	2.095	0.507
Gd*Gd	3.875	0.287
NaOH*NaOH	7.125	0.075
Gd*NaOH	-15.750	0.009

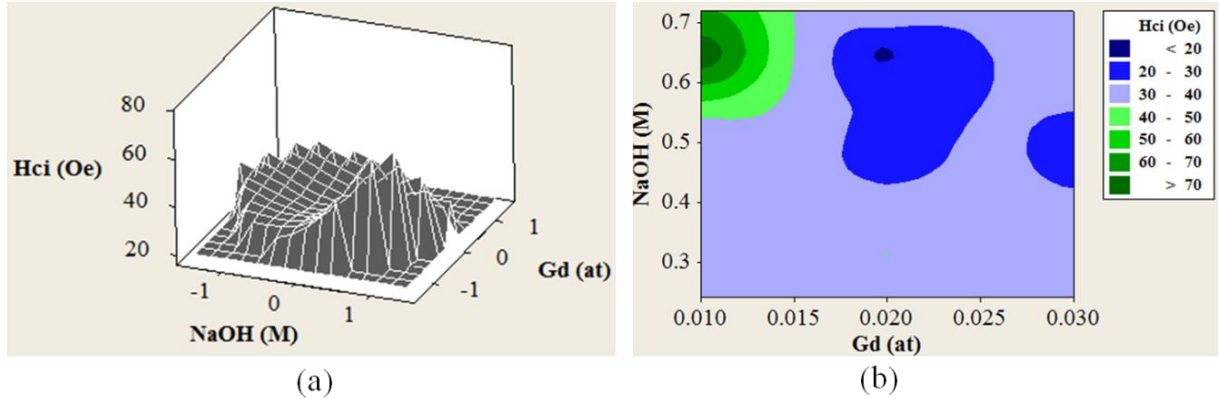


**Figure 67.** (a) 3D-surface plot for the coercivity,  $H_{ci}$ , as function of the controllable variables; (b) contour plot for the 3D-surface plot corresponding to CCD design.

The statistical model describing the influence of the factors on the coercivity is:

$$H_{ci} = 26.5 - 6.332 \cdot Gd - 6.332 \cdot NaOH - 15.750 \cdot Gd \cdot NaOH + 3.875 \cdot Gd \cdot Gd - 7.125 \cdot NaOH \cdot NaOH$$

Based on the outcome of the statistical analysis, it becomes clear that the average crystallite size,  $D$  (nm), is individually dependent on Gd atomic fraction and NaOH molarity. The interaction between these two factors is statistically not significant. On the other hand, the coercivity is susceptible to the Gd atomic fraction and to the interaction of Gd atomic fraction and NaOH molarity. Furthermore, the maximum magnetization and lattice parameter were not affected within the levels established for the Gd atomic fraction and NaOH molarity.

### **5.5.3. Concluding Remarks**

Statistical analyses evidenced the dependence of the average crystallite size,  $D$  (nm), on Gd atomic fraction and NaOH molarity, while the coercivity is susceptible only to the Gd atomic fraction and to the interaction of Gd with NaOH. The maximum magnetization and lattice parameter were not affected.

## CHAPTER VI: FINAL REMARKS

We have successfully synthesized pure and rare-earth doped  $\text{Co}_x\text{Zn}_{1-x}\text{Fe}_2\text{O}_4$  ferrite nanocrystals. Depending of the synthesis protocol, it was also possible to achieve a fine control on crystal size at the nanoscale. It was possible by controlling the oversaturation conditions during the ferrite forming reaction, which in turn favored the crystal growth within the single domain region. The control of the flow-rate at which the reactants were contacted in aqueous phase, attained by using a peristaltic micro pump, made possible that early ferrite nuclei acted as pre-existent seeds while promoting the heterogeneous nucleation associated with crystal growth.

The average crystallite size increased from  $(6.50 \pm 0.21)\text{nm}$  to  $(13.08 \pm 1.01)\text{nm}$  when the  $\text{Co}^{2+}$  atomic fraction 'x', varied in the 0.5-1.0 range. This trend was attributed to the lower affinity of  $\text{Co}^{2+}$  to oxygen as compared to  $\text{Zn}^{2+}$ , which could have affected the solubility of the ferrite intermediate compound. HRTEM analyses evidenced the crystallinity of CoZn ferrite particles even at the nanometric scale. The corresponding average crystallite size increased up to 30 % when the ferrite nanocrystals were synthesized at low flow rates (1mL/min). This drastic enlargement in crystallite size was explained by the promotion of heterogeneous nucleation and by Ostwald ripening processes.

Raman spectroscopy analyses on the CoZn ferrite samples suggested that the principal  $A_{1g}$  and  $T_{2g}$  vibration modes were affected by the sample composition. The modes suggest lattice distortions for CoZn ( $x = 0.7$ ) ferrite. Raman analyses also suggested the migration of  $\text{Co}^{2+}$  ions between tetrahedral and octahedral sites. This conclusion was also supported by Mössbauer spectroscopy analyses of the samples.

Regarding the corresponding magnetic properties, the increase of magnetic Co atomic fraction from 0.5 to 1.0 caused the rise in the maximum magnetization that was enhanced from 48 to 60 emu/g. This rising trend in magnetization with larger 'x' values was expected and attributed to stronger  $\text{Co}^{2+}$ -O- $\text{Fe}^{3+}$  interactions and the magnetic character of Co species replacing diamagnetic Zn species in the ferrite lattice. The corresponding coercivity values also increased, from 8 Oe to 300 Oe, with 'x'. This was attributed to changes in the crystal field and in the magnetic anisotropy due to the larger presence of  $\text{Co}^{2+}$  ions. Although an enhancement on crystal size was observed, lower flow rates (1 mL/min) reduced the magnetization, which is attributed to the promotion of random spin canting, the development of magnetically dead surface layers, and the migration of  $\text{Co}^{2+}$  ions between tetrahedral and octahedral sites. However, the corresponding coercivity dramatically increases. This rising trend in coercivity with lower flow-rates was observed for the powders synthesized at  $x = 0.8$  (from 48 Oe to 716 Oe),  $x = 0.9$  (from 150 Oe to 1775 Oe), and  $x = 1.0$  (from 300 Oe to 2752 Oe). The enhancement of the coercivity is attributed to the enlargement of the crystal size, as suggested by the XRD measurements, within the single magnetic domain range. The demagnetization temperature ( $T_d$ ) increased from 106 °C to 590 °C with increasing Co atomic fraction that should have also promoted the stronger superexchange interaction. The pyromagnetic coefficient ( $\Delta M/\Delta T$ ) did not change with the synthesis method and varied between 0.19 emu/g-K and 0.17 emu/g-K when 'x' varied in the 0.5-0.9 interval.

The Mössbauer spectroscopy analyses of the CoZn ferrite powders corroborated that the increase in Co atomic fraction favors the magnetic ordering in the ferrite structure, an increment in  $H_f$  appears for the samples with higher Co atomic fraction. Also, the variation of the  $\text{Fe}^{3+}$  distribution in the spinel structure of the ferrite synthesized at 1mL/min, when compared to the same sample produced with no control on flow-rate, was also evidenced by Mössbauer analysis.

This redistribution of Fe ions in the lattice should have favored the spin canting on the crystal surface and hence, the increase of the surface anisotropy.

The average crystallite size of CoZn ( $x = 0.7$ ) ferrite synthesized by the hydrothermal method increased from  $(9.96 \pm 0.24)$  nm to  $(14.73 \pm 0.24)$  nm, when the synthesis temperature varied from 100 °C to 250 °C. At higher temperatures, the dissolution of smaller particles and the growth of the larger ones were promoted. The corresponding crystal growth explains the rise in both, the maximum magnetization and coercivity.

Doping of the CoZn ferrite ( $x = 0.7$ ) with rare earths (RE) elements Dy and Gd, caused the average crystallite size to increase. This enlargement of crystal size with the dopant level could be attributed to the improved solubility of the ferrite precursor hosting the RE ions. The higher the solubility, the faster the dissolution stage and the subsequent recrystallization process associated with the ferrite formation. The observed drop of magnetization with increasing the concentration of the dopant is due to the replacement of  $\text{Fe}^{3+}$  by  $\text{RE}^{3+}$  ions in the octahedral sites. However, the possible formation of isolated, non-magnetic, Gd or Dy compounds not detected by XRD measurements could not be ruled out. The demagnetization temperature ( $T_d$ ) is reduced by the incorporation of Dy and Gd in the ferrite lattice. This was explained by weak  $\text{RE}^{3+}\text{-O-Fe}^{3+}$  interaction, which could be destroyed at low thermal energy.

In order to find the best possible synthesis conditions to obtain nanoparticles with the desired properties for magnetocaloric pump applications the  $2^2$  Factorial and CCD design were applied. Experimental design and the subsequent statistical analyses evidenced the dependence of the average crystallite size,  $D$  (nm), on Gd atomic fraction and NaOH molarity; the coercivity value was strongly dependent on both, the Gd atomic fraction and the interaction of Gd concentration

with NaOH concentration. NaOH and Gd both affect the solubility of the hydroxide precursor and promote indirectly spin canting and formation of dead layers on the surface. This results in enhanced shape anisotropy and consequently the coercivity increases. The maximum magnetization and lattice parameter were not affected in 0.01-0.03 (at) and 0.24M-0.72M of Gd atomic fraction and NaOH molarity, respectively.

**On a materials application basis**, the following comments can be stated. The highest magnetization was 73 emu/g ( $x = 0.7$ ) and was attained when the ferrite powders were synthesized by the hydrothermal method. However, neither the coercivity nor the demagnetization temperature were suitable for applications in the magnetocaloric pump. Although we could decrease  $T_d$  by increasing the Zn concentrations ( $T_d$  can be as low as 100 °C), it would take place at expenses of the drop in magnetization and the pyromagnetic coefficient. This applicability scenario becomes more promising after doping the ferrite with Gd or Dy species. For 5% doping the maximum magnetization was an acceptable 53 emu/g, while the coercivity reached a low value of 20 Oe, which are in the required range for applications. The lowest value for the demagnetization temperature was 230 °C reached with Gd-doping. This same sample had a pyromagnetic coefficient of 0.59 emu/g-K, which is a significant increase over all other systems evaluated in this work and also the literature.

Therefore, from a material application viewpoint in magnetocaloric pumping, the doping of the CoZn ferrite with Gd species will promote both, the drop in the demagnetization temperature (it decreased from 350 °C down to 230 °C) and a remarkable increase of the pyromagnetic coefficient. The moderate magnetization and minimum coercivity of these nanoparticles enable them to be considered a very promising candidate for magnetocaloric pumping systems.

Future research could be oriented to synthesize Co-Zn ( $x = 0.7$ ) ferrites doped with 5% Gd by using the hydrothermal method at 250 °C. This elevated temperature would guarantee high crystallinity and keep the magnetization at a high value. To limit crystallite growth and to keep the coercivity low a 0.72M NaOH solution is recommended, as obtained from the statistical design.

## CHAPTER VII: REFERENCES

- <sup>1</sup> R. Sánchez and R. Zysler, *Ciencia Hoy* **15**, 40-51 (2005).
- <sup>2</sup> E. Auzans, D. Zins, E. Blums, and R. Massart, *Journal of Materials Science* **34**, 1253-1260 (1999).
- <sup>3</sup> R. Arulmurugan, G. Vaidyanathan, S. Sendhilkathan, and B. Jeyadevan, *Physica B: Condensed Matter* **363**, 225-231 (2005).
- <sup>4</sup> C.N. Chinnasamy, M. Senoue, B. Jeyadevan, O. Perales-Perez, K. Shinoda, and K. Tohji, *Journal of Colloid and Interface Science* **263**, 80-83 (2003).
- <sup>5</sup> L. Zhao, W. Xu, H. Yang, and L. Yu, *Current Applied Physics* **8**, 36-41 (2008).
- <sup>6</sup> J.F. Hochepped and M.P. Pileni, *J. Appl. Phys.* **87**, 2472 (2000).
- <sup>7</sup> S. Tao, X. Liu, X. Chu, and Y. Shen, *Sensors and Actuators B: Chemical* **61**, 33-38 (1999).
- <sup>8</sup> E. Rezlescu, N. Rezlescu, and P.D. Popa, *Sensors and Actuators A: Physical* **59**, 292-294 (1997).
- <sup>9</sup> X. Chu, D. Jiang, and C. Zheng, *Materials Science and Engineering: B* **129**, 150-153 (2006).
- <sup>10</sup> A. Nethe, T. Schöppe, and H.-D. Stahlmann, *Journal of Magnetism and Magnetic Materials* **201**, 423-426 (1999).
- <sup>11</sup> A. Martin and J. Bruce, *Prenatal Diagnostic* **17**, 1059-1066 (1997).
- <sup>12</sup> R. Hergt, S. Dutz, R. Müller, and M. Zeisberger, *J. Phys.: Condens. Matter* **18**, S2919-S2934 (2006).
- <sup>13</sup> R. Olaru and D.D. Dragoi, *Sensors and Actuators A: Physical* **120**, 424-428 (2005).
- <sup>14</sup> L.J. Love, J.F. Jansen, T.E. McKnight, Y. Roh, and T.J. Phelps, *NanoBioscience, IEEE Transactions On* **3**, 101-110 (2004).
- <sup>15</sup> N. Hirano, S. Nagaya, M. Takahashi, T. Kuriyama, K. Ito, and S. Nomura, *AIP Conf. Proc.* **613**, 1027-1034 (2002).
- <sup>16</sup> R.E. Rosensweig, *Ferrohydrodynamics* (Courier Dover Publications, 1997).
- <sup>17</sup> A. Hatch, E. Kamholz, G. Holman, P. Yager, and F. Böhringer, *Journal of Microelectromechanical Systems* **10**, 215-221 (2001).
- <sup>18</sup> R.V. Upadhyay, K.J. Davies, S. Wells, and S.W. Charles, *Journal of Magnetism and Magnetic Materials* **132**, 249-257 (1994).
- <sup>19</sup> G. Vaidyanathan and S. Sendhilkathan, *Journal of Magnetism and Magnetic Materials* **320**, 803-805 (2008).
- <sup>20</sup> H. Wang, E. Li, G.Y. Li, and Z.H. Zhong, *Advances in Engineering Software* **39**, 629-645 (2008).
- <sup>21</sup> J.M. Castro, M.C. Ríos, and C.A. Mount-Campbell, *Modelling Simul. Mater. Sci. Eng.* **12**, S121-S149 (2004).
- <sup>22</sup> K.H.J. Buschow, *Handbook of Magnetic Materials* (Elsevier, 2007).
- <sup>23</sup> R.C. O'Handley, *Modern Magnetic Materials: Principles and Applications* (Wiley, 2000).
- <sup>24</sup> C. Kittel, *Introduction to Solid State Physics* (Wiley, 2005).
- <sup>25</sup> A. Aharoni, *Introduction to the Theory of Ferromagnetism* (Oxford University Press, 2000).
- <sup>26</sup> J. Crangle, *The Magnetic Properties of Solids* (Edward Arnold, 1977).
- <sup>27</sup> B.D. Cullity and C.D. Graham, *Introduction to Magnetic Materials* (Wiley-IEEE, 2008).
- <sup>28</sup> H.S. Nalwa, *Magnetic Nanostructures* (American Scientific Publishers, 2002).
- <sup>29</sup> D. Jiles, *Introduction to Magnetism and Magnetic Materials* (Chapman and Hall, 1991).
- <sup>30</sup> A. Hernando and J.M. Rojo, *Fisica De Los Materiales Magneticos* (Editorial Sintesis, S.A., Madrid, Spain, n.d.).

- <sup>31</sup> A. Goldman, *Modern Ferrite Technology* (Springer Science & Business, 2006).
- <sup>32</sup> H.D. Williams, K. O'Grady, M. El Hilo, and R.W. Chantrell, *Journal of Magnetism and Magnetic Materials* **122**, 129-133 (1993).
- <sup>33</sup> M. Mahmoudi, P. Stroeve, A.S. Milani, and A.S. Arbab, *Superparamagnetic Iron Oxide Nanoparticles:: Synthesis, Surface Engineering, Cytotoxicity and Biomedical Applications* (Nova Science Pub Inc, 2011).
- <sup>34</sup> N. Knobel and L.M. Socolovsky, *Revista Mexicana De Fisica* **E-50**, 8-28 (2004).
- <sup>35</sup> P.M. Levy, *Phys. Rev.* **135**, A155 (1964).
- <sup>36</sup> J.S. Smart, *Am. J. Phys.* **23**, 356 (1955).
- <sup>37</sup> V. Privman, D.V. Goia, J. Park, and E. Matijevic, *Journal of Colloid and Interface Science* **213**, 36-45 (1999).
- <sup>38</sup> G. Cao, *Nanostructures and Nanomaterials: Synthesis, Properties & Applications* (Imperial College Press, 2004).
- <sup>39</sup> F. Caruso, *Colloids and Colloid Assemblies: Synthesis, Modification, Organization and Utilization of Colloid Particles* (Wiley-VCH, 2004).
- <sup>40</sup> L.K. Kurihara, G.M. Chow, and P.E. Schoen, *Nanostructured Materials* **5**, 607-613 (1995).
- <sup>41</sup> J. Grum, *Nanostructures & Nanomaterials, Synthesis, Properties & Applications By G.Cao* (Imperial College, 2004).
- <sup>42</sup> B. Cushing, L. Kolesnichenko, and J. O'Connor, *Chemical Review* **104**, 3893-3946 (2004).
- <sup>43</sup> T. Sugimoto, *Advances in Colloid and Interface Science* **28**, 65-108 (1987).
- <sup>44</sup> F. Fievet, J.P. Lagier, B. Blin, B. Beaudoin, and M. Figlarz, *Solid State Ionics* **32-33**, 198-205 (Febrero).
- <sup>45</sup> P.S. Odenbach, *J. Phys.: Condens. Matter* **18**, (2006).
- <sup>46</sup> J.A. Ritter, A.D. Ebner, K.D. Daniel, and K.L. Stewart, *Journal of Magnetism and Magnetic Materials* **280**, 184-201 (2004).
- <sup>47</sup> Q.A. Pankhurst, J. Connolly, S.K. Jones, and J. Dobson, *J. Phys. D: Appl. Phys.* **36**, R167-R181 (2003).
- <sup>48</sup> C.C. Berry and A.S.G. Curtis, *J. Phys. D: Appl. Phys.* **36**, R198-R206 (2003).
- <sup>49</sup> G. Gutierrez, J. Catano, and O. Perales-Perez, *ASME Conf. Proc.* **2006**, 751-756 (2006).
- <sup>50</sup> D.C. Montgomery, *Design and Analysis of Experiments* (John Wiley and Sons, 2008).
- <sup>51</sup> R.L. Mason, R.F. Gunst, and J.L. Hess, *Statistical Design and Analysis of Experiments* (John Wiley & Sons, Inc., Hoboken, NJ, USA, 2003).
- <sup>52</sup> P.C. Morais, V.K. Garg, A.C. Oliveira, L.P. Silva, R.B. Azevedo, A.M.L. Silva, and E.C.D. Lima, *Journal of Magnetism and Magnetic Materials* **225**, 37-40 (2001).
- <sup>53</sup> C.N. Chinnasamy, B. Jeyadevan, O. Perales-Perez, K. Shinoda, K. Tohji, and A. Kasuya, *Magnetics, IEEE Transactions On* **38**, 2640-2642 (2002).
- <sup>54</sup> C.N. Chinnasamy, M. Senoue, B. Jeyadevan, O. Perales-Perez, K. Shinoda, and K. Tohji, *Journal of Colloid and Interface Science* **263**, 80-83 (2003).
- <sup>55</sup> V. Kumar, A. Rana, M.S. Yadav, and R.P. Pant, *Journal of Magnetism and Magnetic Materials* **320**, 1729-1734 (2008).
- <sup>56</sup> G.V. Duong, N. Hanh, D.V. Linh, R. Groessinger, P. Weinberger, E. Schafner, and M. Zehetbauer, *Journal of Magnetism and Magnetic Materials* **311**, 46-50 (2007).
- <sup>57</sup> G. Vaidyanathan and S. Sendhilnathan, *Physica B: Condensed Matter* **403**, 2157-2167 (2008).
- <sup>58</sup> C. Hou, H. Yu, Q. Zhang, Y. Li, and H. Wang, *Journal of Alloys and Compounds* **491**, 431-435 (2010).

- <sup>59</sup> J. Feng, L.-Q. Guo, X. Xu, S.-Y. Qi, and M.-L. Zhang, *Physica B: Condensed Matter* **394**, 100-103 (2007).
- <sup>60</sup> E. Ateia, M.A. Ahmed, and A.K. El-Aziz, *Journal of Magnetism and Magnetic Materials* **311**, 545-554 (2007).
- <sup>61</sup> O. Perales-Perez, E. Calderon-Ortiz, and S. Urcia-Romero, *Technical Proceedings of the Nanotechnology Conferences and Trade Show* **1**, 133 (2009).
- <sup>62</sup> E. Calderón-Ortiz, O. Perales-Perez, P. Voyles, G. Gutierrez, and M.S. Tomar, *Microelectronics Journal* **40**, 677-680 (April).
- <sup>63</sup> S. Urcia-Romero, O. Perales-Perez, and G. Gutierrez, *Technical Proceedings of the Nanotechnology Conferences and Trade Show* **1**, 113 (2009).
- <sup>64</sup> Y. Cedeño-Mattei, O. Perales-Perez, M.S. Tomar, F. Roman, P.M. Voyles, and W.G. Stratton, *J. Appl. Phys.* **103**, 07E512 (2008).
- <sup>65</sup> B.D. Cullity and S.R. Stock, *Elements of X-Ray Diffraction*, 3rd ed. (Prentice Hall, 2001).
- <sup>66</sup> H. Klug and A. Leroy, *X-RAY DIFFRACTION PROCEDURES For Polycrystalline and Amorphous Materials*, Second Edition (John Wiley & Sons, Inc., n.d.).
- <sup>67</sup> K. Nakamoto, *Infrared and Raman Spectra of Inorganic and Coordination Compounds*, fourth edition (Wiley- Interscience Publications, Singapore, 2006).
- <sup>68</sup> E. Smith and Dent, G., *Modern Raman Spectroscopy: A Practical Approach* (John Wiley & Sons, Inc., Online, 2005).
- <sup>69</sup> G.J. Long, *Mössbauer Spectroscopy Applied to Inorganic Chemistry* (Springer, 1984).
- <sup>70</sup> S. Chikazumi, *Physics of Ferromagnetism*, 2nd ed. (Oxford University Press, USA, 1997).
- <sup>71</sup> T. Yu, Y. Shi, and J. Ding, *Journal of Physics: Condensed Matter* **14**, L613-L618 (2002).
- <sup>72</sup> L.V. Gasparov, A. Rush, G. Güntherodt, and H. Berger, *Phys. Rev. B* **79**, 144303 (2009).
- <sup>73</sup> G. Shemer, E. Tirosh, T. Livneh, and G. Markovich, *The Journal of Physical Chemistry C* **111**, 14334-14338 (2007).
- <sup>74</sup> M. Sertkol, Y. Köseoglu, A. Baykal, H. Kavas, and A.C. Basaran, *Journal of Magnetism and Magnetic Materials* **321**, 157-162 (2009).
- <sup>75</sup> T. Ozkaya, M.S. Toprak, A. Baykal, H. Kavas, Y. Köseoglu, and B. Aktas, *Journal of Alloys and Compounds* **472**, 18-23 (2009).
- <sup>76</sup> R. Arulmurugan, B. Jeyadevan, G. Vaidyanathan, and S. Sendhilnathan, *Journal of Magnetism and Magnetic Materials* **288**, 470-477 (2005).
- <sup>77</sup> R. Arulmurugan, G. Vaidyanathan, S. Sendhilnathan, and B. Jeyadevan, *Journal of Magnetism and Magnetic Materials* **298**, 83-94 (2006).
- <sup>78</sup> R. Arulmurugan, G. Vaidyanathan, S. Sendhilnathan, and B. Jeyadevan, *Journal of Magnetism and Magnetic Materials* **303**, 131-137 (2006).
- <sup>79</sup> N.A. Halasa, G. DePasquali, and H.G. Drickamer, *Phys. Rev. B* **10**, 154 (1974).
- <sup>80</sup> C. Rath, S. Anand, R.P. Das, K.K. Sahu, S.D. Kulkarni, S.K. Date, and N.C. Mishra, *J. Appl. Phys.* **91**, 2211 (2002).
- <sup>81</sup> N. Moumen and M.P. Pileni, *The Journal of Physical Chemistry* **100**, 1867-1873 (1996).
- <sup>82</sup> S.D. Shenoy, P.A. Joy, and M.R. Anantharaman, *Journal of Magnetism and Magnetic Materials* **269**, 217-226 (2004).
- <sup>83</sup> P. Chandramohan, M.P. Srinivasan, S. Velmurugan, and S.V. Narasimhan, *Journal of Solid State Chemistry* **184**, 89-96 (2011).
- <sup>84</sup> Z. Cvejic, S. Rakic, A. Kremenovic, B. Antic, C. Jovalekic, and P. Colomban, *Solid State Sciences* **8**, 908-915 (2006).

<sup>85</sup> S.E. Jacobo, S. Duhalde, and H.R. Bertorello, *Journal of Magnetism and Magnetic Materials* **272-276**, 2253-2254 (2004).

<sup>86</sup> R.V. Upadhyay, R.V. Mehta, K. Parekh, D. Srinivas, and R.P. Pant, *Journal of Magnetism and Magnetic Materials* **201**, 129-132 (1999).